Temporal and spatial correlations in earthquake dynamics : physical modeling and data analysis

Vincenzo Schimmenti

université PARIS-SACLAY

Temporal and spatial correlations in earthquake dynamics: physical modeling and data analysis

Corrélations temporelles et spatiales dans la dynamique des tremblements de terre: modélisation physique et analyse de données

Thèse de doctorat de l'université Paris-Saclay

École doctorale n° 564, Physique en Île-de-France (PIF)
Spécialité de doctorat: Physique
Graduate school: Physique, Référent : Faculté de Sciences d'Orsay

Thèse préparée dans l'unité de recherche **LPTMS** (Université Paris-Saclay, CNRS), sous la direction d'**Alberto ROSSO**, Directeur de Recherche (CNRS), et le co-encadrement de **François LANDES**, Maitre des conférences (Université Paris-Saclay)

Thèse soutenue à Paris-Saclay, le 23 Novembre 2023, par

Vincenzo Maria SCHIMMENTI

Composition du jury

Membres du jury avec voix délibérative

Cécile MONTHUS Directrice de recherche, Institut de Physique Théorique (IPhT), CEA Saclay	Présidente
Herbert SPOHN Professeur émérite, Technische Universität München (TUM), München	Rapporteur & Examinateur
Jerome WEISS Directeur de recherche, Institut des Sciences de la Terre (ISTerre), CNRS, Université Grenoble Alpes, Grenoble	Rapporteur & Examinateur
Aurelien DECELLE Professeur associé, Dinámica de Sistemas Desordenados, Universidad Complutense Madrid (UCM), Madrid	Examinateur

THESE DE DOCTORAT

NNT : 2023UPASP159

université PARIS-SACLAY | ÉCOLE DOCTORALE Physique en Île-de-France (PIF)

Titre: Corrélations temporelles et spatiales dans la dynamique des tremblements de terre : modélisation physique et analyse de données **Mots clés:** répliqués, statistiques des records, apprentissage automatique, domaines magnétiques, systèmes désordonnés, polymers dirigés)

Résumé: Dans le domaine de la sismologie, les répliques sismiques sont des séismes de taille moindre qui suivent un séisme principal. Ces répliques sont causées par la déstabilisation du sol dans les régions proches de l'épicentre du séisme principal. Dans cette thèse, nous étudierons ce phénomène de trois manières différentes. Dans la première partie, nous discuterons des liens entre des modèles simples de réplique et la statistique des records des processus stochastiques. Dans la deuxième partie, nous utiliserons les similitudes entre les séquences sismiques et la dynamique de glissement de domaines magnétiques. Dans la troisième partie, nous utiliserons l'apprentissage machine afin de construire une méthode de prédiction des répliques sismiques exploitant les mesures de déformation du sol obtenues par satellite GPS. Enfin, dans la dernière partie de cette thèse, nous discuterons d'un sujet différent, lequel étant l'écoulement d'un fluide non newtonien dans un milieu poreux en utilisant les outils de la physique des systèmes désordonnés et des polymères dirigés dans des milieux aléatoires.]

Title: Temporal and spatial correlations in earthquake dynamics: physical modeling and data analysis
Keywords: aftershocks, record statistics, machine learning, domain walls, disordered systems, directed polymers

Abstract: In seismology, aftershocks are smaller earthquakes originating from the destabilised crust in the regions close to a larger earthquake, the mainshock. In this thesis we study this phenomenon from three distinct perspectives. In the first one we unveil the connections between simple models of aftershocks occurrence and record statistics of stochastic processes. The second approach builds up on the similarities between earthquake sequences and mainshock-aftershocks groups with the creep dynamics of a domain wall expanding in a thin magnetic film. Finally, we use machine learning tools to construct a forecasting method for aftershock occurrence by exploiting measurements of surface deformation coming from Global Positioning System (GPS) satellites. As an addendum, in the last part of the thesis, we discuss the physics of yield-stress fluids in porous media and its links to the physics of disorder systems and directed polymers in random media.

Contents

Acknowledgements

I would like to start by deeply thanking my supervisors, Alberto Rosso and François Landes, for accompanying and guiding me in this journey of three years. We met during my master's project in the unfortunate year of 2020 and you were there for me during these especially hard times. They are mentors and friends. Alberto has taught me the importance of clarity, both of the mind and in paper. We shared nice and hard moments, often in unusual locations. I particularly appreciated our "paper writing" days, where we would finish a paper between a morning pain au chocolat and a healthy and quick lunch. You always treated me like a peer but you never hesitated when I needed a dose of reality. I deeply thank François for showing me the importance of communication in science. I always lacked in this department and you pushed me to be more open with the people I work with. I can't thank you enough for putting up with all my flaws. I realize now how much I have matured these three years and a lot of it is because of both of you. My hope is these three years to be the start of a long-lasting human and scientific relationship. I would also thank other researchers I worked and discussed with Andrea De Luca for being my third "ghost" supervisor, for being there as a scientist and a friend. Satya Majumdar for the amazing dinners and for teaching me lots of nice mathematics. Giuseppe Petrillo for being a good friend and a precious light for many questions I had during my PhD. I am also grateful to Valentina Ros, Silvio Franz, Raoul Santachiara, Laura Foini, Gianfranco Durin and, especially, Marco Baiesi, without whom I would have not started my French adventure. Moreover, I would like to thank the jury: the présidente Cecile Monthus, the rapporteurs Jerome Weiss and Herbert Spohn and last but not least the examinateur Aurelien Decelle. Finally, I would like to thank both Emmanuel Trizac and Alberto Rosso who directed the lab during my PhD and Claudine Le Vaou and Karolina Kolodziej for being the foundations upon which LPTMS is built. About LPTMS, I could not have asked to be part of a better lab to work. In particular, I would like to thank all the interns, PhDs and post-docs I met there: Francesco Mori, Benjamin De Brunye, Felix Benoist, Lorenzo Gotta, Lorenzo Rosso, Gabriel Lando, Lenart Zadnik, Andrea Tononi, Julien Despres, Gior-

gio Ciliberto, Alice Marché, Gianluca Morettini, Alberto Nardin, Marco Biroli, Ivan Burenev, Li Gan, Federico Gerbino, Romain Usciati, Luca Capizzi, Giuseppe Del Vecchio Del Vecchio, Pawat Akarapipattana, Maximilien Bernard, Louis Bremaud, Matteo Butano, Alessandro Pacco, Dimitrios Tzivrailis, Giovanni Russo and many others that passed by. A special thanks goes to: Mauro, which showed me how a good heart and a bit of cynicism can make an amazing person (plus, he is a devoted driver); Fabian that with his cheerfulness, joy and, foremost, music made possible a lot of amazing nights and painted the city of Paris with great memories; the italian gang Marco, Andrea, Saverio (merci Le Gob pour tout), Guido and Alessandro (for the tons gossip, political fights and parties), Valentina R. (for the numerous coffee breaks), Sharon for being a great friend and drinking companion (up to a fault) this last year, Martina and Carlotta with whom I shared super fun and deep moments and were always amazing (and witnessed mine and others thesis madness very close up) and, at large, all the people from CFB (Elena, Ignacio, Giulia, Maite and many others). Continuing, Jules and Charbel for standing me while disturbing your quiet by complaining about random things in my life. And how can I forget Lara, the unstoppable, who organized the best parties I had in Paris and with whom now I share the Dresden adventure. We will keep the Parisian traditions alive. Moreover, thanks to two of my office mates, Enrico and Flavio. The former for being an insatiable debater and a source of many discussions. The latter, also known as the clown, for triggering the most genuine waves of laughter I had in my life (plus, it's cool to study spin glasses). You guys are great friends. Then, of course, Ana - unofficially my last flatmate in Paris - for being fantastic and always finding new ways to make fun of everyone and everything, with a bit of evil touch (and ""discuss"" about Tik-Tok trends). Two other people were a pillar in these three years. Federico and Denise. You guys were my first flatmates and we shared the weirdest times (remember Parc de Sceaux). You guys were the best thing in my first Parisian year and I will never forget all the good and bad moments. We did this journey together and you became two of my best friends. And last, but definitely not least, Sap "al Sapone". Man, you are my bro. We were the fixers of LPTMS. We did so much stuff together that it would take pages to tell the stories. Thanks for being there, buddy.

In all this, we would discuss also science with everyone but, you know, we can skip this part for the moment. I'll do italian for a second now. Gotta thank my family.

Grazie mamma, grazie papa e grazie Marcolino. Grazie Andre e Luci (vi metto insieme, ci sta). Sarebbe troppo riduttivo provare a dire qualcosa qua. Vi voglio bene, un sacco di bene. Grazie per esserci sempre.

E grazie Vale. Senza di te sarei una mina vagante.

P.S.: Probably - most definitely - I forgot many people and many things. Thanks to everyone who was there during these three years in Paris. It was quite a journey, guys.

Introduction

This thesis aims to investigate the spatial and temporal correlations of systems displaying avalanches. In statistical physics, an avalanche is a reorganization of the degrees of freedom of a system in response to a generated instability, such as the change in applied forces, thermal fluctuations, or internal relation mechanism. The study of avalanche dynamics is as interesting as they are ubiquitous: earthquakes are the avalanches occurring in seismic faults [1–7], avalanches characterize the deformation crystalline structures put under load [8,9], they are precursors of rupture in brittle materials [10], describe the invasion of porous media by a fluid [11,12] and even emerge in neuronal activity [13]. Often avalanches have clustering properties, both in time and space: a principal avalanche occurs that can trigger numerous "children" avalanches exhibiting rich statistical structures. A prime example and the main focus of this thesis is in the binomial of mainshocks and aftershocks in seismology. Characterizing how aftershocks occur is of primal importance, both for scientific and practical human applications. As such, the central part of the manuscript is divided into three chapters, each referring to a different treatment of the subject of aftershocks.

In the first chapter, based on the published paper [14], we develop and exactly solve a minimal model of avalanches that display aftershocks, generating sequences similar to the ones observed in actual earthquakes ones. This model is inspired by mean-field models of avalanches, such as the famous ABBM model [15], and it is grounded in the class of particles in disordered landscapes. Using extreme value statistics, we show that this model displays avalanches with a power-law distribution, which we analytically determine. Moreover, we characterize analytically and numerically the correlations between avalanches, showing that such a model is one of the few solvable ones presenting aftershocks.

In the second chapter, we perform the data analysis of the dynamics of a domain wall expanding in an ultra-thin magnetic film under the influence of a small magnetic field. The name creep in magnetic materials is borrowed from the one in solid mechanics, which corresponds to slow but progressive accumulation of strain

deformation upon applying external (small) stress over a long time. Here the strain corresponds to the expansion of the domain wall which is driven by a small external magnetic field. The interplay between temperature, impurities present in the underlying film crystalline structure and driving field give rise to a rich dynamics, understanding which is extremely important, for example, in spintronics. We frame the system in the family of driven interfaces in random media, which are the prototypical systems showing avalanche behavior, and we test the theoretical predictions on the experimental data. We show the first experimental observation for the presence of mainshock-aftershocks pairs in the avalanche dynamics of the domain wall which previously has been predicted by the theory [16] and observed recently in numerical simulations [17].

Finally, in the third chapter, we investigate a new approach to earthquake forecasting, specifically in aftershock prediction. The starting point is a recent work [18] that exploited reconstructed underground displacement maps following large earthquakes (mainshocks) to infer spatial patterns of the subsequent aftershocks using machine learning. While very promising, such underground deformation maps need to be build by employing a precise knowledge of the fault system and are hardly doable in real-time on in near real-time. Here we explore the possibility of using surface displacement maps without prior fault knowledge to achieve the same goal of pattern prediction. In particular, such surface displacement maps can be reconstructed with relative more ease by using displacement measurements coming from GPS stations on the ground. GPS stations communicate with satellites for continuous measurements of their position on the ground and a satisfying reading can be obtained within a few hours lag, making them appropriate for near real-time predictions. In practice, we first discuss how to construct such maps and then we compare a classical statistical method and a machine learning approach to tackle the problem, discussing both its quirks and limitations.

As an addendum, in the last chapter of this thesis, we study the problem of characterizing the Darcy's law of non-Netwonian yield-stress fluids. The standard Darcy law [19] is a linear law describing flow rate vs pressure characteristics of a Netwonian fluid in a porous material. However when non-Netwonian fluid are involved, such as yield-stress fluids, the Darcy'law becomes non-linear in the applied pressure. In this chapter we use the tools of disordered systems and statistical physics to describe the flow by employing a mapping to a well known and studied problem, the directed polymer in random media. In literature, a porous material is modelled as a network where the fluid flows in its links. In this chapter we solve analytically the flow in a model where the porous material is modelled as a binary tree. This allows us to unveil the links between the non-linearity of the Darcy's law

and the geometrical organization of the flow in the medium.

Each chapter is based on a different paper:

- Chapter 1: based on "Statistical properties of avalanches via the c-record process" [14]
- Chapter 2: based on "Earthquake-like dynamics in ultrathin magnetic film" (in preprint) [20]
- Chapter 3: based on "Assessing the predictive power of GPS-based ground deformation data for aftershocks forecasting" (in preprint) [21]
- Chapter 4: based on "Darcy's law of yield stress fluids on a tree-like network" [22]

Chapter 1

Records, stick-slip motion and aftershocks

This chapter is based on the published paper *Statistical properties of avalanches via the c-record process* on Physical Review E (Phys. Rev. E 104, 064129) and on not-yet-published results regarding the same topic.

1.1 . Stick-slip motion

Stick-slip motion refers in general to a phenomenon occurring when two surfaces are in contact and moving one past the other. Stick-slip is observed, for example, when a car moves on a wet road, a violin bow acts on a string or in the topical example of tectonic plates that slide in a seismic fault [5]. As the name suggests, stick-slip motion is a type of motion where the object involved is either at rest or undergoes a (fast) movement and the main ingredient regulating these two phases is friction. The physical picture goes as following: an object is subject to some applied force and the static friction impedes the motion; as long as the friction is high enough the object remains still (it *sticks*). Then when the applied force is high enough to overcome friction, the object starts to move (it *slips*) only to (possibly) be stopped again by friction. Due to the alternant nature of the stick-slip motion, the two main observables that characterize it are:

- The slip size corresponds to the amount of displacement the object has undergone during the slip phase.
- The time correlation between subsequent slip events.

In the present context, we will focus on stick-slip motion in seismic phenomena and

its modeling. In doing so, we would like to maintain the main features of seismic events:

- Earthquake magnitudes m distribution $P(m)$ is well described by the Gutenberg-Richter (GR) law $P(m) \sim 10^{-bm}$. The GR law corresponds to an energy release (called seismic moment) during an earthquake of $M_0 \sim 10^{\frac{3}{2}m}$. Moreover, $M_0 \propto AD$, where A is area of the fault that slipped and D the slip size. The exponential nature of GR law translates to a power law distribution for M_0. In the context of stick-slip motion, the energy release happens during the slip phase thus by measuring the slip size we measure the energy release and thus the magnitude.

- The smaller earthquakes following a significant seismic event, called aftershocks, are correlated for a long time and this correlation is well described by the Omori-Utsu law [23], stating that the number of aftershocks $N(t)$ after a time t from a large earthquake decays as $N(t) \sim 1/t^p$ with $p \sim 1$.

The main framework we are going to use to model stick-slip motion is the spring-block model. It consists of an object (i.e., the block) of mass m subject to static and dynamic friction and pulled by a spring whose loose end moves at a constant velocity v_d. If the coordinate of the mass is x, we denote by $u = x - v_d t$ the spring elongation. Its equation of motion is:

$$m\ddot{u} = -cu + F_d \quad \text{if } u > F_s c \tag{1.1}$$

here F_s is static friction, F_d is dynamic friction $F_d < F_s$, c is the spring stiffness. If the block is stuck at some position x_0 because of friction, the force on u has to reach F_s which happens when a time Δt passes:

$$\begin{aligned} c(v_d \Delta t - x_0) &= F_s \\ \Delta t &= \frac{F_s + cx_0}{cv_d} \end{aligned} \tag{1.2}$$

At the beginning of motion, $\dot{u} = 0$ and u evolves as (we set the origin of time as the moment of the beginning of motion):

$$\begin{aligned} u(t) &= \left(\frac{cu_0 - F_d}{c}\right)\cos(\omega_0 t) + \frac{F_d}{c} \\ \dot{u}(t) &= -\omega_0 \left(\frac{cu_0 - F_d}{c}\right)\sin(\omega_0 t) \end{aligned} \tag{1.3}$$

So $u(t)$ will change until it reaches again zero velocity and thus the stick phase begins again. This simple model while displaying the essential feature of stick-slip motion, namely the intermittency between the two phases, lacks one major ingredient which is heterogeneity in the friction observed in real systems [6,24,25]. Indeed the motion is perfectly periodic as the value of the static friction remains constant throughout the dynamics. For a more realistic system, it is essential to exhibit variations in both the duration and friction force levels during different stick and slip phases. In order to do so we introduce a more realistic description: a block driven by an elastic spring in a random frictional landscape. Numerous representations of this model can be found in the literature; however, for our reference material, we rely on the comprehensive study conducted in [26]. The model consists of an overdamped particle (the block, in our case) pulled by a spring whose loose end is fixed at some position w. Thus the equation of motion reads:

$$\eta\dot{x}(t) = c(w - x(t)) + F[x(t)] \tag{1.4}$$

here $F[x(t)]$ incorporates the effect of friction and is, in general, a random variable. As pointed out in the original literature [26], instead of treating $x(t)$ as a continuous variable, it is more effective to discretize the motion in space and put the block on a lattice. Using a lattice spacing of 1 and indicating with i the lattice position, in this approximation the force applied on the block can be written as:

$$c(w - i) - f_i \tag{1.5}$$

where f_i is the friction value at site i. We implement the following rules of motion: if at some site i we have $c(w - i) > f_i$ the block can move by hopping from one lattice site to the next until at some site $i + n$ it encounters an high enough friction force such that $c(w-(i+n)) < f_{i+n}$. We refer to the friction value that stopped the motion as a *stopping force*. Overall during the motion - which is nothing but the slip phase - the block moves by n steps and its force drops by cn. As the friction stopped the motion, the block now is in the stick phase and to trigger a new slip phase the loose end of the spring w must change by a Δw such that:

$$c(w + \Delta w - (i + n)) = f_{i+n} \tag{1.6}$$

i.e., the applied force must reach the friction force. Suppose now that the friction value at each site is independent of the other and follows a distribution $p(f)$ with cumulative $P(f)$. At fixed w, the probability to find the block at position n in the lattice is:

$$P(n|w) = (1 - P(c(w - n)) \prod_{i<n} P(c(w - i)) \tag{1.7}$$

with $i < n$ indicating all the lattice points before n. The formula above is easily understood: the right term expresses the probability that at each site i smaller than n the applied force must be greater than the friction while the term $1 - P(c(w-n))$ expresses the probability that exactly at position n friction wins. The above formula can be generalized to take into account the probability of being stopped at site n with a stopping force less or equal to some value f:

$$P(n, f|w) = (P(f) - P(c(w-n)) \prod_{i=0}^{n-1} P(c(w-i))\theta(f - c(w-n)) \tag{1.8}$$

Finally we can turn equation (1.8) into a recursive equation for stopping forces. If, say, the particle was stuck at some position i with a stopping force f_0 and we want to know the probability of being stuck again at $i+n$ with a stopping force at least f, we need to consider:

$$P(f, n|f_0) = (P(f) - P(f_0 - cn)) \prod_{i=1}^{n-1} P(f_0 - cn)\theta(f - (f_0 - cn)) \tag{1.9}$$

To obtain it one has to use the fact that at site i the particle starts the motion as soon as its internal force is f_0 and after each step forward it takes the force drops by c. So the force must be higher than the friction for $n-1$ steps hence the term under the product and at step n, when the force reaches $f_0 - cn$, it has to be overcome by friction. As already pointed out, this model has been analyzed in [26] for various types of distributions $p(f)$. For our purpose, we need to remember two main results for this model:

- The marginal distribution for the slip sizes n is exponential $\pi(n) \sim \exp(-n/n_0)$ with n_0 a value depending on c and $p(f)$ (as long as we consider non fat-tailed distributions).

- The slip sizes are *uncorrelated* in time.

While this model lacks in reproducing the power-law distributed slip sizes observed in earthquakes (and thus related to the GR law), it has remarkable application in describing DNA unzipping as shown in [27]. Finally the uncorrelated nature of the slip events cannot properly describe aftershocks correlation, which is the second aspect of seismic phenomena we would like to retain.

1.2 . Connection with record statistics

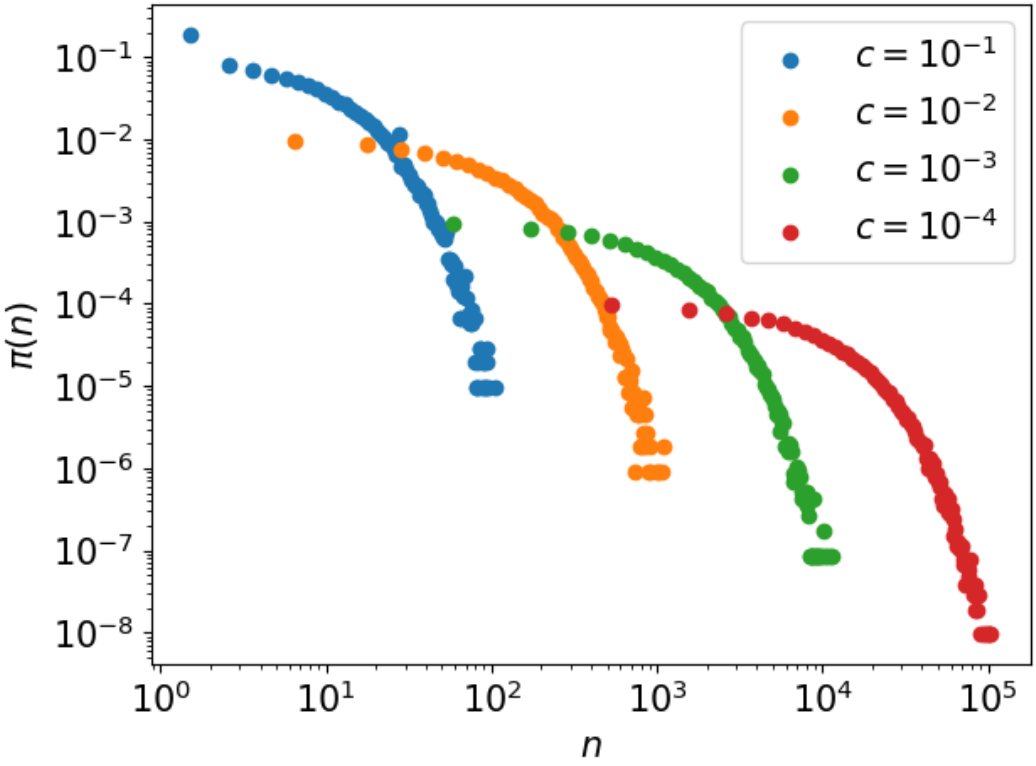

Figure 1.1: Probability distribution $\pi(n)$ for the slip sizes of the discretized driven particle model for $p(f) = \exp(-f)$ and various c. It is evident the exponential nature of $\pi(n)$ as proven in [26].

There is a deep connection between models for stick-slip motion and record statistics. Consider for a moment the case $c = 0$ in equation (1.9). It reads:

$$P(f, n|f_0) = (P(f) - P(f_0)) \prod_{i=1}^{n-1} P(f_0)\theta(f - f_0) = (P(f) - P(f_0))P^{n-1}(f_0))\theta(f - f_0) \tag{1.10}$$

For $c = 0$ one can immediately recognize that the equation (1.9) reduces to the probability of finding $n - 1$ numbers smaller than f_0 and one between f_0 and f among n i.i.d. random variables with cumulative $P(f)$ or, in other words, is the cumulative distribution of the maximum of n random variables conditioned on being also larger than f_0. As originally we were dealing with frictional forces on a lattice, we can imagine that the f_i's are spatially ordered by lattice site i. We can also say that, up to position n, equation (1.10) is the conditional record distribution for a collection of i.i.d. random variable. What is a record, though? The name speaks for itself, as it is defined as the largest value encountered in a time series (or spatial series, as in our case) up to some time (or position) n. If say, the last record was f_0,

equation (1.10) expresses the probability that the new record will be smaller than f and attained after n steps from f_0. Now we can plug back a $c > 0$ and interpret (1.9) in terms of record statistics. Indeed we can read equation (1.9) as a *modified* record problem where each time we encounter a new value in the time/spatial series we *relax* the condition of finding a record, namely we discount the record by a constant value c. Hence, after 1 step from f_0, we find a record if our new value f_1 is larger than $f_0 - c$, after 2 steps if f_2 is larger than $f_0 - 2c$ and so on. As we diminish the value of record to beat, effectively it is *easier* to find a new record for $c > 0$. This problem in the literature has been regarded as records for linear-trended time series and we refer to [28–30] for the original literature. In the next section, we review the main results on record statistics of i.i.d. series.

1.3 . Classical record statistics

We are ready now to formulate more precisely the concept of record statistics. Consider an infinite time/spatial series of values $\{f_i\}_{i=1}^{\infty}$. We stick to infinite time series as it greatly simplifies the calculations without losing the main features. We refer to i as the series index and f_i as the series value. Up to index $N \geq 1$, the *record* is the largest value in the series $f_1, f_2, \ldots, f_N$. As we consider larger N, the number of records can either increase or stay constant. We indicate with M_N the number of records up to index N and we label the indices at which the M_N record occurs as $i_1, i_2, \ldots, i_k \ldots i_{M_N}$ with $i_1 = 1$ by convention. The record values are thus labelled by $R_1, R_2, \ldots R_k, \ldots R_{M_N}$ and they correspond to the series values $f_{i_1}, f_{i_2}, \ldots f_{i_k}, \ldots R_{i_{M_N}}$. Finally, an important quantity, especially in connection with the physical problem, is the so-called *record age* defined as the difference between two consecutive record locations i.e. $n_k = i_{k+1} - i_k$ is the age of the k-th record. Figure 1.2 shows a pictorial representation of these quantities. In the next sections we describe record statistics for series of i.i.d. random variables and for linear-trended series, as they connect directly to the block model discussed above.

1.3.1 . IID Random variables

Classic results about record statistics can be easily obtained when considering a series of i.i.d. random variables i.e. the values f_i are drawn independently from a distribution $p(f)$ with cumulative $P(f)$. First of all we consider the so-called record rate which is the probability that the N-th value is a record. As we are dealing with i.i.d. series, all the values f_i are equally likely to be the record, this probability is uniform in N

$$p_N = \frac{1}{N} \tag{1.11}$$

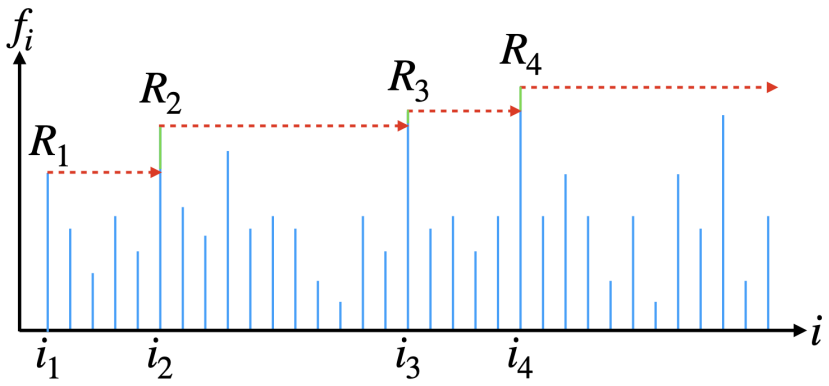

Figure 1.2: A realization of the classical record statistics. The vertical blue lines represent the series values f_i and we label the record both by their values and the index at which they occur.

Using this argument we can also say that, up to index N, the expected number of records is:

$$\sum_{n=1}^{N} \frac{1}{n} = \ln N + \gamma + o(1/N) \tag{1.12}$$

with $\gamma \approx 0.577215$ the Euler-Mascheroni constant. Consider now the joint probability that there are M records up to index N and the record has value R:

$$P_N(M, R) = P_{N-1}(M, R)P(R) + p(R) \int_{R'<R} dR' P_{N-1}(M-1, R') \tag{1.13}$$

The formula is read as follows: M records can formed at index N if at index $N-1$ no record has formed which happens with probability $P(R)$ where R is the last record value or if at index $N-1$ and a new record is formed with value R distributed according to $p(R)$ with probability given by $\int_{R'<R} dR' P_{N-1}(M-1, R')$. It can be shown that the generating function of $P_N(M, R)$, namely:

$$G(z, s, R) = \sum_{N=1}^{\infty} \sum_{M=1}^{\infty} z^N s^M P_N(M, R) \tag{1.14}$$

satisfies the following integral equation:

$$G(z, s, R)[1 - zP(R)] = zsp(R) \left[1 + \int_{R'<R} G(z, s, R')dR'\right] \tag{1.15}$$

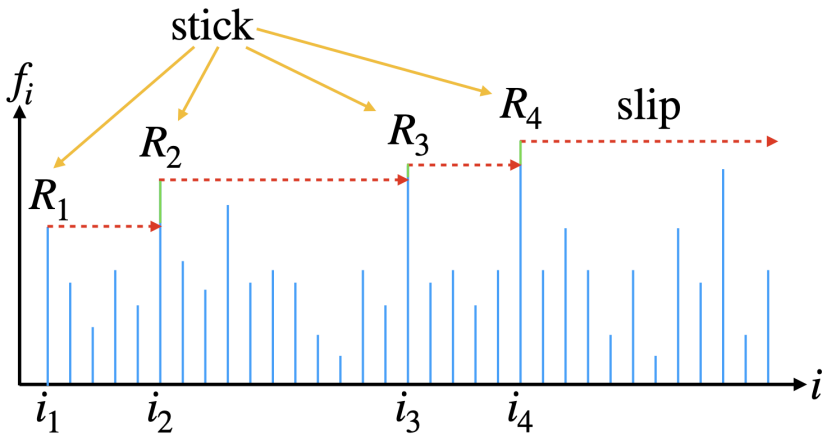

Figure 1.3: Stick-slip interpretation of the classical record statistics. The frictional landscape f_i is depicted by vertical blue lines indexed by the lattice site i. The records for the series $\{f_i\}_{i=1}^{\infty}$ are indicates by $R_1, R_2, \ldots$ at positions $i_1, i_2, \ldots$. These positions correspond to the position at which the system is stuck (stick phase). In the slip phase, which happens between two consecutive records, the force profile remains constant (red dotted lines). With small green segment we indicate the amount of force the system has to gain to start slipping again and each time is equal to $R_2 - R_1, R_3 - R_2, R_4 - R_3 \ldots$ i.e. is the difference between two consecutive record value.

Considering $H(R) = \int_{R'<R} G(R')dR'$ (we omit z and s for simplicity) we can show that:

$$H(R) = -1 + (1 - zP(R))^{-s} \tag{1.16}$$

By taking $R \to \infty$ (or, in general, R as the right limit of the support for $p(R)$) we obtain the generating function for the probability $P_N(M)$ of having M records up to index N:

$$G(z, s) = \lim_{R\to\infty} G(z, s, R) = (1 - z)^{-s} - 1 \tag{1.17}$$

Using $G(z, s)$ we can easily find that the expected number of records $\langle M_N \rangle$ which in the large N limit reads:

$$\langle M_N \rangle = \ln N + \gamma + O(1) \tag{1.18}$$

that is the result derived at the beginning of the section. As the generating function $G(z, s)$ does not depend on the type of distribution considered, the statistics for the number of records M_N is *universal*. The same is not true when one focuses

on the distribution of the k-th record value which we denote by $q_k(R)$ and depends explicitly on the form of $p(f)$. It can be shown that it satisfies the following recursive relation:

$$q_k(R) = p(R) \int_{R'<R} dR' \frac{q_{k-1}(R')}{1 - P(R')} \tag{1.19}$$

where the integral is understood has going from the left support of $p(f)$ up to R. By introducing a new generating function:

$$\tilde{q}(y, R) = \sum_{k=1}^{\infty} q_k(R) y^k \tag{1.20}$$

we can obtain an integral equation for it:

$$\tilde{q}(y, R) = yp(R) \int_{R'<R} dR' \frac{\tilde{q}(y, R')}{1 - F(R')} + yp(R) \tag{1.21}$$

with solution:

$$\tilde{q}(y, R) = yp(R) e^{-y \ln(1-P(R))} \tag{1.22}$$

The generating function corresponds to the following form for $q_k(R)$:

$$q_k(R) = \frac{p(R)}{(k-1)!} \left[-\ln(1 - P(R))\right]^{k-1} \tag{1.23}$$

Finally we can compute the distribution of the k-th age. Omitting the details of the computation we get:

$$\pi_k(n) = \frac{1}{(k-1)!} \int_0^1 dx (1-x) x^{n-1} \left[-\ln(1-x)\right]^{k-1} \tag{1.24}$$

which at variance to $q_k(R)$ is universal. For large k it can be also shown that $\pi_k(n) \sim 1/n$ which is non-normalizable. As we discussed now the key elements of records of i.i.d. series, we can back to the stick-slip motion interpretation. Records for i.i.d. time series thus correspond to a stick-slip model where the 'block' is stuck at record positions $i_1, i_2, \ldots$ and the blocking forces correspond to record values $R_1, R_2, \ldots$. Moreover the blocking force grow each time and they are distributed according to $q_k(R)$. To make this more clear, figure 1.3 has a schematics were the mapping is further explained and in the table below where this mapping is summarized.

records	**stick-slip motion**
series index i	lattice position
series values f_i	friction forces
record age $n_k = i_k - i_{k-1}$	displacement in the slip phase / slip size
record value $r_k = f_{i_k}$	stopping force

1.3.2 . Linear-trended series

As we treated record statistics for i.i.d. series and its connection to the case $c = 0$ driven particle model, we focus now on so-called linear-trended time series which is mapped to the $c \neq 0$ case. It consists in finding the records of the following series:

$$\tilde{f}_i = f_i + ci \tag{1.25}$$

where c is a constant and the $\{f_i\}_{i=1}^{\infty}$ are a series of i.i.d. random variables. For $c = 0$ it reduces to the classical records discussed above. Let's start by analyzing the record condition. If, say, some previous record occurred at index i_k with value $\tilde{R}' = f_{i_k} + ci_k$ the new record $\tilde{R}$ will occur at index i_{k+1} if:

$$\begin{aligned} &f_i + ci < f_{i_k} + ci_k \text{ for } i_k < i < i_{k+1} \\ &f_{i_{k+1}} + ci_{k+1} > f_{i_k} + ci_k \end{aligned} \tag{1.26}$$

The first line can be recast to $f_i < f_{i_k} - c(i - i_k)$ and the second to $f_{i_{k+1}} > f_{i_k} - c(i_{k+1} - i_k)$. So for $c > 0$, with respect to the case $c = 0$, it is *easier* to find a record while for $c < 0$ it is *harder*. We focus on the case $c > 0$ which has a direct mapping to the problem of the block pulled by an elastic spring. Indeed the two subsequent record locations i_k and i_{k+1} described above are nothing but the stick position of the block and the two values f_{i_k} and $f_{i_{k+1}}$ are the stopping forces. Moreover, if we say that $i_{k+1} - i_k$ is equal to some $n > 0$ and the initial applied force to the block was f_{i_k}, the applied force dropped by $cn = c(i_{k+1} - i_k)$ during the slip phase, as it happens for the block that moved by n steps. We have now two perfect correspondences, (1) between record values and stopping forces and (2) between record ages and displacement of the block/slip size. Hence, talking about record statistics and block model is effectively the same. An important feature of the linear trend record is that there exists a limiting distribution for the stopping force distribution. Namely, if we consider the k-th record and we take a very large k, the distribution for the stopping force can reach a limiting shape, depending on the type of distribution $p(f)$ (more precisely, depending on its extreme value class).

1.4 . A novel record model

As of now, it should be clear that stick-slip motion can be modeled using records and we presented two examples of such correspondence. In the following sections we present and analyze a novel record model that correctly reproduces two features of stick-slip motion observed in earthquakes, namely a power law distribution in slip sizes (and hence in record ages) and correlations between slip events. The model can

be understood informally by stating the record condition. Namely if the previous record is R' the next record value is the first element in the series R for which $R > R' - c$, with c a positive constant. This record condition is equivalent to a constant drop c in the applied force on the block after the slip phase starts. See figure 1.4 for a pictorial representation. Thus this model, which we dub c-record model, *interpolates* between the classical record model where there is no force drop (thus $c = 0$) and the linear-trend one (equivalent to the driven particle model) where the force drop is proportional to the slip size. This version of the c-record is not the only one interpolating but one could consider a protocol for which the force drop increase by c for each step the block makes up to a maximum number of steps $n_{\max}$, after which the force remains constant. The c-record corresponds to $n_{\max} = 1$. We will briefly discuss this variation at the end of the chapter but we anticipate that the main properties of the c-record model are maintained for any finite $n_{\max}$. We focus mostly on $n_{\max} = 1$ for analytical tractability. It is worth mentioning that this kind of modified record model was introduced in a different context, namely in study of fitness landscapes, in [31] without the explicit record interpretation.

1.4.1 . Definition

The definition of the c-record model is better carried out in a recursive way. Consider the usual series $\{f_i\}_{i=1}^{\infty}$ and label the record values as $R_1, R_2, \ldots, R_M \ldots$ and the indices at which they occur $i_1, i_2, \ldots, i_M, \ldots$. As the first record R_1 is always f_1, we have $i_1 = 1$. The successive records $R_2, \ldots, R_k, \ldots R_M \ldots$ are defined recursively:

$$R_k = f_{i_k} : f_{i_k} > R_{k-1} - c \quad \text{and} \quad f_i < R_{k-1} - c \quad i_{k-1} < i < i_k \tag{1.27}$$

In other words, a new record R_k is achieved when a value in the series f_{i_k} is larger than the old record value R_{k-1} minus a constant c. As for the other record models, we can introduce the record ages $n_k = i_k - i_{k-1}$ as a measure of how long a record lasts.

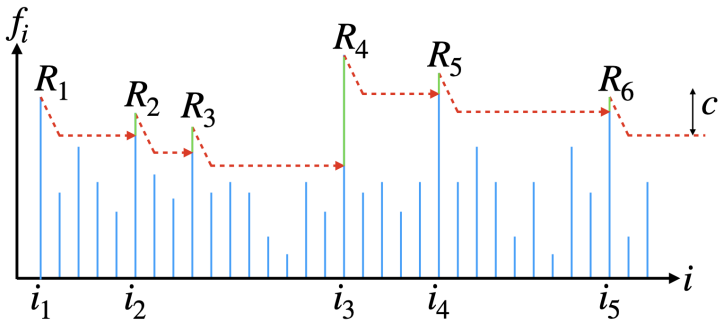

Figure 1.4: Pictorial representation of the c-record model. The solid vertical lines represent the friction values or equivalently the series $\{f_i\}_{i=1}^{\infty}$. The dashed red lines is the force profile during the motion. Solid green vertical lines indicate the force increase between the stick and the slip phase. The elbow-like shape of the force profile quantifies the effect of the force drop by c at the start of the slip phase.

The type of c-record we are going to focus on are those of i.i.d. series. In other words we are gonna consider a frictional landscape for our block with no spatial correlations. We expect from extreme value theory of correlated random variables [32–34] that these results won't be *qualitatively* affected in case of short-range correlation and will effectively change for strongly correlated random variables (such as a frictional landscape correlated as a random walk).

Calling $p(f)$ and $P(f)$ respectively the distribution and the cumulative of the elements of $\{f_i\}_{i=1}^{\infty}$, two successive records can be related using a conditional distribution. Fixing the value of a previous record to R', the new one will happen after n steps and will have value $\leq R$ with probability:

$$Q(n, R|R') = (P(R) - P(R' - c))P(R' - c)^{n-1}\theta(R - R' + c) \tag{1.28}$$

It is simple to understand equation (1.28): the new record will have a value R if for $n-1$ steps the values from the series are smaller than $R' - c$ and the n-th is larger than $R' - c$ and smaller than R. By taking a derivative w.r.t. R we can find the joint probability distribution of record age n and value R:

$$q(n, R|R') = p(R)P(R' - c)^{n-1}\theta(R - R' + c) \tag{1.29}$$

Equations (1.28) and (1.29) are valid for a distribution $p(f)$ with support on $\mathbb{R}$. We consider distributions limited from the left, e.g. with a support at $[0, \infty)$, the case

$n = 1$ changes depending on R':

$$q(n, R|R') = \begin{cases} p(R)P(R' - c)^{n-1}\theta(R - R' + c) & R' > c \\ \delta_{n,1}p(R) & R' < c \end{cases} \tag{1.30}$$

In the following sections, we will focus precisely on distributions with support $[0, \infty)$ which are the most interesting ones.

1.4.2 . Conditional distributions

In the case of limited support from the left, i.e., $[0, \infty)$, we can sum over the age value n in (1.30) and obtain the conditional distribution of record values:

$$q(R|R') = p(R)\theta(c - R') + \frac{p(R)}{1 - P(R' - c)}\theta(R - R' + c)\theta(R' - c) \tag{1.31}$$

The first term in the equation corresponds to the case $n = 1$ we mentioned before. By the same reasoning, by integrating over R we can find the conditional probability for the record age, which we call $\pi(n|R')$:

$$\pi(n|R') = \begin{cases} \delta_{n,1} & R' < c \\ (1 - P(R' - c))P(R' - c)^{n-1} & R' > c \end{cases} \tag{1.32}$$

The interpretation for $\pi(n|R')$ is straightforward: if $R' < c$, the next value in the series is a c-record, otherwise for $R' > c$, the age random variable n follows a geometric distribution. We can use equation (1.31) to efficiently simulate c-records if it is possible to apply the inverse transform sampling method for the distribution $p(f)$. Indeed, given previous record R', R is distributed according to (1.31) which can be interpreted as the distribution R drawn from $p(R)$ conditioned on being larger than $R' - c$. Hence if we can invert $P(f)$ we can sample R as follows:

$$R = \begin{cases} P^{-1}(P(R' - c) + u(1 - P(R' - c))) & R' > c \\ P^{-1}(u) & R' < c \end{cases} \tag{1.33}$$

where u is a uniform random variable in $[0, 1]$.

1.5 . Record value distribution

We are now ready to write equations for $q_k(R)$, namely the probability distribution of the k-th record. Using $q(R|R')$ it is possible to relate $q_k(R)$ to $q_{k-1}(R)$:

$$q_k(R) = f(R)\int_0^c q_{k-1}(R')dR' + f(R)\int_c^{R+c} \frac{q_{k-1}(R')}{1 - F(R' - c)}dR' \tag{1.34}$$

The first term corresponds to the case when the previous record has a value smaller than c (that happens with probability $\int_0^c q_{k-1}(R')dR'$). On the other hand the second terms comes from the case of a previous record larger than c. If we differentiate (1.34) w.r.t. to R

$$q_k'(R) = f'(R)\int_0^c q_{k-1}(R')dR' + f'(R)\int_c^{R+c} \frac{q_{k-1}(R')}{1-F(R'-c)} + f(R)\frac{q_{k-1}(R+c)}{1-F(R)} \tag{1.35}$$

and combine (1.35) with (1.34) we obtain a differential equation for $q_k(R)$:

$$q_k'(R) = \frac{f(R)}{1-F(R)}q_{k-1}(R+c) + \frac{f'(R)}{f(R)}q_k(R) \tag{1.36}$$

Equation (1.36) can be used to find a solution for $q_k(R)$ self-consistently with (1.34).

1.5.1 . Limiting distribution

Solutions for the recursive equation (1.35) are highly non-trivial and they can be carried out for a few distributions. An interesting question though is the existence of a *limiting* distribution $\lim_{k\to\infty}, q_k(R) \equiv q(R)$ for the record value. The answer depends on the behavior for large f of $p(f)$. Indeed in [14] it was shown that for a distribution with a stretched exponential tail $p(f) \sim e^{-f^\gamma}$ f $to\infty$ $q(R)$ exists for any $c > 0$ as long as $\gamma > 1$. Conversely for $\gamma < 1$ $q_k(R)$ does not have a well-defined limit and like in the classical record case, the record grows indefinitely without a limiting form. In figure 1.5 we show the average record for $\gamma > 1$ along with a predicted scaling for it in the $c \to 0+$ limit. The case $\gamma = 1$, which corresponds to pure exponential tail, is special and must be treated on its own. In the following sections, we are indeed gonna specialize to this case and we will choose the exponential distribution as a proxy $p(f) = e^{-f}$, due to its analytical tractability.

1.6 . The exponential distribution

As we anticipated in the previous section the c-records for the exponential distribution represent a limiting case for the existence of a stationary record distribution $q(R)$. Focusing on $p(f) = e^{-f}$, the equations for the record distributions become:

$$q_k(R) = e^{-R}\int_0^c q_{k-1}(R')dR' + e^{-R}\int_c^{R+c} q_{k-1}(R')e^{R'-c}dR' \tag{1.37}$$

$$q_k'(R) = q_{k-1}(R+c) - q_k(R) \tag{1.38}$$

The solution for $q_k(R)$ has been found in [31] by a power-series expansion suggested from solving the simple cases $k = 2, 3$ with initial condition $q_1(R) = e^{-R}$:

$$q_k(R) = -\frac{d}{dR}\left(\sum_{n=0}^{k} R\frac{(R+cn)^{n-1}}{n!}e^{-R-cn}\right) \tag{1.39}$$

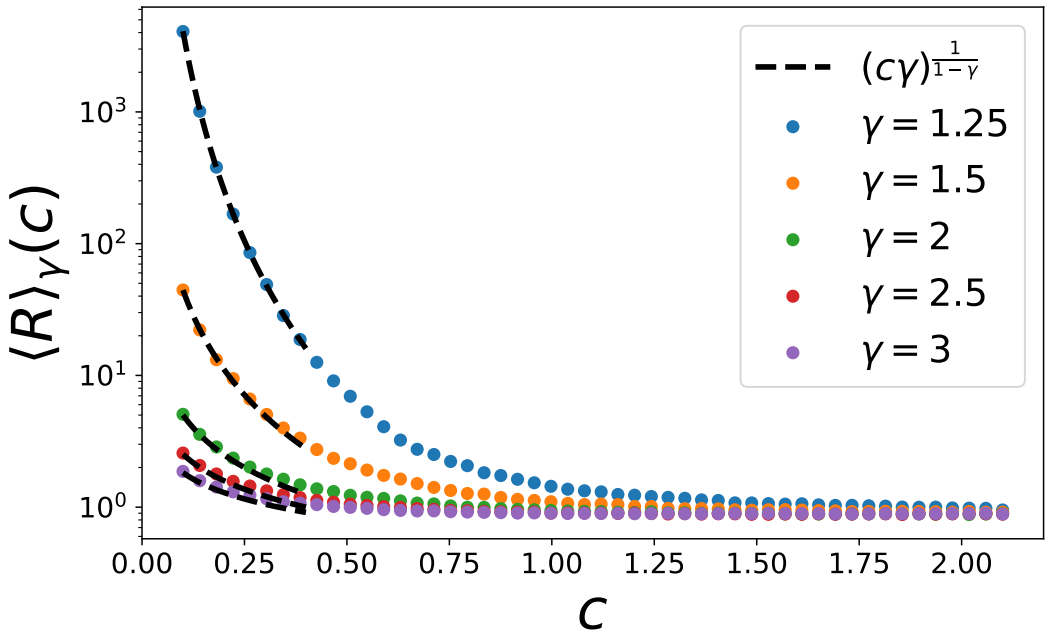

Figure 1.5: Average record extracted from exact numerical simulations and the scaling predicted for $c \to 0^+$. Simulations were carried out using the Weibull family $p(f) = \gamma f^{\gamma-1} e^{-f^\gamma}$. Figure from [14].

In the limit $k \to \infty$, the limiting distribution $q(R)$ satisfies:

$$q'(R) = q(R+c) - q(R) \tag{1.40}$$

This non-local equation has a simple solution:

$$q(R) = \lambda e^{-\lambda R} \tag{1.41}$$

with λ the solution of the self consistent equation:

$$\lambda = 1 - e^{-\lambda c} \tag{1.42}$$

One can always find such λ for $c > 1$. For $c \leq 1$ indeed the limiting distribution does not exists. This result can be also checked by inspecting directly the behaviour of $q_k(R)$ for large k. We thus identify a phase transition at $c = 1$. The effect of this transition can be seen either from the existence of the limiting distribution but also from counting the average number of records $\langle M \rangle_N$ in the first N elements of the time series:

$$\langle M \rangle_N = \begin{cases} \frac{1}{1-c} \ln N + O(1) & 0 \leq c < 1 \\ \ln^2(N) + O(\ln N) & c = 1 \\ A_0(c) N^\lambda + \frac{1}{1-c} \ln N + O(1) & c > 1 \end{cases} \tag{1.43}$$

with $A_0(c)$ a positive constant depending on c. We remind to the original work for an in-depth discussion and for the derivation of these results [14].

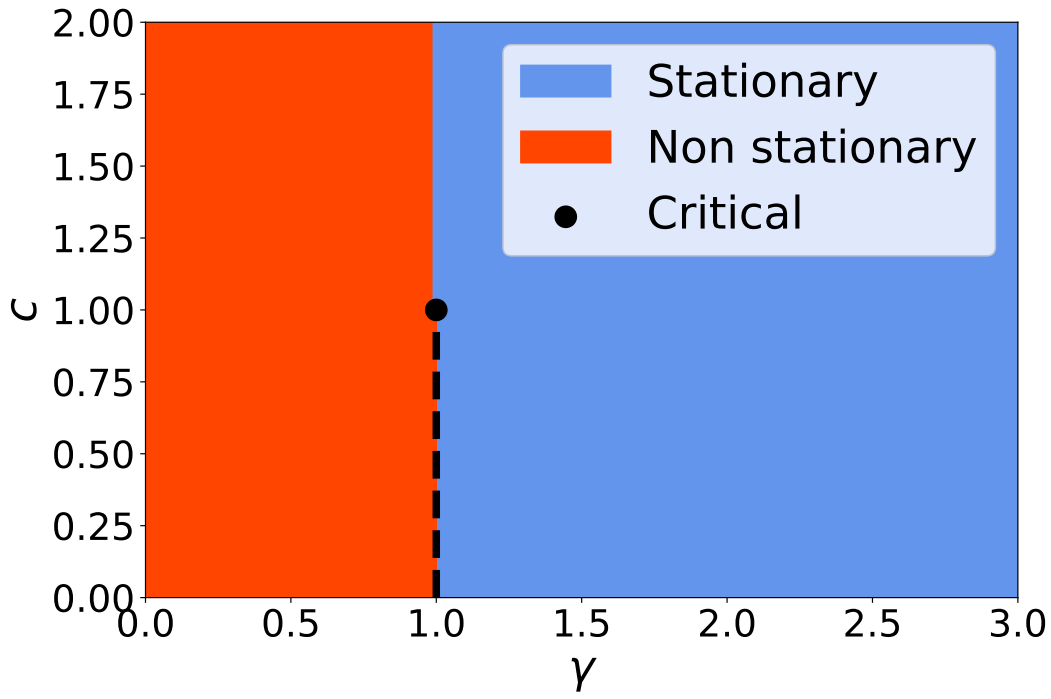

Figure 1.6: Phase diagram for the phase transition described in the text. The exponential distribution is a limiting case between the existence of a stationary record distribution. This phase diagram is specialized on the Weibull family $p(f) = \gamma f^{\gamma-1} e^{-f^\gamma}$.

1.6.1 . Age distribution

Having found the stationary record distribution for $c > 1$ we can also recover the stationary age distribution:

$$\pi(n) = \lim_{k\to\infty} \pi_k(n) \tag{1.44}$$

The age distribution $\pi_k(n)$ is obtained by using the conditional age distribution (1.32) in conjuction with $q_k(R)$:

$$\pi_k(n) = \int_0^\infty \pi_k(n|R) q_k(R) dR \tag{1.45}$$

In the limit $k \to \infty$, by using $q(R) = \lambda e^{-\lambda x}$, this corresponds to:

$$\pi(n) = \lambda \delta_{n,1} + \lambda(1-\lambda) B(n, \lambda + 1) \tag{1.46}$$

with $B(a, b)$ the Beta function $B(a, b) = \Gamma(a)\Gamma(b)/\Gamma(a + b)$ and $\Gamma(x)$ the gamma function. This prediction is confirmed by numerical simulations, see figure 1.7. For large n is it straightforward to show that:

$$\pi(n) \sim \lambda(1-\lambda)\Gamma(1+\lambda)/n^{1+\lambda} \tag{1.47}$$

This density is normalizable as long as $1 + \lambda > 1$ which is always the case for $c > 1$.

Going back to the mapping between the record model and the spring-block one, the age distribution corresponds to the slip size distribution and thus a power law in n corresponds to a GR law for the magnitude, here defined as $m \propto \log_{10} n$. This is in sharp contrast with the result for the age/slip size in the driven particle model presented before, where n has an exponential distribution. In the following section we investigate numerically the c-records of different probability distribution, with a particular focus on the Weibull family $p(f) = \gamma f^{\gamma-1} e^{-f^\gamma}$. We will show that the main feature of the exponential case in maintained, namely a power law in $\pi(n)$.

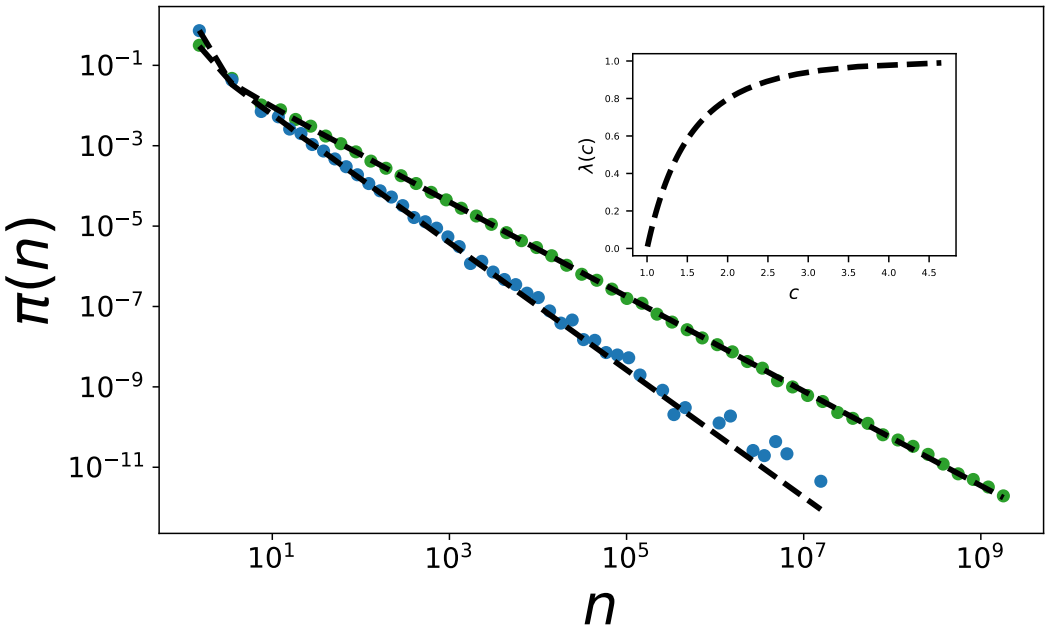

Figure 1.7: $\pi(n)$ for $c = 1.5$ (blue circles) and for $c = 1.1$ (green circles). Black dashed line corresponds to the analytical predictions of (1.46). The inset shows $\lambda(c)$ as a function of c.

1.7 . Numerical results on the Weibull family

As anticipated, the Weibull family of probability distributions is particularly suited for the simulations of c-records. By using equation (1.33) specialized for the Weibull family:

$$p(f) = \gamma f^{\gamma-1} e^{-f^\gamma} \tag{1.48}$$

$$P(f) = 1 - e^{-f^\gamma} \tag{1.49}$$

$$\tag{1.50}$$

we can write a stochastic equation relating two subsequent records:

$$R_k = (\eta_k + (R_{k-1} - c)_+^\gamma)^{1/\gamma} \tag{1.51}$$

where $(x)_+ = \max(x, 0)$ and η_k is a number with exponential distribution of mean 1 i.e. $p(\eta_k) = e^{-\eta_k}$. Equation (1.51) allows us to directly simulating the records without simulating the series $\{f_i\}_{i=1}^{\infty}$. This stochastic equation makes clear that, whenever $R_{k-1} < c$, the distribution of R_k will be the one of $\eta_k^{1/\gamma}$ which is precisely a Weibull. In figure 1.8 we show the record age distribution $\pi(n)$ for various c and

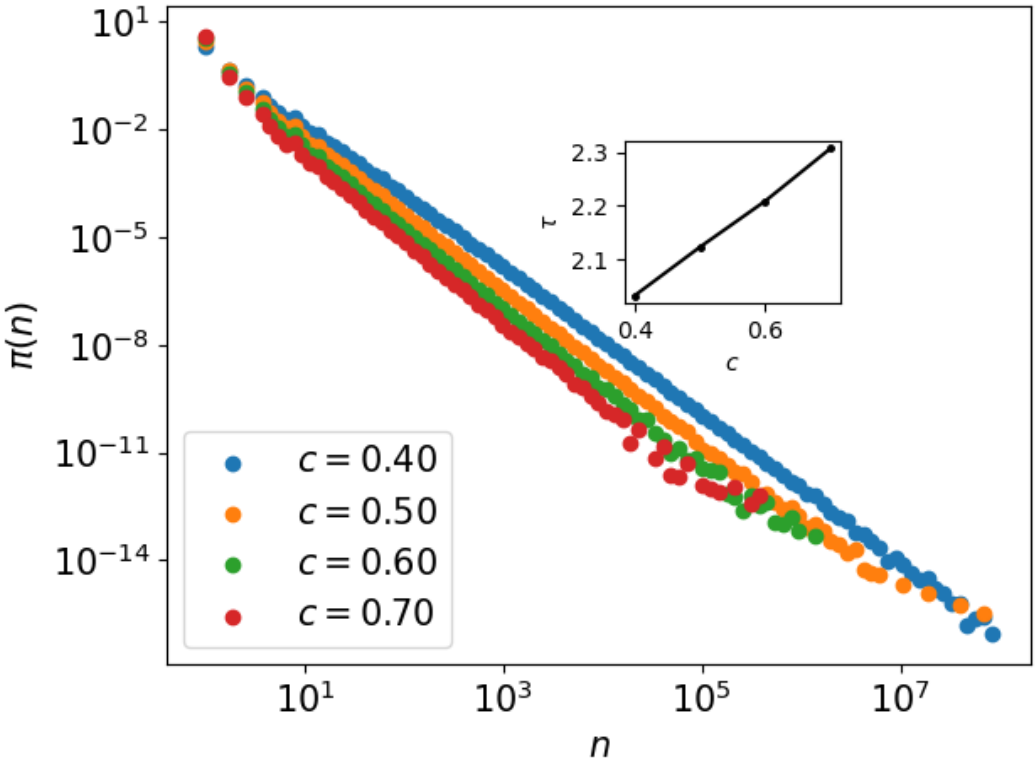

Figure 1.8: Ages distribution simulated using equation (1.51). In the inset we show how the exponent τ in $\pi(n) \sim n^{-\tau}$ varies with c.

$\gamma = 2$. In all cases the power law behaviour $\pi(n) \sim n^{-\tau}$ is maintained with $\tau > 1$. The analytical results on the exponential distribution joint with the numerics of the Weibull case (which are a representative of any distribution with a tail falling faster than an exponential) show how the c-records, in their spring-block interpretation, correctly reproduce the GR law. What is left to investigate now is the correlation between records. For the record values, it can be analytically carried out in the exponential case, while for the Weibull case we limit ourselves to numerics.

1.8 . Correlations and seismic sequences

In the case of distributions $p(f)$ with support limited from the left such as $[0, \infty)$, it is clear that from equation (1.30), when if some record R' is smaller than c, the next one R will have a value uncorrelated from R' and drawn from $p(R)$. In other words from the point of view of the record value, it is like the record value process *resets* as soon as a record reaches a value $\leq c$. As this is the case, we can separate the records in sequences, each stopped precisely by the record that reached a value $\leq c$.

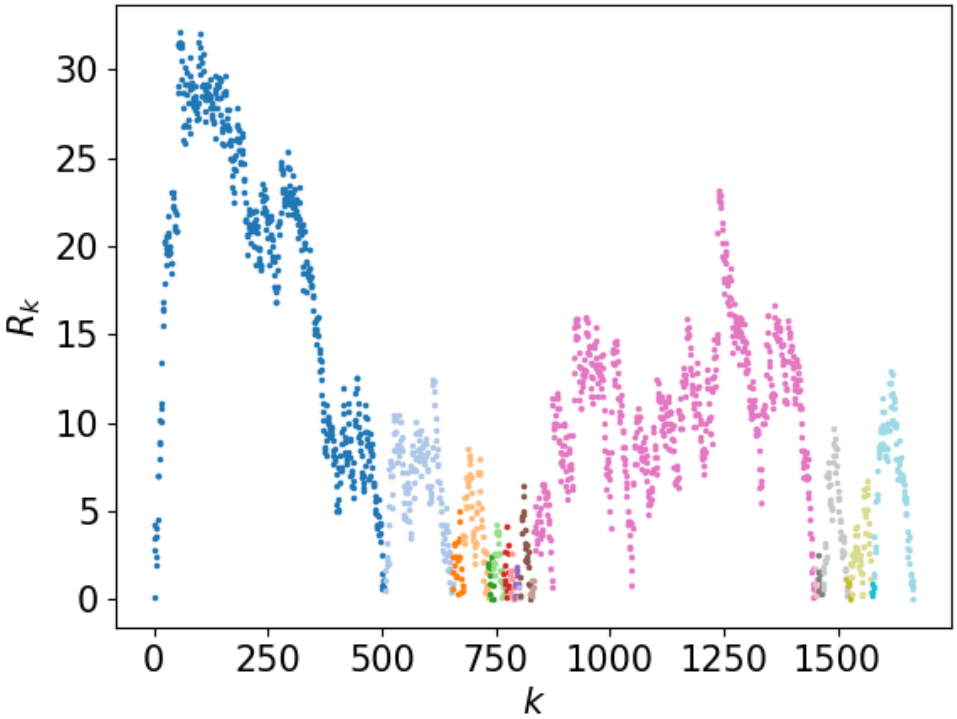

Figure 1.9: Example of different sequences for the c-record in the exponential case. Sequences are separated by the color. The record values are plotted to distinguish the sequences. Simulations are carried out at $c = 1.1$.

Focusing now on the exponential case, we can introduce a new quantity, namely the probability that $\ell - 1$ consecutive records had a value $> c$ and the last one is equal to R:

$$P_\ell(R) = \{\text{probability that } R_i \geq c \text{ for } i = 1 \dots \ell - 1 \text{ and } R_\ell = R\} \tag{1.52}$$

So $P_\ell(R)$ is a form of survival probability, when integrated over R. Indeed as a

sequence ends when the last record reaches a value $\leq c$, the sequence length distribution is obtained by:

$$P_\ell = \int_0^c P_\ell(R)dR \tag{1.53}$$

Using the conditional record value distribution (1.31) specialized to the exponential case we can relate $P_\ell(R)$ and $P_{\ell-1}(R)$:

$$\begin{aligned} P_\ell(R) &= \int_c^\infty q(R|R')P_{\ell-1}(R')dR' = \\ &= e^{-R-c}\int_c^{R+c} e^{R'}P_\ell(R')dR' \end{aligned} \tag{1.54}$$

For moderate ℓ, We can simply find the explicit form of the correspondent $P_\ell(R)$:

$$\begin{aligned} P_1(R) &= e^{-R} \\ P_2(R) &= Re^{-R-c} \\ P_3(R) &= \frac{R(R+2c)}{2}e^{-R-2c} \end{aligned} \tag{1.55}$$

By inspection one can realize that:

$$P_\ell(R) = e^{-(R+c(\ell-1))}\frac{R}{(\ell-1)!}(R+c(\ell-1))^{\ell-2} \tag{1.56}$$

Now by integrating over $R \in [0, c]$ we can find P_ℓ as defined above:

$$P_\ell = \int_0^c P_\ell(R)dR = \frac{1}{(\ell-1)!}\int_{c(\ell-1)}^{c\ell} e^{-z}z^{\ell-2}(z-c(\ell-1))dz \tag{1.57}$$

Equation (1.57) can be rewritten using the upper incomplete gamma function $\Gamma(s,x) = \int_x^\infty t^{s-1}e^{-t}dt$:

$$P_\ell = \frac{1}{(\ell-1)!}\left[(\Gamma(c(\ell-1),\ell) - \Gamma(c\ell,\ell)) - c(\ell-1)\left(\Gamma(c(\ell-1),\ell-1) - \Gamma(c\ell,\ell-1)\right)\right] \tag{1.58}$$

For large ℓ, P_ℓ can be shown to have the following asymptotics:

$$P_\ell \sim \mathcal{N}_c\frac{1}{\ell^{3/2}}e^{-\ell/\ell_{\text{co}}} \tag{1.59}$$

with $\mathcal{N}_c$ a c-dependent constant and ℓ_{co} cutoff length :

$$\ell_{\text{co}} = \frac{1}{c-1-\ln(c)} \tag{1.60}$$

Close to $c = 1$, ℓ_{co} diverges as:

$$\ell_{\text{co}} \sim (c-1)^{-\nu} \tag{1.61}$$

with $\nu = 2$. At the critical point $c = 1$, in accordance with standard critical phenomena, the cutoff length disappears and we find a pure power law:

$$P_\ell \sim \frac{1}{2\sqrt{2\pi}\ell^{3/2}} \tag{1.62}$$

In figure 1.10 we test this result numerically for various values of c finding perfect agreement.

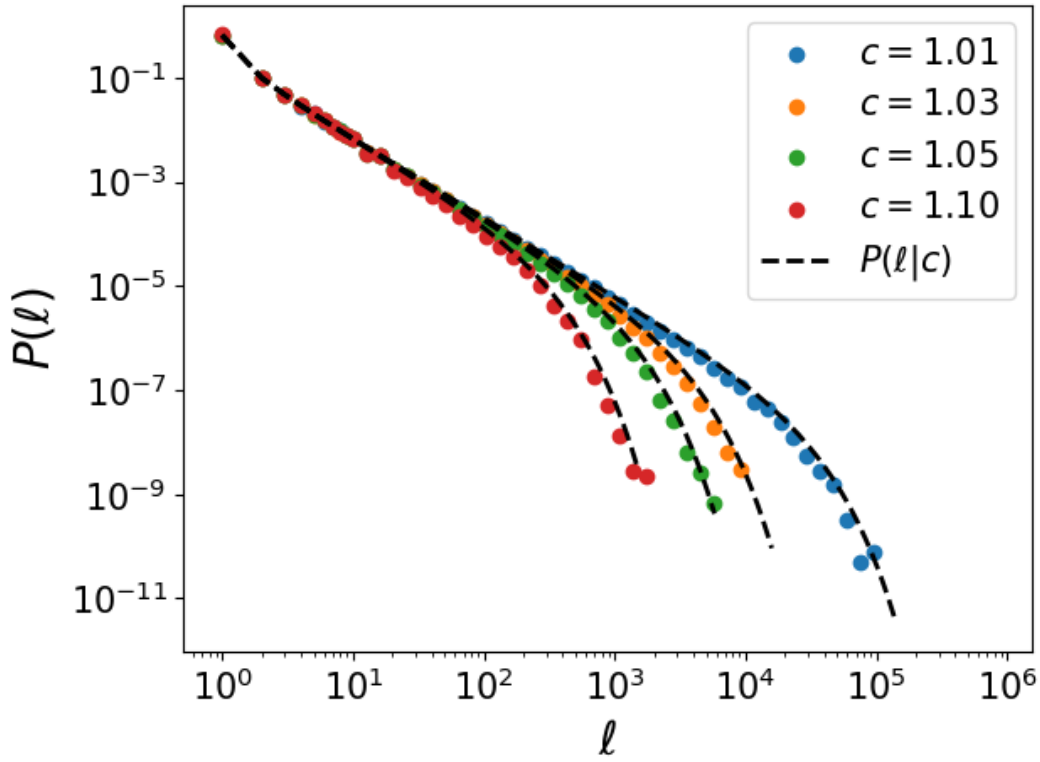

Figure 1.10: Sequence length distribution P_ℓ in the exponential case for various c. The dots are data from simulations, the black dashed line the analytical expression from (1.57). As expected the cutoff grows as c approaches 1.

The result on the sequence length is reminiscent of the first passage time in zero of a Brownian motion with a drift. Indeed we can interpret a sequence in terms of random walks. Consider again the stochastic equation for two subsequent records (1.51):

$$R_k = \eta_k + (R_{k-1} - c)_+ \tag{1.63}$$

with $\eta_k \sim e^{-\eta_k}$ and $(x)_+ = \max(x, 0)$. If a sequence lasts for ℓ, we have $R_1, \ldots, R_{\ell-1} > c$ and $R_\ell < c$. Hence for $k = 1, \ldots, \ell - 1$:

$$R_k = \eta_k + R_{k-1} - c \tag{1.64}$$

In the variable $z_k = R_k - c$ and introducing $\xi_k = \eta_k - 1$ we obtain:

$$z_k = 1 - c + z_{k-1} + \xi_k \tag{1.65}$$

This is an equation for a discrete time random walk with an asymmetric jump distribution $\xi_i \sim e^{-(\xi_i+1)}\theta(\xi_i+1)$, a drift $1-c$ and an absorbing boundary in $z=0$, corresponding to the end of sequence when $R \leq c$. Thanks to this mapping we expect that the first passage time of the random walker through zero or, equivalently, the length of the sequence of records, to have a distribution with a power law tail $P_\ell \sim \ell^{-3/2}$. The presence of drift introduces a cutoff $\ell_{\rm co}$ as in the standard first passage time of a Brownian motion [35]. As we already pointed out, the new record will have a value uncorrelated from the previous one and drawn from $p(f)$. In the language of Brownian motion, this mechanics corresponds to a Brownian particle which is reset after each passage though zero. This process is denoted as first passage stochastic resetting and has been studied, for example, in [36, 37].

The remarkable expression for (1.57) is only valid for the exponential case. When dealing with other distributions, such as the Weibull already mentioned, the situation changes and we lose the power law behavior. In either cases we manage to reproduce another feature of the real stick-slip motion and of earthquakes, namely a strong correlation between subsequent events.

1.9 . Variations of c-records

Various variation can be introduced of the c-record model [14].

For example one can generalize the new record criterion from $R_k > R_{k-1} - c$ to $R_k > R_{k-1} - h(R_{k-1})$ where $h_k(R)$ is some function, possibly k-dependent. Example are given in [38, 39].

Another example can be to take $h_k(R) = gR$, independent of k. The seismic/stick-slip interpretation of this model is that the loss in the applied force at the onset of the slip phase is proportional to the initial stopping force: the bigger the record, the bigger the loss. In this case the recursive record equation, analogous to (1.34), becomes:

$$q_{k+1}(R) = f(R) \int_0^{R/g} \frac{q_k(R')}{1 - F(gR')} dR' \tag{1.66}$$

If we consider a series $\{f_i\}_{i=1}^{\infty}$ with Weibull distribution $p(f) = \gamma f^{\gamma-1} e^{-f^\gamma}$, the associated stochastic equation for the record reads:

$$R_k^\gamma = g^\gamma R_{k-1}^\gamma + \eta_k \tag{1.67}$$

with η_k exponentially distributed with mean 1. In terms of $z_k = R_k^\gamma$ and $\alpha = g^\gamma$:

$$z_k = \alpha z_{k-1} + \eta_k \tag{1.68}$$

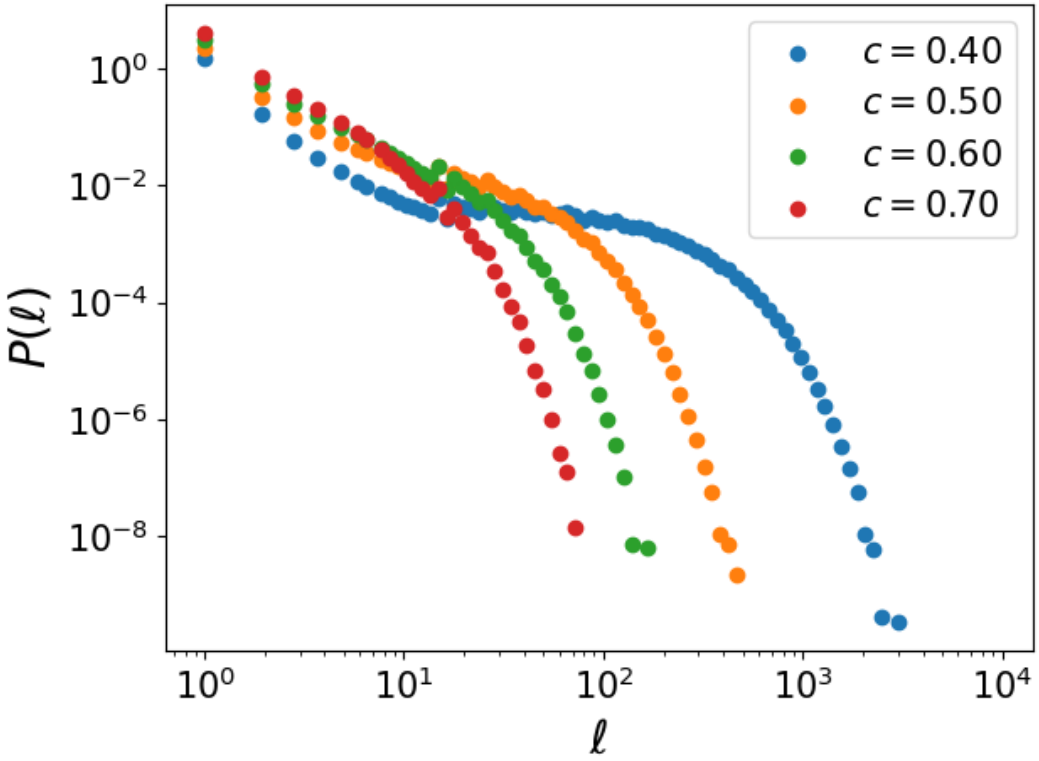

Figure 1.11: Sequence length distribution P_ℓ in the Weibull case with $\gamma = 2$ for various c. At variance with the exponential case, an exponential decay in P_ℓ dominates.

which has a solution:

$$z_k = \sum_{i=1}^{k} \eta_i \alpha^{k-i} \tag{1.69}$$

with average:

$$\overline{z_k} = \sum_{i=1}^{k} \alpha^{k-i} = \frac{1-\alpha^{k+1}}{1-\alpha} \tag{1.70}$$

Finally a possible generalization would be to promote c, in the c-record model, to a random variable. This kind of generalization would be more appropriate to model seismic phenomena then as a bona-fide modified record model.

1.10 . Conclusion

In this chapter we discussed the mapping between models of stick-slip motion and record statistics. By introducing a new record model, we managed to reproduce the main features of seismic catalogues. In particular, we recovered power law distribution of the slip size which is compatible with the GR law and a strong

correlation between record sequences, in accordance to the existence of aftershocks. We showed that the presence of these features are independent of the type of friction distribution employed but, at the same time, they become special when dealing with an exponential distribution. Naturally this kind of model has huge limitations as it ignores the spatial extent of the seismic fault and their elastic interactions. More realistically, in modeling such a system, driven elastic manifolds in quenched disorder (the frictional landscape) are often used. A large literature has been produced [4, 40–42], with more and more realistic models emerging in recent years [7].

Chapter 2

Earthquake-like dynamics in ultrathin magnetic films

This chapter is dedicated to the experimental study of the expansion of a domain wall in an ultra-thin magnetic film under the influence of a weak magnetic field. The reason behind the study of this magnetic system is that the dynamics of the wall have strong similarities with the correlated seismic dynamics of mainshocks/aftershocks. Indeed as in seismic phenomena, when one portion of the wall moves by a sufficient amount, it can trigger a cascade of events that are spatially and temporally correlated. The experiment is carried out at room temperature and at a very low magnetic field, resulting in a creep motion of the wall. Hence in the first part of this chapter, we are gonna review the creep regime observed in the motion of driven elastic interfaces in random media. In the second part, we carry out the data analysis of the experiment and compare it with the theoretical results.

2.1 . Driven elastic interfaces in random media

Domain walls in magnetic films can be described by one-dimensional interfaces embedded in a two-dimensional medium. As the medium contains impurities (magnetic defects, for example) the domain wall expansion is not regular, and the front has a rough nature. The simplest yet effective description of a domain wall is given by an interface $u(x,t)$ embedded in a random medium:

$$\gamma \partial_t u(x,t) = c\nabla^2 u(x,t) + F(x,u(x,t)) + f + \eta(x,t) \tag{2.1}$$

This model is referred to as quenched Edwards-Wilkinson (qEW) interface The first term 2.1 is the elastic force acting on the interface. One could include a non-linear KPZ term $\lambda(\nabla u(x,t))^2$, that emerges whenever some form of anisotropy is present [43] or when anharmonicity is relevant [44, 45]. We refer to this modified version as quenched Kardar-Parisi-Zhang (qKPZ) interface. Moreover, f is the driving force (equivalent to the driving magnetic field in the domain wall experiments), $\eta(x,t)$ is a thermal noise with correlations $\langle \eta(x,t)\eta(x',t')\rangle = 2\gamma T\delta(x-x')\delta(t-t')$ and $F(x,u(x,t))$ is a quenched disorder that models the impurities. The latter can be derived by a potential $V_P(x,u)$ as $F(x,u) = -\partial_u V(x,u)$, which is uncorrelated along the x direction. Instead, along the u axis, three different types of disorder emerge depending on the correlations of $V(x,u)$:

- Random Bond (RB) where the potential (and the force) are short-range correlated i.e. $\overline{[V(x,u)-V(x',u')]^2} = \delta(x-x')R(u-u')$ with $R(u)$ a function exponentially decaying.
- Random Field (RF) where the potential is long-range correlated e.g. $\overline{[V(x,u)-V(x',u')]^2} \propto \delta(x-x')|u-u'|$.
- Random Periodic (RP) where the correlator is a periodic function of u e.g. $\overline{[V(x,u)-V(x',u')]^2} \propto \delta(x-x')\cos(u-u')$.

The dynamical equation (2.1) is well suited for studying the driven interface i.e. $f > 0$. However, at zero driving force $f = 0$ and in the long-time limit, the problem reduces to study the thermodynamics of the equivalent system at temperature T. The Hamiltonian reads:

$$H = \frac{c}{2}\int dx(\nabla u(x))^2 + \int dx V(x,u(x)) \tag{2.2}$$

where the disorder potential has the same correlations described above.

2.2 . Theory: equilibrium

An interface in random medium is characterized by the competition between elasticity, which tends to flatten the interface, and disorder, which favors more irregular profiles. Such competition can result in a rough interface and this translates to the following structure for the fluctuations:

$$\overline{\langle [u(x)-u(x')]^2\rangle} \sim |x-x'|^{2\zeta} \tag{2.3}$$

Here the brackets stand for the thermal average, while the overline for the disorder one. The exponent $\zeta > 0$ is called the roughness exponent and measures the level of

roughness of the wall. Moreover a $\zeta < 1$ indicates that the fluctuations over a size $\ell \sim |x - x'|$ grow slower than ℓ grows. A $\zeta = 0$ corresponds to a flat interface. It is easier to first focus on the static case i.e. $f = 0$. The values taken by ζ can be found by using Flory estimates (first devised for self-voiding polymers). Such estimates start from the idea that roughness emerges when the elastic energy contributions and disorder one match. We consider for the moment the case of random bond disorder. In a system of linear size L the elastic part gives:

$$\int_x (\nabla u)^2 \sim L^{d-2} u^2$$

where u is the typical value of $u(x)$. The disorder part gives instead:

$$\int_x \sqrt{\delta^2 V} \sim L^d \sqrt{L^{-1} u^{-1}}$$

We equate the two contributions by using the scaling $u \sim L^\zeta$. It yields:

$$\zeta_{\text{RB,Flory}} = \frac{4-d}{5}$$

Repeating the same argument for the random field case we get $\zeta_{\text{RF,Flory}} = \frac{4-d}{3}$. In both cases for a dimension $d < 4$, $\zeta_{\text{Flory}} > 0$ and thus the interface is indeed rough. In the Renormalization Group (RG) sense, this implies that the disorder is relevant in any dimension smaller than 4. The Flory estimates are crude ones and yield wrong values for the roughness [46]. However, they manage to identify as $d = 4$ the upper critical dimension of the model and the fact that the RB and RF cases yield different values. A more refined analysis is due to Larkin [16, 47, 48]. Consider a subsystem of linear size ℓ at zero temperature. The discussion on a finite temperature $T > 0$ is delayed for the moment, and, as we will see, it won't change the arguments given here. Over a size ℓ, the interface has a typical displacement $w(\ell) \sim \sqrt{\overline{(u_\ell - u_0)^2}}$ and the elastic force can be estimated as $f_{\text{el}} \sim cw(\ell)/\ell^2$. Calling $\Delta(u) = -R''(u)$ the force correlator i.e. $\overline{F(x,u)F(x',u')} = \delta(x - x')\Delta(u - u')$, we can estimate the force due to disorder as $f_{\text{dis}} \sim \sqrt{\Delta(0)/\ell^d}$. Balancing the two we obtain:

$$cw(\ell)/\ell^2 \sim \sqrt{\Delta(0)/\ell^d}$$

Denoting by r_f the correlation length of the disorder, in any dimension $d < 4$ one identifies a length scale ℓ_c:

$$\ell_c = \left(\frac{c^2 r_f^2}{\Delta(0)}\right)^{\frac{1}{4-d}}$$

called the Larking length for which for any $\ell < \ell_c$:

$$w(\ell) \sim r_f \left(\frac{\ell}{\ell_c}\right)^{\frac{4-d}{2}}$$

This results in a rough interface at $\ell < \ell_c$. For $\ell > \ell_c$, the situation changes as the interface fluctuates beyond the correlation length r_f, and the interface can be seen as a series of pieces of length ℓ_c which are independently pinned by the disorder. The $\ell < \ell_c$ picture is confirmed by studying interface fluctuations and its roughness using perturbation theory in the context of the Function Renormalization Group (FRG) [16]. Beyond the Larkin length, indeed, a new roughness emerges different from $(4-d)/2$:

$$w(\ell) \sim r_f \left(\frac{\ell}{\ell_c}\right)^{\zeta_{\text{eq}}}$$

We denoted the roughness with ζ_{eq} as it is the large-scale roughness at equilibrium (statics) even though, at the moment, at zero temperature. The ζ_{eq} value depends on the disorder type (RB or RF). An exact solution is available for the RB case in $d = 1$ as, in this case the interface is exactly mapped to the ground state of the directed polymer in a random medium in $1+1$ dimensions, solved using the Replica Bethe Ansatz [49]. Such method yields $\zeta = 2/3$. The value slightly changes for the RF case and is obtained using perturbation theory [50]. Finally, we address the case of $T > 0$ while still considering statics $f = 0$. The static problem at any T exhibits Statistical Tilt Symmetry (STS), meaning that if we tilt $u(x)$ by a linear function i.e. $u(x) \to u(x) + ax$, it can be shown that the system has the same statistical properties (this can be shown using the replica approach, as discussed in [46]). The STS has deep implications on the properties of the theory as, in the RG sense, the elastic constant does not get renormalized by the presence of disorder. This implies that the ground state energy ($T = 0$), while being extensive $\propto L^d$, fluctuates as L^θ with $\theta = 2\zeta_{\text{eq}} + d - 2$ because of STS. Additionaly, Moreover, one can show that temperature is irrelevant in the RG sense [16] and the statics is dominated by the $T = 0$ physics. As such, we will refer to any $f = 0$ case as the *equilibrium* fixed-point [16, 46, 48, 51, 52], encompassing the whole $T \geq 0$ region.

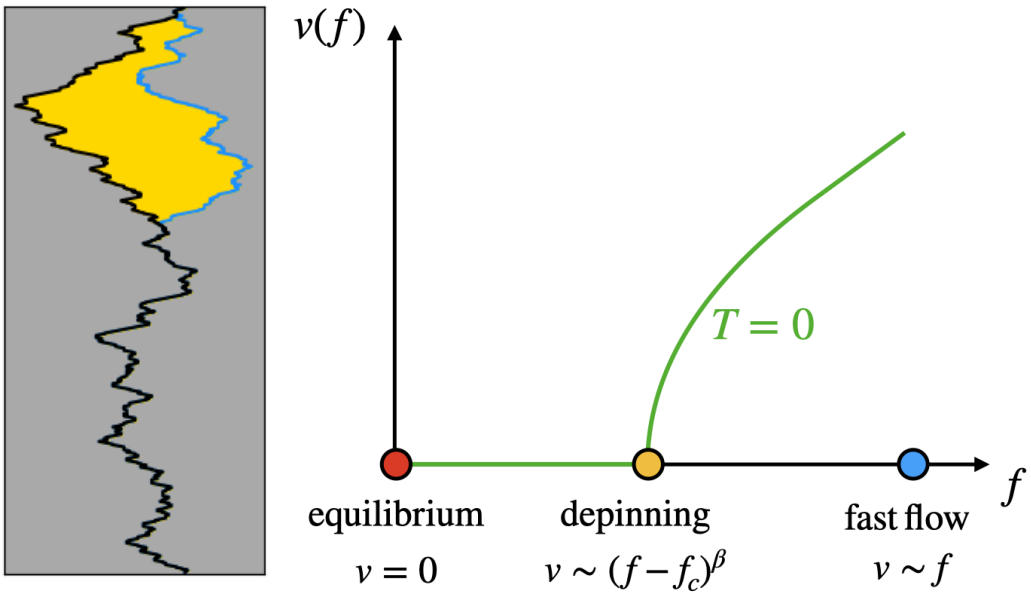

Figure 2.1: Left: avalanche as measured at f slightly below f_c following an increase δf. The black line represents the interface at f, while the yellow area is the avalanche after the increase $f \to f + \delta f$. Right: the zero-temperature characteristics of the velocity as a function of the driving force. At $f = 0$, the interface is at the equilibrium and is characterized by the equilibrium universality class. For $f = f_c$ the interface is at depinning. For $f \gg f_c$ the fast-flow regime kicks in and velocity becomes linear in f i.e. $v \sim f$. In this regime the quenched disorder acts like a thermal noise and the interface looks like an EW (or KPZ) thermal interface.

2.3 . Theory: depinning

The second regime relevant for interfaces in random media is the driven regime at zero temperature i.e. $f > 0$ and $T = 0$. In this regime, the interface undergoes a depinning transition for a f larger than some critical force f_c and it acquires a finite velocity, vanishing at f_c as:

$$v \sim (f - f_c)^{\beta} \tag{2.4}$$

where β is a known exponent [16, 50]. At depinning there is no difference between the RB and RF classes [16]. The statistical properties of a qEW interface at depinning are described by two independent critical exponents, the roughness ζ and the dynamical exponent z. The latter describe of the correlation time of the interface grows with system lateral size i.e. $t \sim L^z$. In $d = 1$, one finds $\zeta \approx 1.25$ and for $z = 1.43$, from which one can obtain $\beta = \frac{z-\zeta}{2-\zeta} \approx 0.31$. For later use, we also report the exponent ν describing the growth of the correlation length ζ as one approaches depinning i.e. $\xi \sim |f - f_c|^{-1/\nu}$ with $\nu = 1/(2 - \zeta)$. When the non-linear KPZ term is relevant the exponents change and we get $\zeta \approx 0.63$, $z = 1$ and ν becomes an

independent exponent $\nu \approx 1.733$.

Just above f_c, the interface moves in an intermittent fashion: a point of the interface can stay stuck for a long time and then suddenly acquire a large velocity. The intermittent motion is collective in nature: many pieces are at rest while many connected portions move fast and coherently [50]. Such motion can be probed by starting from a pinned interface and a driving force very close to f_c. By increasing f by the minimal δf that destabilizes the interface, an avalanche occurs: a finite part of size ℓ of the interface advances by a finite amount, spanning an area of size S, while the other parts remain stuck. The avalanche size S is distributed according to:

$$P(S) = f(S/S_m)S^{-\tau} \tag{2.5}$$

with $f(s)$ a scaling function decaying exponentially and S_m that diverges as $f \to f_c$. One finds, for both qEW and qKPZ case, that τ i$\tau = 2-(\zeta+1/\nu)/(d+\zeta)$. Thus, in $d = 1$, $\tau = \tau_{\text{qEW}} \approx 1.11$ for EW and $\tau = \tau_{\text{qKPZ}} \approx 1.26$ for KPZ [46]. The avalanche spatial extension ℓ follows a similar scaling form $P(\ell) = g(\ell/\ell_m)\ell^{-\kappa}$ and, as $S \sim \ell^{d+\zeta}$, one finds $\kappa = 1 + (\tau - 1)(d + \zeta)$. An example of a depinning avalanche is visible in figure 2.1 left. The depinning point is, however, only the second fixed point (after the equilibrium one) relevant for elastic interfaces at $T = 0$. Indeed for very large driving forces $f \gg f_c$, the velocity of the interface becomes linear in f and the interface is in the fast-flow regime. In this regime, the quenched force $F(x, u)$ behaves as thermal noise and the interface dynamics reduces to the one of the conventional EW or KPZ interface and it acquires an effective temperature $T_{\text{eff}} \propto \Delta(0)$. In this regime, the roughness is simply $\zeta_{\text{flow}} = (2-d)/2$. For intermediate forces, between the depinning and fast-flow regimes, the interface has the depinning roughness at small scales and the fast flow one at large ones [16, 50]. In figure 2.1 right the velocity characteristics is summarized.

2.4 . Theory: creep

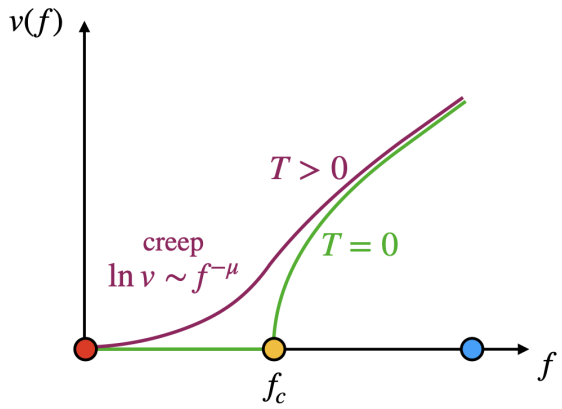

Figure 2.2: Velocity characteristics of the creep regime (violet) compared to the zero temperature one of figure 2.1 right. Above the critical force f_c the effect of temperature tends to diminish and the depinning statistics dominates.

Whenever $T > 0$ and a finite force is applied $f > 0$, the interface always has a finite but small velocity (see figure 2.2 for a summary plot). Indeed the presence of a driving force $f > 0$ generates an energy landscape unbounded from below. However disorder induces the presence of metastable states and energy barriers up to f_c. Thus the interface jumps between metastable states and acquires a finite velocity, described by the celebrated creep law :

$$v \sim v_0 \exp\left(-\left(\frac{f_0}{f}\right)^{\mu}\right) \tag{2.6}$$

with $\mu = 1/4$ the universal creep exponent in $d = 1$ and v_0 and f_0 two material-dependent parameters. The creep law has been first derived in [53], measured in [54] and subsequently confirmed in many experiments [55].

As the interface is an extended object, when f vanishes, the energy barriers diverge and this is ta the origin of the stretched expinential behavior of 2.6. When observed at short times, the interface moves back and forth in an incoherent fashion while for large times one observes large reorganizations [50]. Due to the presence of the driving force, backward motion is suppressed and the interface reorganizes from one local minimum to another, by a sequence of visits through metastable states with lower and lower energies. In order to understand how such reorganizations occur, one can evaluate the typical energy barriers seen by the interface. The first derivations of the creep law, via scaling arguments [56] or FRG [16], employed the hypothesis that during the dynamical evolution between two metastable states

the energy barriers scale as the energy fluctuations of the equilibrium fixed point ($f = 0$) i.e. $E_{\text{barrier}} \sim \ell^{\theta} = \ell^{2\zeta_{\text{eq}}+d-2}$, with numerical simulations supporting this hypothesis [57]. The only assumed effect of the driving force $f > 0$ is only to tilt the energy barriers by

$$E_{\text{tilt}} \sim f\ell^{\zeta_{\text{eq}}+d} \tag{2.7}$$

Thus in the creep regime, a reorganization between two metastable states occurs when the tilt and the barrier energies are of the same order. This happens when the at a scale ℓ_{opt}:

$$\ell_{\text{opt}} \sim f^{-\frac{1}{2-\zeta_{\text{eq}}}} \tag{2.8}$$

with the corresponding energy barrier:

$$E_{\text{barrier}}(\ell_{\text{opt}})\ell_{\text{opt}}^{\theta} \sim f^{-\frac{\theta}{2-\zeta_{\text{eq}}}} \tag{2.9}$$

Using 2.9 we can use an Arrhenius-type activation [50, 58] to estimate that

$$\ln v \propto E_{\text{barrier}} \sim f^{-\frac{\theta}{2-\zeta_{\text{eq}}}} \tag{2.10}$$

which is precisely the creep law 2.6. We immediately identify the creep exponent $\mu = \frac{\theta}{2-\zeta_{\text{eq}}} = \frac{2\zeta_{\text{eq}}+d-2}{2-\zeta_{\text{eq}}}$. Using the $d = 1$ values, we get $\mu = (1/3)/(2 - 2/3) = 1/4$. The physical picture emerging from the scaling argument above is thus the following. The interface moves incoherently back-and-forth below the scale ℓ_{opt} as it fails to overcome the barriers. When a reorganization of bigger scale triggers, the interface finds itself in a new local minimum, leaving room for a new ℓ_{opt} reorganization at a different spatial location. Thus, the interface can be viewed as a collection of pieces of size ℓ_{opt} that reorganize independently and move from one minimum to another with no further correlations. To this scenario, we can associate an energy landscape formed by many uncorrelated energy minima, each corresponding to a separate ℓ_{opt} reorganization.

However, theoretical [16] and numerical studies [17, 50] have suggested another phenomenology completely missed by the simple scaling arguments above. Indeed, they suggest the existence of other, smaller, length scales in play associated to reorganizations that develop for shorter time scales. In this second picture, when a reorganization of size ℓ_{opt} occurs, for a short time, new smaller reorganizations are *facilitated* in nearby regions. This process is strikingly similar to earthquake dynamics where, after a mainshock (corresponding to the ℓ_{opt} reorganization), numerous aftershocks, smaller in magnitude, occur in the neighboring regions. Indeed, a mainshock tends to destabilize the regions surrounding its epicenter, resulting in further earthquakes later in time (the aftershocks). We can refer to each of these reorganizations (both mainshock and aftershocks-like) as *creep avalanches*, and when

we consider them as a single correlated reorganization, we walk about a *cluster*. In parallel to one cluster ℓ_{opt} formation, another one can start to form in a different region, and this novel one is spatially and temporally uncorrelated from the previous one. This second, richer, picture implies a more complex structure of the minima of the energy landscape seen by the interface. Indeed, as a reorganization ℓ_{opt} occurs, the landscape is affected as the barriers are lowered, leaving room for such smaller reorganizations close in space.

Continuing on the second scenario, a remarkable observation of [17] is that the size of clusters S_c presents a statistics akin to the depinning avalanches. Indeed by summing over the contribution from each of creep avalanche $S^{(i)}$ one obtains that the cluster has a size S distributed as

$$P(S) \sim S^{-\tau_{\text{dep}}} \tilde{f}(S/S_c)$$

with $S_c \sim \ell_{\text{opt}}^{d+\zeta_{\text{eq}}}$. This result has huge importance when testing experimentally the predictions of the second scenario. Indeed, one could measure experimentally creep avalanches and aggregate them in clusters. By studying the distribution of such clusters one could understand whether their statistics is compatible with the depinning exponents, as predicted by the second scenario. On the other hand, if the first scenario were relevant, one would observe a scaling of clusters compatible with equilibrium theory. The latter predicts a different τ, i.e. $\tau_{\text{eq}} = 2 - \frac{2}{d+\zeta_{\text{eq}}} \approx 1.39$, which can be viewed as the size of excitations above the ground state of the equilibrium point.

In the next section, we will study clusters to test for the second scenario by conducting data analysis on an experiment of creep motion of a magnetic domain wall in an ultra-thin magnetic film.

2.5 . Experiment: the setting

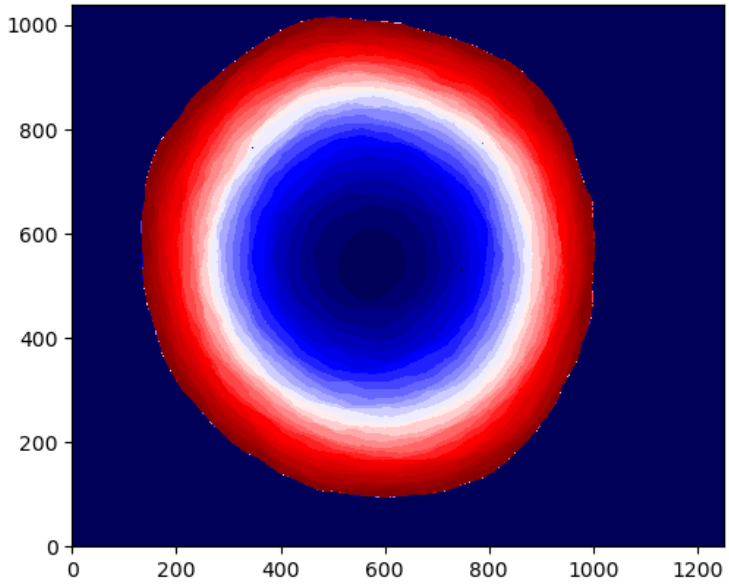

Figure 2.3: Snapshot of the resulting data from the experiment at $H = 0.16$ mT. The color gradient indicates the successive frames.

The creep regime has been observed most effectively in the expansion of a magnetic domain wall in magnetic films and the creep law has been confirmed countless times, starting from the seminal experiment in [54]. In our context, the domain wall expansion is carried out in one ultrathin magnetic film of Ta(5)/CoFeB(1)/MgO(2)/Ta(3) (in the parentheses, the thickness in nanometers). This material exhibits perpendicular magnetic anisotropy (PMA) i.e. when put in a magnetic field, exhibits out-of-plane magnetization. The depinning field of this film is $H_{\text{dep}} \sim 10$mT (equivalent to f_c discussed in the previous section) and presents low density of pinning defects, at variance with other popular magnetic films used in similar experiments [59]. The experiment starts by nucleating an initial bubble of radius ~ 30 μm using a short-field pulse. Four experimental settings are considered, where the subsequent bubble expansion is driven by fields of slightly different magnitude $H = 0.13, 0.14, 0.15, 0.16$ mT. All the fields considered are way below the depinning field and the experiment is carried out at room temperature: we are in the creep regime.

The domain wall expansion is captured using the Magneto-Optical Kerr Effect (MOKE). Images are acquired at a rate of 200 ms with a resolution of 400 nm (which is the pixel size of the acquiring camera). In all four cases the bubble maintains its circular shape all along the expansion. The relative limited resolution and sampling rate does not allow to resolve the dynamics at the nanoscale hence the resulting

images present a coarse grained dynamics. The effect of the change in magnetization of a portion of the wall results in the change in the gray scale level of the acquired image and we need to detect the time at which this change occurs to properly reconstruct the newly activated region, as shown in figure 2.4.

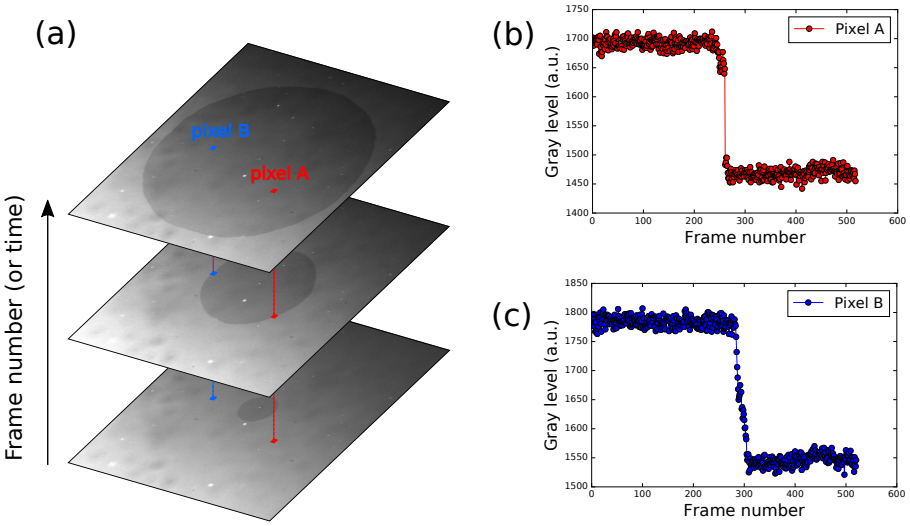

Figure 2.4: **Schematic illustration of the procedure used to determine the position of the domain wall.** (a) All the raw images collected within one measurement of bubble expansion are stacked together into a 3D array. Marked in red and blue are two representative pixels whose gray level profiles are shown in (b) and (c), respectively. While pixel A switches its gray level abruptly, the transition occurs more slowly for pixel B. High/low gray level values correspond to bright/dark MOKE contrast, respectively.

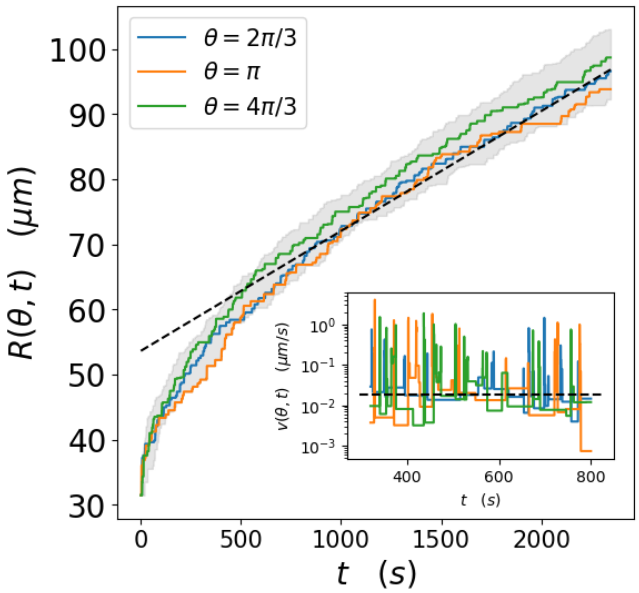

Figure 2.5: Radius of the bubble for the field $H = 0.16$ mT as a function of time. The time in seconds has been converted from the frame index by considering the sampling rate of 200 ms. During the first, non-stationary, regime of the expansion the domain wall is very fast and a lot of activated events occur. Later on, the velocity stabilizes to a stationary creep velocity. It is worth noticing that this change in the regime of creep has been observed in other systems showing a creep behavior, such as ice [60]. The grey area indicates the total velocity span of the points in the wall as a function of the angle θ. The colored curves are relative to three specific angles and the velocity is shown in the inset where the intermittent nature of the dynamics is clearly visible.

Remarkably the set of pixels activated at each sampling is connected in space and we refer to it as a single *frame event*. The coarse dynamics shows two important features:

- The bubble always expands. At scales below ℓ_{opt} the domain wall is expected to move back and forth incoherently, driven by thermal fluctuations. In our experiment we can estimate ℓ_{opt} as:

  $$\ell_{\text{opt}} \sim \ell_C (H_c/H)^{3/4}$$

  as given in [16, 55], with $\ell_C \sim 100$ nm the Larkin length and $H_c \sim 10$ mT the depinning field. Using $H \sim 0.13, 0.14, 0.15, 0.16$ we get ℓ_{opt} goes from ~ 380 to ~ 400 nm. This means that ℓ_{opt} is smaller or at most at the order the pixel resolution of 400 nm, hence we cannot observe the backward motion, and we only record the forward one above ℓ_{opt}. This is quantitatively visible by inspecting the radius of the domain wall as a function of time, as shown in figure 2.5.

- The wall motion presents spatial correlation well above the pixel size. As figure 2.6 depicts, each frame event corresponds to a compact spatial reorganization and events of subsequent frames tend to cluster together, as predicted by the second scenario in the previous section.

These two features support the second scenario for which an initial reorganization of size ℓ_{opt} initializes a cascade of events on a much larger scale. At this level this observation is more qualitative. In the next section, by directly analyzing the domain wall structure, we will unveil the precise form of correlations supporting the second scenario.

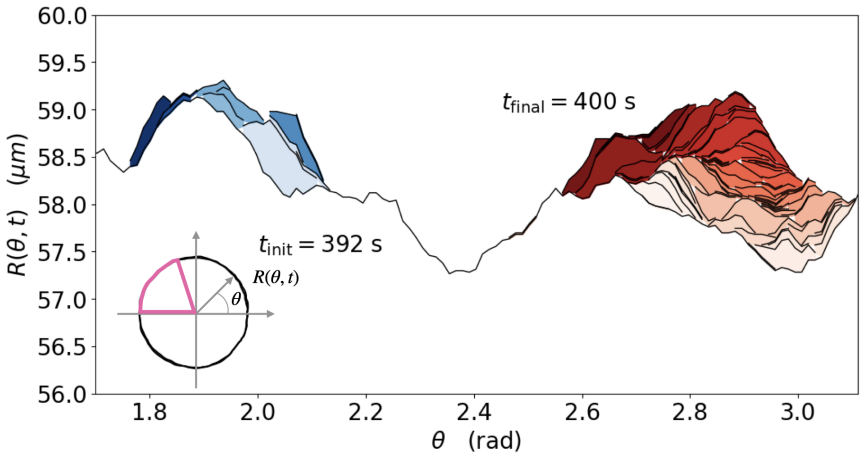

Figure 2.6: Example of two formation of clusters between a time $t = 392$ s and $t = 400$ s. The blue and the red gradients indicate two different forming clusters. The darker the color the later the frame event occurs.

2.6 . Experiment: data analysis

Theoretical results [16] and numerical simulations [17, 50] suggest that events following a reorganization of scale L_{opt} generate a cascade of correlated events, akin to mainshock-aftershocks in seismicity. In numerical simulations [17, 50], it has been shown that, by aggregating such correlated events into clusters, their statistics is compatible with the statistics of avalanches at depinning, which are in nature a zero-temperature process. In this case, as one has full control over the dynamics of single activated events following ℓ_{opt}, so it is immediate to identify to which cluster an event belongs. On the other hand, in an experimental setting, the limited acquisition rate and resolution affect the spatial and temporal mixing of the observed events, hence one needs to apply extra-care in the cluster identification. To this purpose, we now discuss an algorithm to construct such clusters.

We index each frame event in the collected data is indexed by a frame index t. Each event contains S_t pixels and we label such pixels as $\{x_i(t), y_i(t)\}_{i=1}^{S_t}$. We then define the spatial distance between two frame events as:

$$d_{t,t'} = \min_{i=1\ldots S_t, j=1\ldots S_{t'}} |x_i(t) - x_j(t')| + |y_i(t) - y_j(t')| \tag{2.11}$$

Using $d_{t,t'}$, we can build up an algorithm that creates clusters of creep avalanches based on constructing a network of frame events. Consider an adjacency matrix $A_{t,t'}$ where the nodes are the frame events. Given a frame event t, consider all frame events $t' = t+1, \ldots, t+T^*$ and set $A_{t,t'} = 1$ if $d_{t,t'} \leq d^*$. By repeating this procedure for each time frame t, we end up with an adjacency matrix $A_{t,t'}$ that connects only frames close in space and time. Here d^* and T^* are two parameters of the algorithm. We set d^* equal to 2 as we want to connect frame events that are contiguous in space. Increasing it to 3 or 4 does not affect the results. For T^* we did a more refined research and we explored between $T^{=}6$ and $T^* = 16$ frames, without observing any drastic change in the algorithm's results.

The clusters are defined as the connected components of the graph associated to $A_{t,t'}$. The size of a cluster S is given by the total number of pixels in the cluster We can visualize how frame events appear by direct inspection in figure 2.7 left. Single frame events and the clusters they form show an ellipsoidal shape with an area precisely equal to S. This observation allows us to set up a procedure that lets us extract the elongation of clusters ℓ.

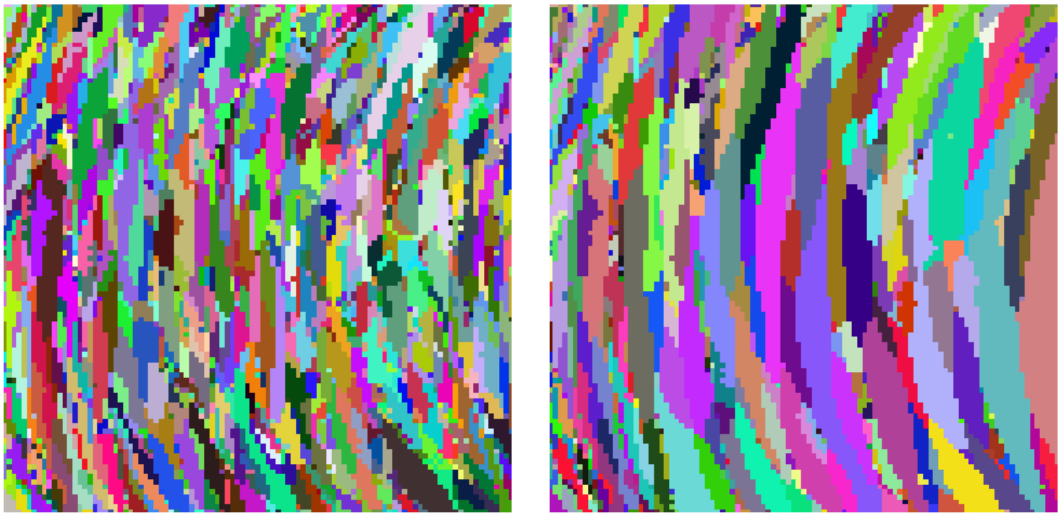

Figure 2.7: Raw event frames (left) and the obtained clusters (right). The elongated nature of the clusters is immediately visible and suggests a roughness for the domain wall interface smaller than 1.

Indeed, calling the coordinates of pixels in a cluster $\{x_i, y_i\}$, we can construct the 2×2 covariance matrix C between the pixels:

$$C = \begin{bmatrix} \overline{x^2} - \overline{x}^2 & \overline{xy} - \overline{x}\,\overline{y} \\ \overline{xy} - \overline{x}\,\overline{y} & \overline{y^2} - \overline{y}^2 \end{bmatrix} \tag{2.12}$$

where the overline stands for the average among the pixels of the cluster. If we diagonalize C, we find two eigenvalues λ_+ and λ_- which are an estimate of, respectively, the major and minor axis of the ellipse describe by the cluster. Because of this, we can relate λ_+ and λ_- to S as $S = \pi\lambda_+\lambda_- a^2$ with a some constant. We find a by regressing S with the found λ_+ and λ_- and thus we identify ℓ with $a\lambda_+$. In figure 2.7 right we show an example of the obtained clusters.

2.7 . Experiment: results

Figures 2.8 left and middle show the results of our analysis. Both figures show statistics for S and ℓ compatible with a depinning behavior, excluding the equilibrium fixed point supported by the first scenario. Thus it is tempting to interpret these clusters as avalanches at the depinning transition, as suggested by the numerical simulations in [17]. In those simulations, however, avalanches are very fat in the growth direction (i.e., the direction of propagation of the interface) consistently with the qEW depinning. Here, clusters are instead elongated objects, as visible from the scaling $S \sim \ell^{d+\zeta}$ in figure 2.8 right, resulting in a roughness exponent $\zeta \sim 0.63$. This exponent excludes the possibility of qEW depinning but is consistent with the qKPZ depinning. We corroborate this result with an independent measure of the roughness by directly reconstructing the interface profile. As the interface is circular in shape, we obtain a collection of radii as a function of the angle, $R(\theta, t)$. We can then compute the structure factor of the interface $S(q, t) = |\rho(q, t)|^2$ where $\rho(q, t)$ is the discrete Fourier transform of $R(\theta, t) - R(t)$ w.r.t. θ (here $R(t)$ is the average of the radius). For small q we expect the scaling $S_q \sim 1/q^{1+2\zeta}$. The results for S_q are visible in figure 2.9. The measured ζ is both compatible with equilibrium $\zeta = 2/3$ and KPZ depinning $\zeta \approx 0.63$, again leaving out qEW depinning. In conjunction with the results from the clusters, this leaves out qKPZ depinning as the only fixed point describing the clusters statistics.

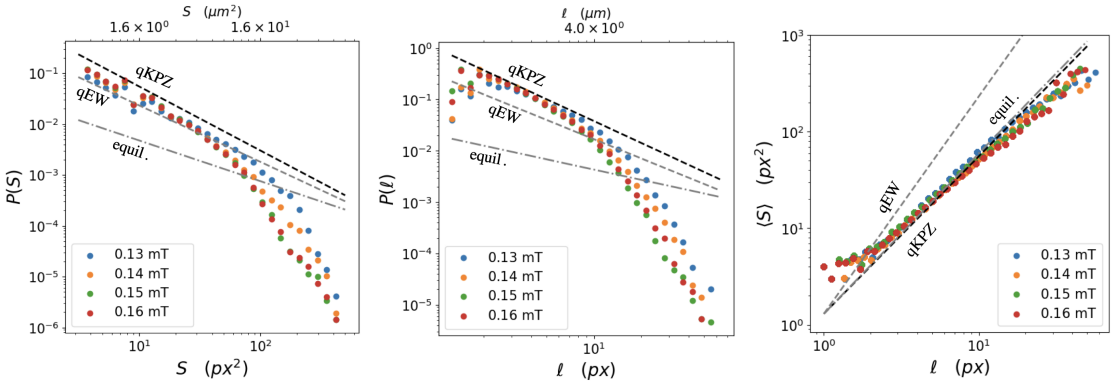

Figure 2.8: (a) Cluster size S and (b) longitudinal length ℓ distributions for different magnetic fields. (c) Cluster size versus their longitudinal length. The clusters have been obtained for $T^* = 8$ frames and $d^* = 2$ pixels. The first two panels are compatible with qEW and qKPZ universality classes but not with the equilibrium exponents. The value of the roughness exponents from (c) is computed using the power law scaling $S \sim \ell^{1+\zeta}$. The measured value is compatible with both $\zeta_{\text{qKPZ}} = 0.63$ and $\zeta_{\text{equilibrium}} = 2/3$, but exclude the qEW universality class $\zeta_{\text{qEW}} = 1.25$. Combining these findings leaves the qKPZ universality class as the sole possible candidate for describing the creep motion in our experiment.

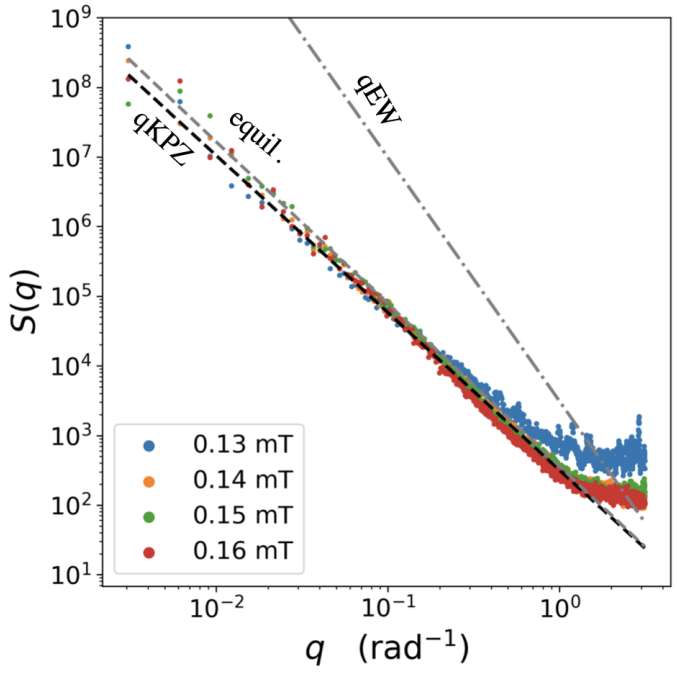

Figure 2.9: Structure factor $S(q)$ computed by averaging over time the Fourier transform $\rho(q,t)$ of $\rho(\theta,t) = R(\theta,t) - \overline{R}(t)$, i.e., $S(q) = \langle \rho(q,t)\rho(-q,t)\rangle_t$. Using the power law scaling an $S(q) \sim q^{-(1+2\zeta)}$ at small q, we compute a value of the roughness exponent in perfect agreement with the one obtained in Fig. 2.8 (c).

2.8 . Conclusion and future work

The celebrated creep formula (2.6) rests on the hypothesis that the key feature determining a wall motion is optimal excitations of size ℓ_{opt}. Our analysis on intermittently occurring rapid movements along a magnetic wall unveils their spatial organization, extending on scales much more extensive than ℓ_{opt}. Their size and shape display the same statistics of the avalanches recorded at the depinning but with a much slower evolution. In contrast with previous theoretical and experimental studies [50, 61], our experiment shows that the exponents are compatible with the qKPZ instead of the qEW universality class. The emergence of KPZ dynamics at depinning must be sustained by anisotropy in the material [43], thus requiring future study on similar systems for future understanding.

The scenario emerging from our results suggests that events of size ℓ_{opt} lower the energy barriers accessible by the system, giving rise to a cascade of correlated events. In the future, this opens up the possibility of testing this scenario in other examples of elastic disordered systems such as ferroelectric domain walls [62–64] or crack propagation [65]. Interestingly, similar observations were recently reported for different disordered systems, such as amorphous solids and glass-forming liquids. Simulations on elastoplastic models have shown how localized plastic excitations can trigger cascades of faster events [66,67]. In that case, such avalanches were described as thermally-facilitated avalanches and they are generated by the same mechanism as clusters of creep avalanches. If this scenario were confirmed, it would be clear that the complex nature of disordered energy landscapes cannot be described simply by a sequence of uncorrelated elementary excitations.

On top of deepening the understanding of the effects of elasticity and temperature in disordered systems, the results reported here can also have significant influence in the field of spintronics. The analysis of the creep dynamics of a domain wall is the starting point for the determination of interfacial Dzyaloshinskii-Moriya interaction (DMI). This is a chiral interaction responsible for the occurrence of topological spin structures, such as chiral domain walls and skyrmions. The latter are considered the most promising information carriers in future spintronics technologies [68]. The determination of the DMI constant is based on the asymmetric expansion of the bubble under an in-plane magnetic field, with the domain wall velocity measured by dividing the displacement between two MOKE snapshots over their time interval. Fig. 2.5 actually suggests that the velocity is constant only at large times/displacements, and thus that this procedure could be misleading. In addition, theoretical expressions to evaluate the DMI field from the velocity curve are primarily phenomenological, and a more accurate description of the domain wall

dynamics, such as the qKPZ reported here, could highly improve the fits of the data. We hope these considerations shed some light on a more accurate determination of DMI value and solve the contradictions with other popular methods, such as the Brillouin light scattering.

Chapter 3

Aftershocks and GPS data

In this chapter we focus on the study of data coming from real earthquakes. Specifically we present a *proof of concept* and a first implementation of a system to forecast aftershocks originating from large earthquakes. We focus on earthquakes from Japan but this method is seamlessly extensible to any region in the world. This new approach focuses on two types of seismic data:

- Catalog data, which for our purposes gives us the time, location (latitude, longitude) and magnitude of earthquakes happened in some region

- Global Positioning System (GPS) data, which measures for the three spatial direction north, east and up the deformation of Earth's surface due to both background continental drift and earthquake occurrence.

Earthquakes from catalog data come from the inversion of P and S seismic waves picked up by seismic stations. The data we are gonna use in this context comes from the Japan Meteorological Agency (JMA) and can be accessed from here. It suffices to know that we are gonna use four main pieces of information (*features*) of a seismic catalog, namely the time of occurrence t, the epicenter's longitude and latitude (x, y) and magnitude m. On the other hand, GPS data are less known, especially in the statistical physics and deep learning community, henceforth it is worth spending some time discussing about it.

3.1 . GPS data

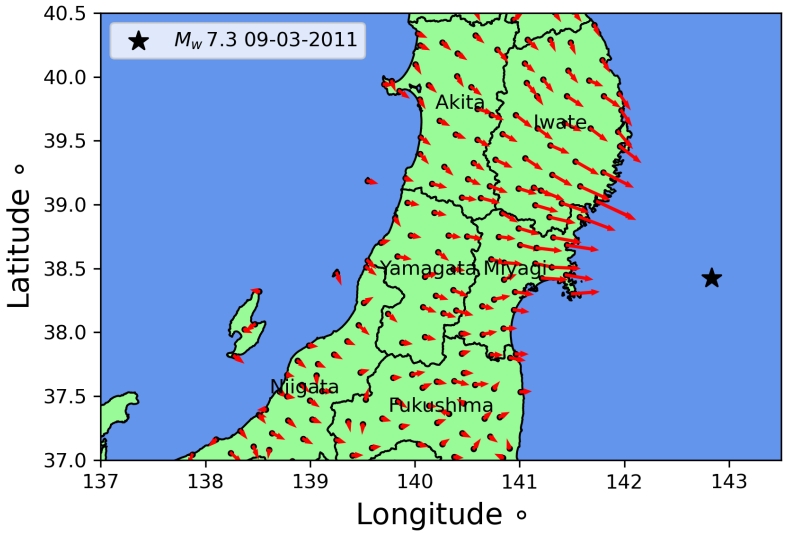

Figure 3.1: Ground deformation (red arrows) due to the magnitude 7.3 earthquake occurred in offshore Japan (black star) the 9th March 2011. It is evident how the deformation direction and magnitude is strongly correlated with the location of the earthquake. GPS data extracted from the Nevada Geodetic Laboratory repository.

In the context of geophysics, GPS data refer to measurements of ground deformation due to both the slow and continuous continental drift and the sudden deformation caused by large earthquakes. To understand the latter type, which is the most interesting to study seismic phenomena, we can look at the map of Japan GPS stations the 9 march 2011. In that date the first earthquake (of magnitude 7.3) belonging to the Tōhoku seismic sequence occurred. This is the first event triggering the tsunami that caused the Fukushima nuclear disaster. In figure 3.1 we show the measured effect of this earthquake on the ground deformation. Moreover, as shown in figure 3.2, if we compare the total displacement as a function of the distance from the earthquake epicenter, we obtain a curve which rapidly falls off as we consider stations distant from the epicenter to then saturate to an approximately constant value, which can be seen as a mixture of measurement noise and the effect of continental drift.

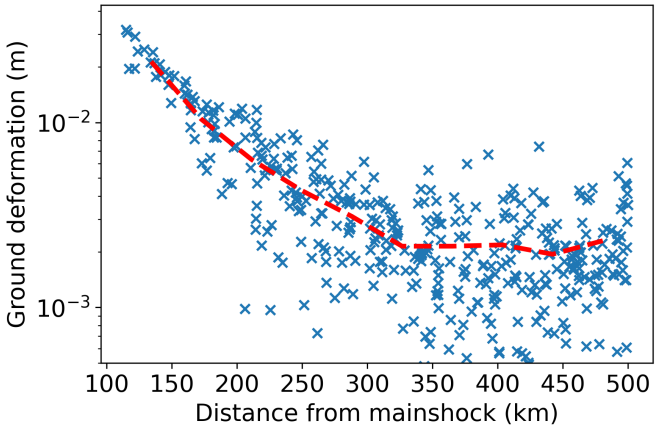

Figure 3.2: Ground deformation vs distance from the mainshock. The crosses represent single measurement while the red dashed line the average behaviour. As the earthquake occurred offshore, no measurement is available close to the epicenter. GPS data extracted from the Nevada Geodetic Laboratory repository.

These two connected results can be reproduced for any other large earthquake, provided close enough station measurements are available. The importance of the GPS data is thus evident, as it provides informations on the effect of an earthquake which cannot be easily extracted from waveform data. The deformation at the day of the earthquake is particularly important as it can tell us which regions have been more destabilized and thus are a potential recipients for aftershocks occurrence, which can often be as dangerous as a main shock. With in mind the forecasting, many works - both using a mixture of classical statistics methods and geophysical considerations [69–74] or machine learning [18] - started to employ underground displacements maps (slip maps) to predict the locations of aftershocks. However this is a remarkably hard task, as it requires, on top of waveform and GPS data, a knowledge of both the fault geometry and a model for how the rupture occurs. On the other hand, GPS data can be employed out-of-the-box and, especially in the cases of shallow earthquakes, can be enough to provide enough information to attempt the forecasting of aftershocks. This possibility is analyzed in the next section, where we lay out a (possible) way to deal with GPS ground deformation data that is suitable for this task.

3.2 . Surface deformation maps

The main technical issue with GPS measurements is that the resulting surface deformation is inherently available only in discrete space points. To handle such data structure, one could either directly use the network structure of GPS stations

with the associated measurements an "input data" for the forecasting or interpolate the measurements to obtain a continuum deformation field. The direct use of measurements has been seldom considered in literature [75, 76] as the network structure is harder to handle. In the future, with the current improvement of graph and networks oriented machine learning tools, such as Graph Neural Networks, and with the increase n the quantity and quality of GPS data, such an approach could emerge again. On the other hand, an interpolation-driven approach has a much broader history - in the past for statistical analysis [77–79] and recently in more prediction-oriented tasks [80]. In this section, we present one of the possible ways to elaborate the networked data to produce a continuum displacement field. We start by making an initial reasonable approximation, as done by previous literature [79]: we assume that the earth's surface can be treated as a thin homogeneous elastic sheet, and consequently we can employ the elastostatics equations to describe the measured displacements. We thus discard from the GPS data the deformation measurements in the upward direction, which have nonetheless larger measurement errors. In this setting, electrostatics equations [81] tell us how the displacement of the ground is related to N applied point-like forces $(f_{i,e}, f_{i,n})$ at locations (x_i, y_i) for $i = 1 \dots N$ (here the subscripts e and n refer to the eastward and northward directions, x's are longitudes and y's latitudes):

$$\begin{aligned} \frac{2}{1-\nu}\partial_x^2 v_e + \frac{2\nu}{1-\nu}\partial_{xy}^2 v_n + \partial_y^2 v_e + \partial_{xy}^2 v_n &= -\tfrac{1}{\mu}\textstyle\sum_{i=1}^{N} f_{i,e}\delta(x-x_i)\delta(y-y_i) \\ \partial_{xy}^2 v_e + \partial_x^2 v_n + \frac{2\nu}{1-\nu}\partial_{xy}^2 v_e + \frac{2}{1-\nu}\partial_y^2 v_n &= -\tfrac{1}{\mu}\textstyle\sum_{i=1}^{N} f_{i,n}\delta(x-x_i)\delta(y-y_i) \end{aligned} \quad (3.1)$$

Here we adopted the form of elastostatics with the Poisson ratio and the bulk modulus as constants [82]. We can absorb the bulk modulus into the definition of the forces (and thus we set it to 1) and we use $\nu = 0.5$, the typical choice for incompressible elastic materials [79]. Starting from 3.1, we proceed as follows. At a given instant, we have measurements of the deformation (v_e, v_n) at station locations (x_i, y_i). These measurements can be used to find the applied forces $(f_{i,e}, f_{i,n})$ at the same locations by inverting the elastostatics equations (3.1). This can be done in Fourier space with space-frequency (k_e, k_n):

$$\begin{bmatrix} \frac{2}{1-\nu}k_e^2 + k_y^2 & \frac{1+\nu}{1-\nu}k_e k_n \\ \frac{1+\nu}{1-\nu}k_e k_n & \frac{2}{1-\nu}k_n^2 + k_e^2 \end{bmatrix} \begin{bmatrix} \tilde{v}_e(k) \\ \tilde{v}_n(k) \end{bmatrix} = \frac{1}{4\pi^2\mu}\sum_i \begin{bmatrix} f_{i,e} \\ f_{i,n} \end{bmatrix} e^{-ik_e x_i - ik_n y_i} \quad (3.2)$$

The inverse of (3.2) reads:

$$\begin{bmatrix} \tilde{v}_e(k) \\ \tilde{v}_n(k) \end{bmatrix} = \sum_i \frac{1}{8\pi^2\mu k^4} \begin{bmatrix} 2k^2 - (1+\nu)k_e^2 & -(1+\nu)k_e k_n \\ -(1+\nu)k_e k_n & 2k^2 - (1+\nu)k_n^2 \end{bmatrix} \begin{bmatrix} f_{i,e} \\ f_{i,n} \end{bmatrix} e^{-ik_e x_i - ik_n y_i} \quad (3.3)$$

with $k^2 = k_e^2 + k_n^2$. By inverting the Fourier transforms [79], we can write:

$$\begin{aligned} v_e(x,y) &= \sum_i q(x-x_i, y-y_i) f_{i,e} + w(x-x_i, y-y_i) f_{i,n} \\ v_n(x,y) &= \sum_i w(x-x_i, y-y_i) f_{i,e} + p(x-x_i, y-y_i) f_{i,n} \end{aligned} \tag{3.4}$$

where the function $q(x,y)$, $p(x,y)$ an $w(x,y)$ are:

$$\begin{aligned} q(x,y) &= (3-\nu)\ln r + (1+\nu)\tfrac{y^2}{r^2} \\ p(x,y) &= (3-\nu)\ln r + (1+\nu)\tfrac{x^2}{r^2} \\ w(x,y) &= -(1+\nu)\tfrac{xy}{r^2} \end{aligned} \tag{3.5}$$

where $r = \sqrt{x^2+y^2}$. The next step is to discretize space in the two directions (x,y) in cells of lateral size a. As we want to interpolate signals from GPS stations, a should be chosen to be smaller than the typical distance between neighbouring stations, in order to avoid having more than one station inside single cell. At present we are gonna choose $a = 5$ kilometers, based on the typical spatial speration between japanese GPS stations (for other regions where the station density is lower one has to choose larger a, such as California, where a good a is of the order of ~ 10 km [79]). A final remark is needed before continuing: equations (3.5) are singular when $r = 0$ hence we need to introduce a small regularization term to r i.e.$r \to r + \epsilon$ where ϵ should be on the order of a. We are now ready to find the forces $(f_{i,e}, f_{j,e})$. Indeed by using the known deformation measurements at each point (x_i, y_i), we can write the linear equation that relate them to the forces:

$$\begin{aligned} v_e(x_i,y_i) = v_{i,e} &= \sum_j q(x_i-x_j, y_i-y_j) f_{j,e} + w(x_i-x_j, y_i-y_j) f_{j,n} \\ v_n(x_i,y_i) = v_{i,n} &= \sum_i w(x_i-x_j, y_i-y_j) f_{j,e} + p(x_i-x_j, y_i-y_j) f_{j,n} \end{aligned} \tag{3.6}$$

We rewrite (3.4) using a matrix $G_{ij}^{\alpha,\beta}$:

$$v_{i,\alpha} = \sum_\beta \sum_i G_{ij}^{\alpha\beta} f_{j,\beta} \tag{3.7}$$

with $\alpha = e, n$ and $\beta = e, n$ are the component indices. So numerically we can invert (3.7) and find the forces $(f_{i,e}, f_{i,n})$ and use equations (3.4) to find the displacement in any other location (x,y) different from the station ones (x_i, y_i). In practice the inversion is made by using the SVD decomposition and by discarding some of the singular values, which results in the smoothing of the solution [79]. This method

and analog ones have been tested in numerous works with much success. However, one has to keep in mind that for regions of the space where the density of station is low (for example when one considers coastal regions as no station is present in the sea) or even no station is present, the results of the interpolation do not reflect the underlying physical displacement. As such, we will exclude from our analysis regions where interpolation quality is low. Calling $d_{\min}(x, y)$ the distance of a cell (x, y) from its closest station, our proposal is not to use (mask) all the cells (x, y) for which $d_{\min}(x, y) > d^*$. In this work, we will employ $d^* \approx 90$ km. To show the type of output from such an interpolation method, we show in figure 3.3 the interpolated surface deformation maps from Japan on the date 9th March 2011.

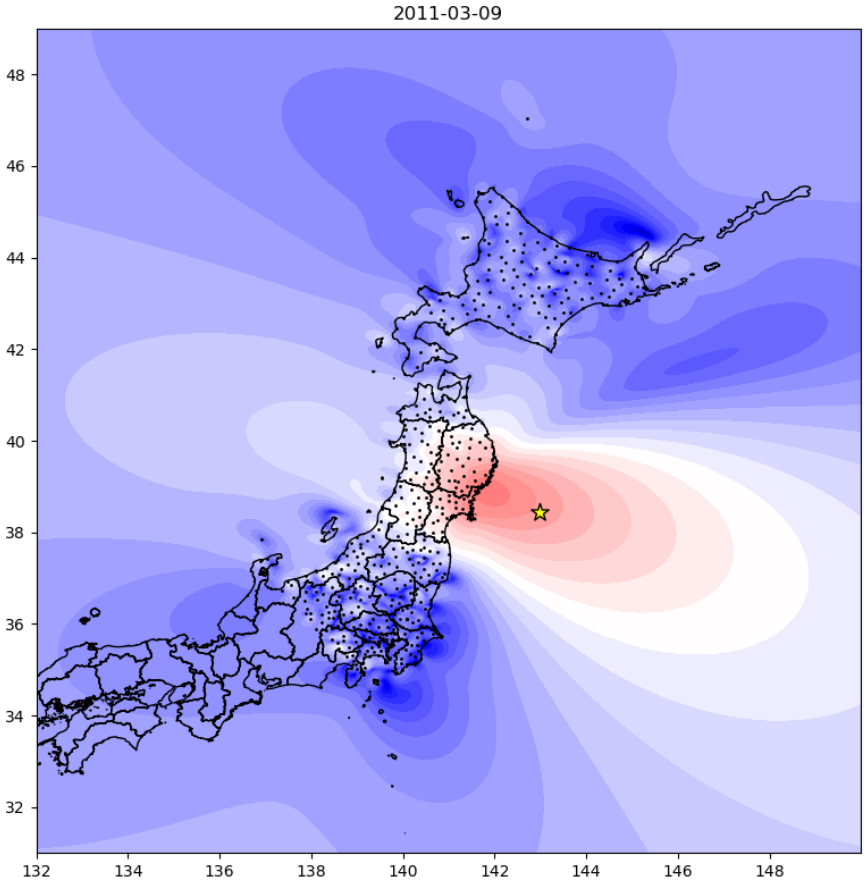

Figure 3.3: Logarithm of the magnitude (in meters) of the interpolated displacement as measured at the date 9th March 2011 in Japan. The black dots correspond to actual station positions.

Moreover, we can visualize the change in displacement by focusing on the days following the 9th of March.

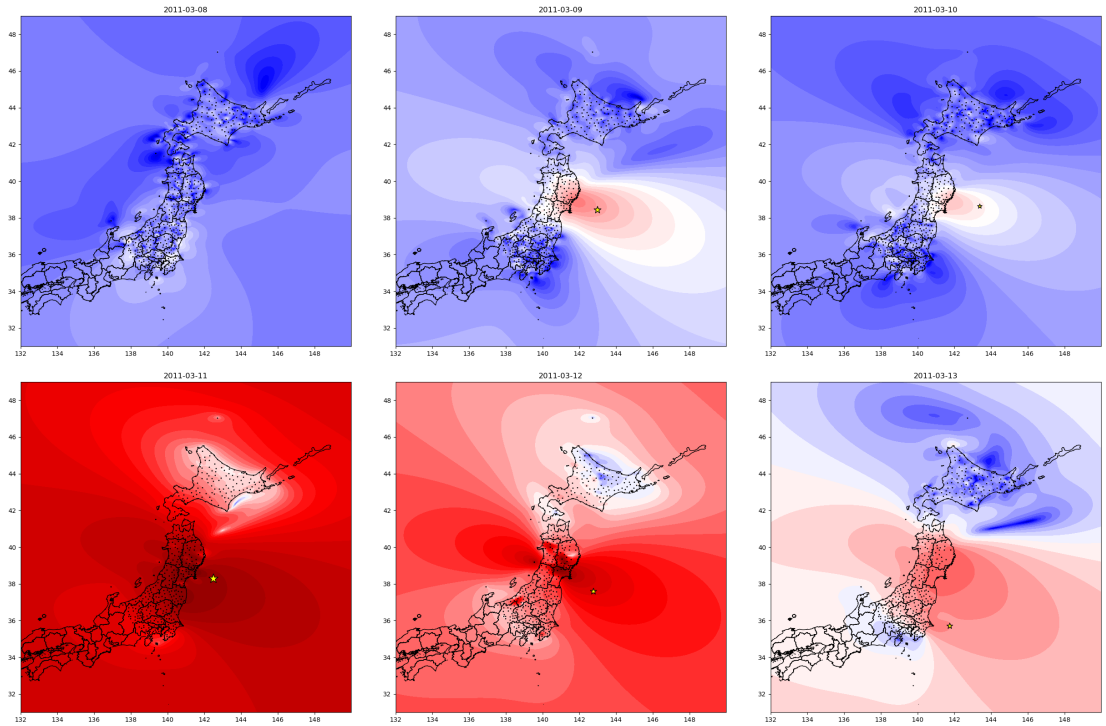

Figure 3.4: Interpolated displacement maps from the 8th of March to the 13th of March 2011 in Japan. Dark red corresponds to displacements of the order of centimeters, while blue to a few millimeters. The first map on the second row corresponds to the Magnitude 9.1 Tohoku earthquake, which indeed shows the largest possible displacement.

3.3 . Constructing input and output

Any forecasting pipeline has to be divided into two steps: choosing the input for the forecasting and the corresponding output. First of all, we need to identify seismic *sequences*, namely couples of mainshock-aftershocks. There exists a plethora of method to identify them. One can use the so called stochastic declustering [83], which uses a non-deterministic method to identify mainshock-aftershocks pair. However as the output of such an approach is, indeed, stochastic, is less suited for simple forecasting. Instead, for the sake of simplicity, we consider as mainshocks all earthquake with at least magnitude 6 occurring in Japan from the year 2000 to 2019 (the seismic catalog of this period is properly constructed; earthquakes occurring after 2019 as of now are still being analyzed). Our source is the Japanese Meteorological Agency, which releases bulletins with earthquakes occurring in the Japanese area. On the other hand as aftershocks, we pick up all earthquakes occurring after a mainshock in a radius of 300 km from the mainshock's epicenter and within a time window of 45 days. What can occur, in such a manual earthquakes selection,

is that two or more mainshocks have overlapping aftershocks or even that one identified mainshock is, in fact, a foreshock (as for Fukushima discussed in the previous section where one finds an earthquake of magnitude ~ 7 the 9th of March 2011 and one of magnitude ~ 9 on March the 11th). It is worth knowing that this ambiguity is well known in sequence selection, as there is no unique definition of a mainshock. We employ the simplest solution i.e. we identify mainshocks with such problems and we pick the largest one as a mainshock.

Having selected the mainshock-aftershocks pairs, we indicate with t_0 the day of the mainshock. Then we consider GPS data interpolated from the day $t_0 - 1$ to the day $t_0 + 1$ and, as such, we only keep the aftershocks occurring at times later than $t_0 + 1$. Since we are using daily GPS data, one has to include the day $t_0 + 1$ as the displacement due to the mainshock might be delayed w.r.t. day t_0. While we lose some aftershocks this way, we are sure we are not mixing information from overlapping time windows. For each mainshock occurring at some time t_0, the interpolation is carried out using displacement measurements of stations in a radius of 300 km centered at the epicenter (x_0, y_0), considering a spatial window of 250km $\times$ 250km. As for the output, namely the aftershocks, we use an *image segmentation* approach. We identify and discretize in cells of size $a = 5$ km the locations of aftershocks from a given mainshock and we construct a map $A(x, y)$ that equals to 1 if an aftershock occurred inside the cell (x, y) and is zero otherwise. This approach is the simplest one and is inspired by [18]. Other approaches, such as a magnitude-dependent prediction, are theoretically possible and are left for future work.

3.4 . Training models

Having defined the input $(v_e(x, y), v_n(x, y))$ and the output $A(x, y)$, we are ready to set up a forecasting protocol. We can do two types of forecasting. One, which acts as a form of baseline, is a pixel-to-pixel prediction, which consists into predicting $A(x, y)$ by only knowing $(v_e(x, y), v_n(x, y))$ at one cell location. The other is an image-to-image prediction that uses the whole image (v_e, v_n) to predict A.

For the first type, we are gonna employ the logistic regression. As input we are gonna use the displacement magnitude $v_r(x, y) = \sqrt{v_e(x, y)^2 + v_n(x, y)^2}$ at cell (x, y). The output of the model is given by the probability that the cell (x, y) has any aftershocks:

$$\pi(x, y) = \sigma(\alpha v_r(x, y) + \beta) \tag{3.8}$$

where $\sigma(z) = 1/(1 + e^{-z})$ is the logistic function and α and β are two fittable (learnable) parameters. In order to find α and β we need to minimize the following

loss function:

$$-\sum_{n=1}^{N_{\text{tr}}} \sum_{(x_n,y_n)} A(x_n,y_n) \ln \pi(x_n,y) + (1 - A(x_n,y_n)) \ln(1 - \pi(x_n,y_n)) \tag{3.9}$$

Such loss function is referred to *cross-entropy loss*. The sum over n refers to the number of training samples N_{tr} while the sum over (x_n, y_n) is over the pixels of the $n-$ th training sample. As mentioned before, each pixel in the interpolation as a different *quality*, namely cell too far away from stations are less trustable. We introduce the quality of the cell by adding a weight to the loss:

$$-\sum_{n=1}^{N_{\text{tr}}} \sum_{(x_n,y_n)} \gamma(x_n,y_n) \left[A(x_n,y_n) \ln \pi(x_n,y) + (1 - A(x_n,y_n)) \ln(1 - \pi(x_n,y_n))\right] \tag{3.10}$$

where $\gamma(x,y) = \exp\left(-\frac{d^2_{\text{min}}(x,y)}{2\sigma_q^2}\right)$ and $\sigma_q = 8a$. This way we give more importance to pixels close to stations and we try to maximize the performance there. Finally the number of positive samples, namely the number of cells with $A(x,y) = 1$, is way smaller than negative cells (with $A(x,y) = 0$). In the dataset used the negative cells comprise the $\approx 98\%$ of the whole cells. In order to compensate for this we reweight the loss as following:

$$-\sum_{n=1}^{N_{\text{tr}}} \sum_{(x_n,y_n)} \gamma(x_n,y_n) \left[w_1 A(x_n,y_n) \ln \pi(x_n,y) + (1 - w_1)(1 - A(x_n,y_n)) \ln(1 - \pi(x_n,y_n))\right] \tag{3.11}$$

where $w_1 \approx 0.98$ reflects the abundance of negative cells. This way we give more importance to positive cells, as they are the minority.

This is for the single cell prediction. For the image-to-image one we need to use a model that can accept as input a whole image. The best candidate for this is a Convolutional Neural Network (CNN). A CNN is a type of neural network particularly suited for Computer Vision tasks and at its heart, as the name says, there is a convolution operation. In this context a convolution operation takes as input an image of size $H \times W$ pixels composed of C channels. For example, in a regular picture, the channels would correspond to the red (R), green (G), and blue (B) color components (hence $C = 3$). The output of the convolution is a new image of size $H' \times W'$ and C' channels. The convolution operation maps the input to the output by applying the convolution operator $\star$ to the input:

$$I_{\text{out,c}'} = b_{c'} + \sum_{c=1}^{C} I_{\text{in,c}} \star w_{c'} \quad c' = 1 \dots C' \tag{3.12}$$

Here $I_{\text{in,c}}$ is the input image with c being the channel index and $I_{\text{out,c}'}$ is the corresponding output. Here $w_{c'}$ represents the *filter* (also called *kernel*) of the convolution, which is a $k_1 \times k_2$ matrix. In practice, the convolution operator works as following:

$$(I \star w)(x, y) = \sum_{m=0}^{k_1-1} \sum_{n=0}^{k_2-1} I(x+m, y+n) w(m, n) \tag{3.13}$$

Finally $b_{c'}$ is called *bias* term and is an (optional) constant that is added to the output of the convolution. Other ingredients can be added to a convolution operation that we do not discuss here as they won't influence the overall discussion. Ultimately the scope of the convolution is, by properly choosing the filters, to extract spatial information from the input image. As a practical example a 3×3 filter with $w(m, n) = 1/9$ for any m, n corresponds to averaging the image in windows of 3×3 pixels. The simplest CNN is constructed by stacking together multiple convolution operations that, step-by-step, aim to extract specific *features* from the image. However a simple chaining of convolutions remains a linear operation and to make the output of the network richer (and thus able to extract more complex features), one should also apply non-linear functions to the pixels of each convolutional output. A popular choice is the ReLU function $f(z) = \max(z, 0)$. The ReLU enhances the output of the convolution by throwing out the negative pixels and boosting the positive ones. Other linear function are used after a convolution. In our case we will also employ the sigmoid $f(z) = 1/(1 + e^{-z})$, which maps real values to the finite interval $[0, 1]$. Hence the convolution operation and the non-linear function constitute the building blocks of our CNN. These two are by no means exhaustive and we refer to the original literature for more ingredients [...]. The choice of the number of channels and filter sizes in each convolution operation fixes the structure of the network. The filters and the biases are the network's parameters and they are fixed by minimizing a loss function. We are now ready to go back to the CNN for aftershocks forecasting. For the CNN in this study we use a *two-column* CNN. In practice we construct two separate networks, the first one taking as input the magnitude of the displacement:

$$v_r(x, y) = \sqrt{v_e(x, y)^2 + v_n(x, y)^2} \tag{3.14}$$

while the second one two angular features, namely:

$$\cos\theta(x, y) = \tfrac{v_e(x,y)}{v_r(x,y)} \tag{3.15}$$

$$\sin\theta(x, y) = \tfrac{v_n(x,y)}{v_r(x,y)} \tag{3.16}$$

$$\tag{3.17}$$

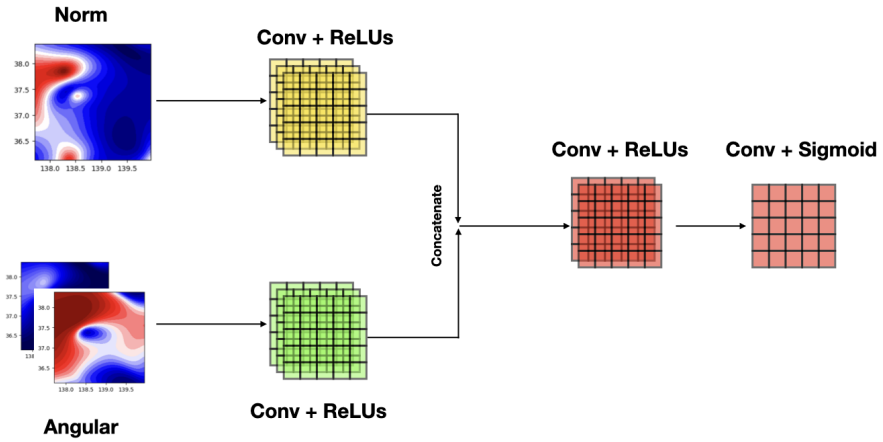

Figure 3.5: Schematic summary of the CNN architecture. The norm of the displacement and the angular parts are fed into two separate sequences of convolutions. The two outputs are concatenated along the channels and fed to a final sequence of CNNs that outputs a probability of aftershock occurrence.

Hence the first network has 1 channel as input, the second has 2 channels. The two networks are structurally the same, they each contain 3 convolutional steps with 10 channels and kernels of size 5×5 per convolution. Between each convolution, we apply a ReLU non-linear function. The two outputs are concatenated along the channels, thus we obtain from two images of 10 channel each one image of 20 channels. To such output we then apply a new series of convolution of, respectively, 20, 5 and 1 channels in output. After the first two we use a ReLU and for the last one a sigmoid, as we want to map the real values of the pixels into probabilities. A schematic summary of the CNN structure is given in figure 3.5.

Both in the Logistic or the CNN approach, the output for a mainshock i the probability $\pi_i(x, y)$ that an aftershock occurs at location (x, y). To assess the quality of the prediction we need to count how many cells are correctly predicted. As we deal with a probability, we need to introduce a threshold π_{th} on the $\pi_i(x, y)$ that determines if a cell is predicted as having an aftershock (is a *positive* cell) or not (is a *negative* cell):

$$(x, y) \text{ is predicted to have an aftershock if } \pi_i(x, y) > \pi_{\text{th}} \tag{3.18}$$

At given fixed threshold, we can properly count the correctly classified cells by analyzing two quantities:

- The True Positive Rate (TPR), namely the fraction of cells (x, y) that have an aftershock ($A_i(x, y) = 1$) and for which the aftershock is correctly predicted ($\pi_i(x, y) > \pi_{\text{th}}$).

- The False Positive Rate (FPR), namely the fraction of cells (x, y) that do not have an aftershock ($A_i(x, y) = 0$) and for which an aftershock is wrongly predicted ($\pi_i(x, y) > \pi_{\text{th}}$).

By varying the threshold π_{th} we obtain a curve parameterized by π_{th} in the plane $(\text{FPR}(\pi_{\text{th}}), \text{TPR}(\pi_{\text{th}}))$. This curve is called Receiver operating characteristic (ROC). We associate to a ROC curve its Area Under the Curve, in brief AUC, which is used as a metric to assess the quality of the model. When the ROC coincides with the line FPR = TPR (and thus the associated AUC is 0.5) the predictions of the model are essentially random. When instead the ROC is above the line FPR = TPR the model performs better than random and any AUC around 0.66 and above is a fingerprint of decent to good classifier. As a complementary metric we use the balanced accuracy (ACC) defined as:

$$\text{ACC} = (\text{TPR} + 1 - \text{FPR})/2 \tag{3.19}$$

which can be also read as $\text{ACC} = \left(\frac{\text{num. true positives}}{\text{num. positives}} + \frac{\text{num. true negatives}}{\text{num. negatives}}\right)/2$. As the false and true positive rates are both functions of π_{th} we can maximize ACC (and, equivalently the difference $\text{TPR} - \text{FPR}$) to find the best threshold π^*_{th}. The value of the balanced accuracy at the optimal threshold will be the second metric to assess the quality of our models.

3.5 . Training procedure

Before fitting the models' parameters, the first task to carry out is to divide the available data in train, validation and test sets. The train data fits the model parameters while the validation assesses the training quality. When the train score is significantly higher than the validation score, the model is said to be overfit. Overfitting occurs when a model *memorizes* the train set, achieving very high scores, and cannot give accurate predictions for the validation set. The opposite scenario can occur - underfitting - where both the train and the validation scores are poor, signalling the need for either a more complex model (with more parameters and/or a different structure) or a better training procedure. Thus, a properly trained model minimizes the difference between validation and train score, keeping the overall performance high. Moreover, as different models might be used for the same task (in our case, we could change the convolution kernels, number of channels etc.), one must compare the validation score coming from different models to adjust for the best one.

Finally, the test score assesses the true capability of a model as the test set was never seen by the model, neither in the training phase nor in the validation one.

It's the score one would expect when the model is used, for example, in real-life applications.

The dataset we employed in this study refers to mainshocks occurring in the Japanese region with at least magnitude 6, in longitude interval $[123°, 148°]$ and latitude one $[22°, 46°]$, and between the year 2000 and 2019. For train and validation, we employed the mainshocks that occurred up to 2015. See figure 3.6.

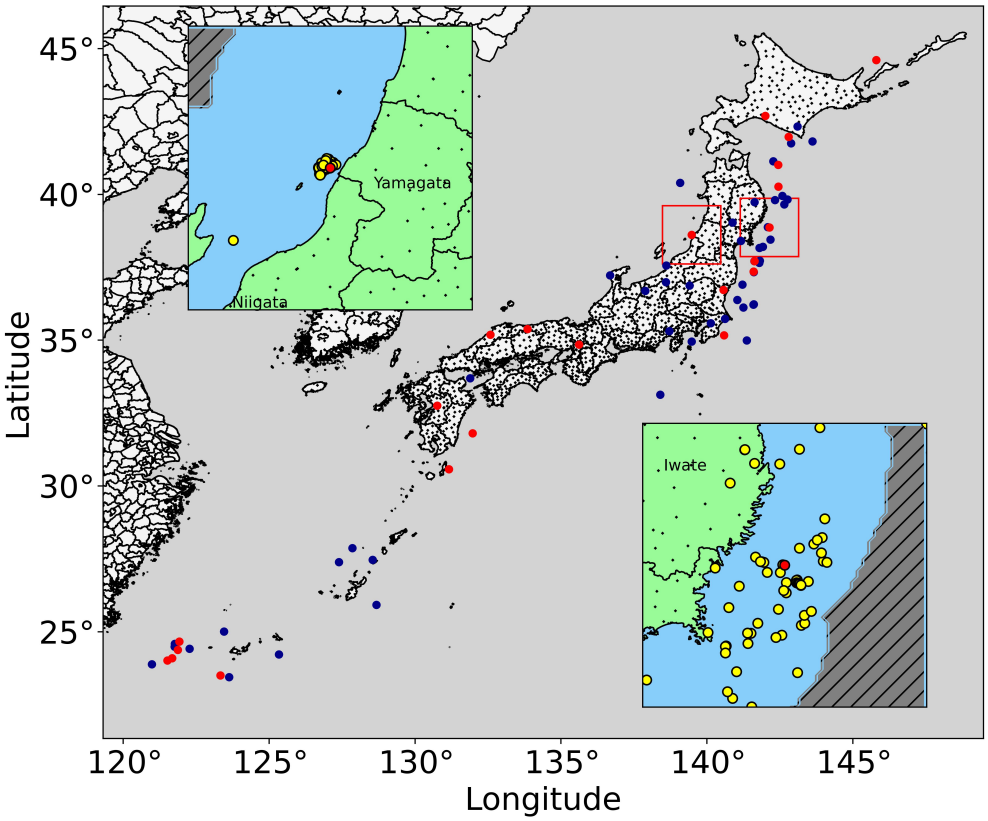

Figure 3.6: Map of Japan showing the mainshocks used for train (blue) and test (red). The two insets show two different earthquake sequences (in the test) with the corresponding aftershocks (in yellow). Small black dots are the station locations. The hatched regions correspond to the parts where the displacement map will be discarded, as no close station is available.

The total number of mainshocks is 71, with 48 in the training set and 23 in the test set. Such low number of samples is by no means adequate to train modern deep-learning models and there is a high risk of overfitting. With such a small dataset, how one splits the samples into train and validation can strongly influence the model quality. Indeed one can stumble upon a lucky split and obtain a very good model, while a slightly different one can end up in a poor quality one. To overcome this issue, we employ an ensemble approach. It consists in first fixing a model architecture and then training it on different splits of the train-validation set. In practice, one chooses a fraction $f_v = 0.2$ of samples for validation and trains a model on the remaining samples. Repeating this procedure N_m times by changing the validation samples, one obtains N_m different models trained on slightly different data. Given an earthquake i with input $(v_{r,i}(x,y), \cos\theta_i(x,y), \sin\theta_i(x,y))$, the output of the k-th trained model is $\pi_{i,k}(x,y) \in [0,1]$. From the N_m different prediction, we can construct a single prediction by aggregating the $\pi_{i,k}(x,y)$'s. One can use different protocols, but we stick to the most robust one, the median:

$$\pi_i(x,y) = \text{median}_{k=1\dots N_m} \pi_{i,k}(x,y) \tag{3.20}$$

The median is the most robust predictor. Indeed two other extremal protocols could be considered. For example, to maximize the predicted aftershocks one could consider taking the maximum along k. On the other hand, to minimize the number of false prediction, one could use the minimum. However both protocols are extremely sensitive w.r.t. to fluctuations in the train set used. In the following two section we show the results on the test set by using both the Logistic Regression approach and the CNN.

3.6 . Logistic Regression Baseline (LRB)

We first explore the results coming from logistic regression. As anticipated, a single model contains only two parameters; for the ensemble approach, we use $N_m = 50$ different models coming from the N_m different train/validation split. By combining these models and using the median aggregation we obtain the ROC curve in figure 3.7. In this case we obtain an AUC of 0.74 and an accuracy of 0.71: this shows that the amount of displacement at some location manages to predict strongly the occurrence of an aftershock.

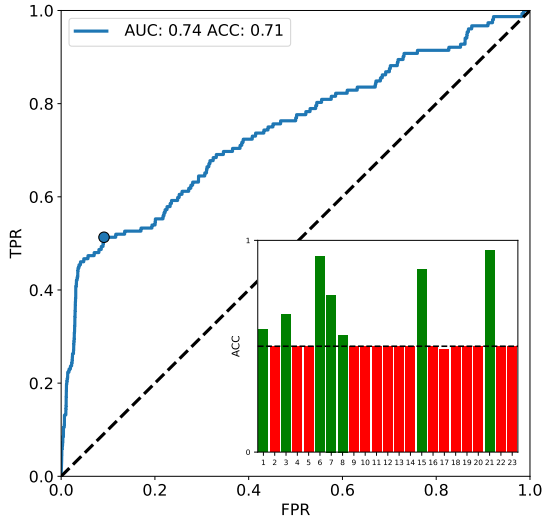

Figure 3.7: Logistic Regression Baseline (LRB) model: the ROC curves are obtained on the 23 mainshocks of the test set. The point of optimal balanced accuracy is outlined with a circle. Insets: balanced accuracies computed for each test set sample.

However, while the global metrics are promising, we must understand what happens to the single mainshocks analyzed. Specifically, we compute the accuracies of the prediction for each of the 23 mainshocks, as shown in the inset of figure 3.7. The red bars indicate an accuracy ≤ 0.5, the green one above it. As visible, only the minority of earthquakes have good accuracy (7 in total, with only 6 sensibly above 0.5), while for the rest the accuracy lands on 0.5, indicating the inability to make a meaningful prediction. What is crucial to understand is why such an imbalance occurs. We postpone this discussion to the next sections. Below instead we show the prediction maps for 3 mainshocks for which the LRB performs well:

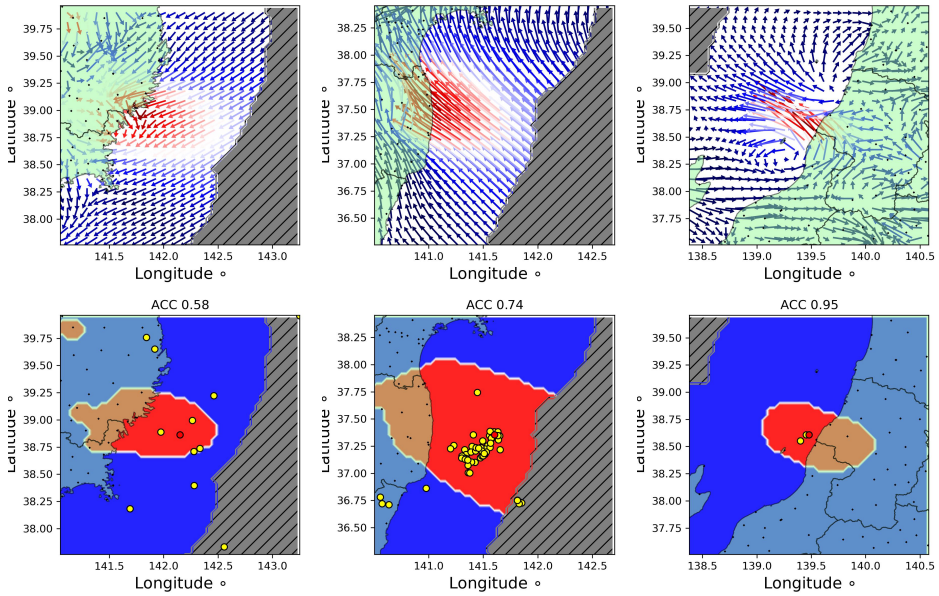

Figure 3.8: Top row: input of the logistic regression the color (blue to red) indicates the relative magnitude of displacement, the arrow the direction. The maps correspond to mainshocks number $1, 7, 21$ (see appendix for details). Bottom row: the logistic regression prediction. Red pixels correspond to those with $\pi(x, y) > \pi^*_{\text{th}}$, with π^*_{th} chosen to maximize the overall balanced accuracy. N.B.: we use the same π^*_{th} for all the maps. Yellow dots are aftershocks, the red one the mainshock.

3.7 . CNN

As for the simpler logistic regression, we trained $N_m = 50$ models and we used them to construct the prediction maps $\pi_i(x, y)$ using the median aggregation. In figure 3.9 we report the ROC with the corresponding AUC and ACC, specialized for the 23 mainshocks. The global accuracy and AUC is lower in the CNN case, however when specializing to single earthquakes we obtain 9 mainshocks with good predictions and none of them with poor one (the minimal accuracy for a mainshock is ≈ 0.65). The exploitation of spatial correlations, while not improving the global accuracy of the LRB method, manages to extract more information (as expected). This is even more clear when one looks at the prediction maps in figure 3.10, as in the CNN case they are not simply obtained by thresholding on the input displacement, thus showing more structure.

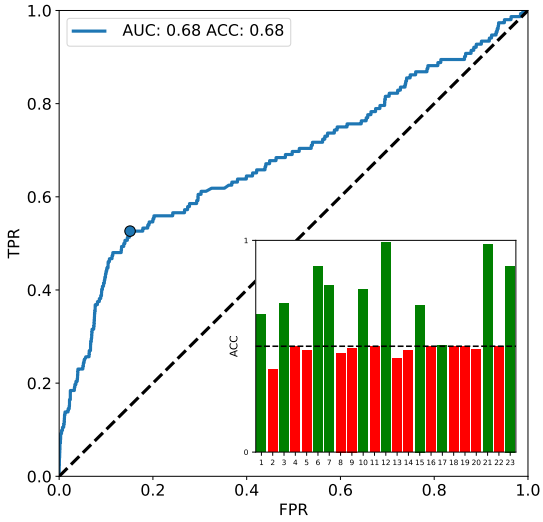

Figure 3.9: CNN model: the ROC curves are obtained on the 23 mainshocks of the test set. The point of optimal balanced accuracy is outlined with a circle. Insets: balanced accuracies computed for each test set sample.

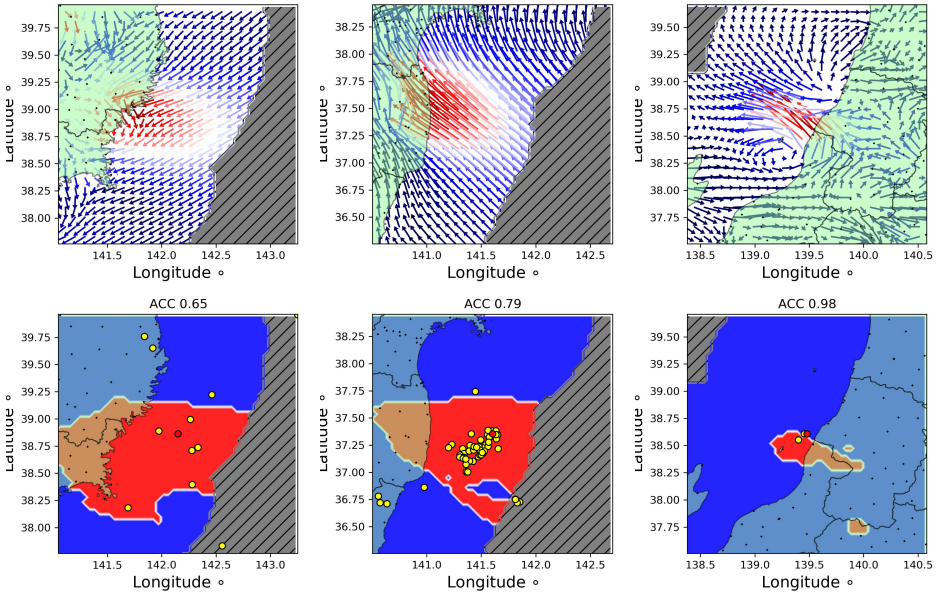

Figure 3.10: Top row: input of the CNN the color (blue to red) indicates the relative magnitude of displacement, the arrow the direction. The maps correspond to mainshocks number $1, 7, 21$ (see appendix for details). Bottom row: the CNN prediction. Red pixels correspond to those with $\pi(x, y) > \pi^*_{\text{th}}$, with π^*_{th} chosen to maximize the overall balanced accuracy. N.B.: we use the same π^*_{th} for all the maps. Yellow dots are aftershocks, the red one the mainshock.

3.8 . Interpreting the results

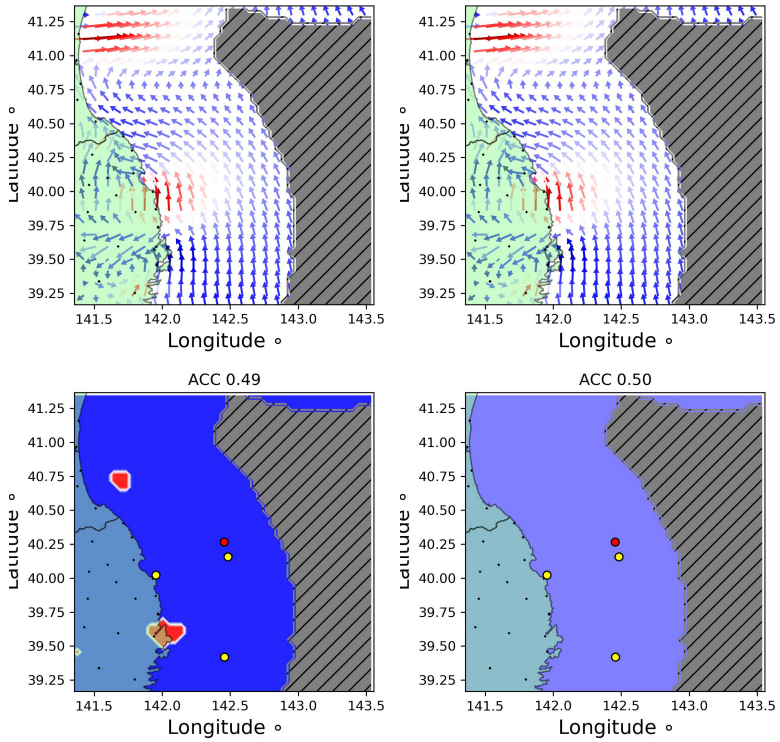

Figure 3.11: Study on the mainshock labelled as 9. Top: Input: surface displacement map. Bottom: Output: the prediction $\pi(x, y)$. Neither the CNN (left) nor the LRB (right) manages to outperform a random classifier. A possible origin of this failure is the fact that the main shock and most of the aftershocks happen in the sea. Thus, the interpolated surface deformation in those off-shore areas is not reliable.

With the LRB and CNN results in mind, we are ready to discuss the implications of the usage of GPS data in aftershocks forecasting. To begin, we find some earthquakes for which neither the LR not the CNN manage to make a satisfying prediction. One example is mainshock 9, for which we show the prediction map at the optimal threshold (obtained as explained before) in figure 3.11. For other, such as mainshock 10 in figure 3.12, the displacement magnitude is not sufficient to make meaningful predictions and thus the CNN outperforms the LRB. Overall we noticed that two different elements can influence the predictive power:

- The mainshock magnitude. As visible in summary table of appendix A, the better part of large earthquakes (with magnitude ≥ 6.7) are well classified.
- More importantly, the density of stations. All the earthquakes with only 1 station inside the image are poorly predicted (mainshocks $4, 5, 11, 18$). When

the number of stations is moderate (3 or slightly above) we obtain slighlty better performances, especially using the CNN. Japan is one of the regions in the world where GPS stations are more prominent. However, most of the epicenters are located offshore and as such the displacement measurements inshore are not sufficient to reconstruct a sufficiently informative displacement map.

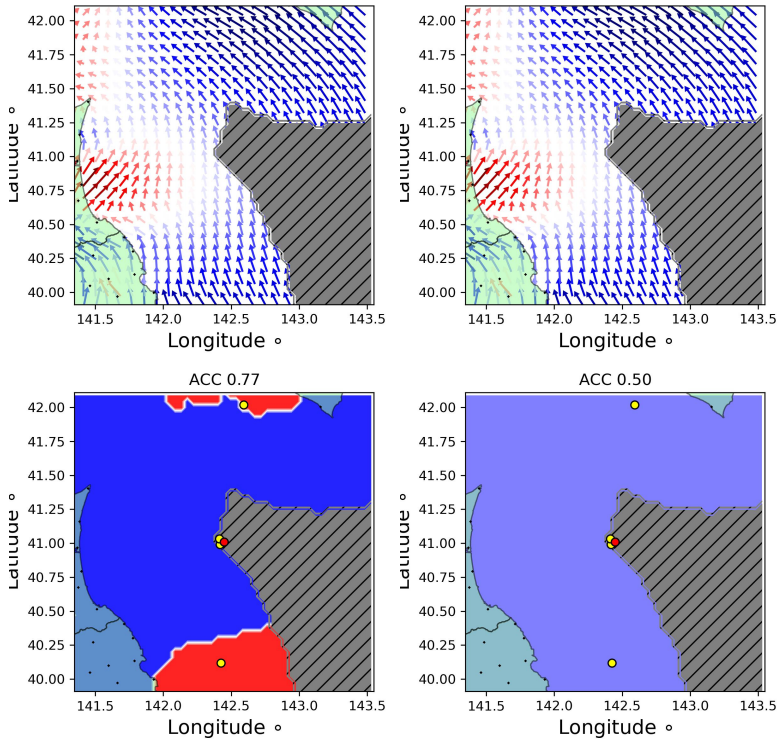

Figure 3.12: Study on the mainshock labeled as 10. Top: Input: surface displacement map. Bottom: Output: the prediction $\pi(x, y)$. The CNN (left) outperfoms the LRB (right). Such imbalance originates from the ability of the CNN to exploit better signals with low quality (large hatched areas).

3.9 . Conclusion and future work

In this chapter we dicussed the relevance of GPS data can in forecasting aftershocks. While having obtained satisfying results, we showed the limitations of such an approach, as it is heavily reliant on the station density and distribution. As anticipated, one possible improvement could come from extending the study to high-frequency GPS data (5 mins) in order to (1) include the aftershocks immediately following the mainshocks (2) have a more refined control over the earthquake dynamics. While the latter approach could be extremely promising, it could easily

lead to overfitting and, as such, it would require a strong preprocessing of the data in order to extract the main features, keeping the complexity of the model (relatively) low. On top of these improvements, one could have access to more data by including other regions in the world where the GPS station density is relatively high, such as the USA (especially California), New Zealand, Italy. For the purpose of enlarging the dataset, one could try to include synthetic GPS data constructed from ground rupture model, such as the popular Okada model [84]. Such an approach has been taken very recently in [80], where synthetic GPS data is used to predict the mainshock magnitude and location building up precisely on the Okada model, with promising results. Finally a heterogeneous approach would benefit enormously to the aftershocks prediction task i.e. one could include multiple data sources, such as waveforms, past catalog data and other geophysically relevant features.

Chapter 4

Darcy law and yield-stress fluids

In this chapter, based on the published paper "Darcy's law of yield stress fluids on a tree-like network" [22], we study the problem of the flow of a yield-stress fluid (a particular type of non-Netwonian fluid) embedded in a porous material. We first briefly review the Darcy's law, which describes the flow of Netwonian fluid in porous media to then discuss the numerical and analytical challenges introduced when dealing with a yield-stress fluid. We finally introduce an exactly solvable model that allows us to understand how the flow of such fluids grows in porous material.

4.1 . Darcy's law

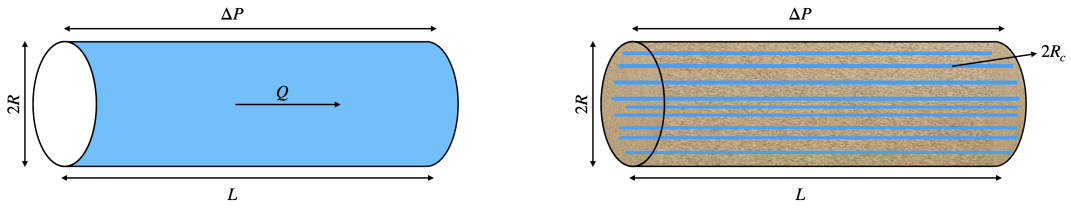

Figure 4.1: Left: schema for the Poiseuille law, with a tube filled with a Netwonian fluid (e.g. water). Right: schema for a tube filled with a porous material (e.g. sand) highlighting the small channels used in Darcy's derivation of his law.

Understanding the flow of fluids in complex structures is crucial for both human

and industrial applications. Seminal experiments [19] carried out by Henri Darcy in 1856 in Dijon showed that the mean flow rate Q of water passing through a porous material (in his case a cylinder filled with sand) is proportional to the applied pressure gradient and to a material dependent factor which he called *permeability*:

$$Q = \kappa R^2 \frac{P}{\eta L} \tag{4.1}$$

Here R the cylinder radius, L its length, η the fluid viscosity, P the pressure and κ the permeability. While Darcy originally believed that such a relation would hold only for water, it was later understood that the form of this law also holds for any Newtonian fluid. Thus, The only difference comes from different porous materials, solely affecting the permeability. For example, the permeability of sand or gravel is orders of magnitude larger than the one of clay. In its original form, Darcy's law 4.1 is in contrast with Poiseuille law that describes the flow of a Newtonian fluid in an empty cylinder (see figure 4.1 left):

$$Q_{\text{Pois}} = \frac{\pi R^4}{8\eta} \frac{P}{L} \tag{4.2}$$

Darcy noted this difference in the proportionality factor and he gave a simple explanation, which is crucial for understanding how flow develops in porous materials. Consider now a cylinder of length L and radius R filled with a porous material, say sand. A fluid is embedded in the material, and a pressure difference ΔP from top to bottom of the cylinder. Darcy imagined that the fluid could only flow along empty thin paths or *channels* present in the medium due to its intrinsic heterogeneity. In a first approximation, we can imagine that all the channels are non-intersecting and they all have a typical radius $R_c \ll R$. See figure 4.1 for a pictorial representation. As these channels can be treated effectively as empty cylinders of size L and radius R_c, we can apply the Poiseuille law to each of them individually, resulting in a flow rate per channel of:

$$Q_{\text{c}} = \frac{\pi R_c^4}{8\eta} \frac{\Delta P}{L} \tag{4.3}$$

As the channels are non-intersecting and identical in size the total flow rate in the cylinder is the sum of each flow rate coming from the individual channels. If we indicate with N_c the number of such channels we obtain:

$$Q = N_c \frac{\pi R_c^4}{8\eta} \frac{\Delta P}{L} \tag{4.4}$$

Now we want to relate this microscopic effective description to the macroscopic features i.e. to the radius of the cylinder. The total area covered by the tiny

channels is $N_c \pi R_c^2$ and the total area of the cylinder is πR^2 hence the density of channels is $n_c = N_c \pi R_c^2 / \pi R^2 = N_c R_c^2 / R^4$. By expressing the number of channels N_c w.r.t. its density we get:

$$Q = N_c \frac{\pi R_c^4}{8\eta} \frac{\Delta P}{L} = n_c \frac{R^2}{R_c^2} \frac{\pi R_c^4}{8\eta} \frac{\Delta P}{L} = \left(n_c \frac{\pi R_c^2}{8} \right) R^2 \frac{\Delta P}{L} \tag{4.5}$$

By defining the permeability as $\kappa = n_c \pi R_c^2 / 8$ we recover Darcy's law 4.1. This simple derivation reflects the fact that the permeability is a material property and depends essentially on the availability of channels in the porous medium. A natural question is: what would happen if we were to drop the non-intersecting channel assumption? In this case the permeability would be linked to the geometrical properties of the channels without affecting the linear form of the Darcy law and only the value of κ.

However, the linear nature of the Darcy's law is only valid for Netwonian fluids. Indeed, when considering non-Newtonian ones, the picture changes drastically as the form 4.2 of Poiseuille's law is no longer valid. Plenty of non-Netwonian fluids, natural or synthetic, exist. Among the many we find suspensions [85], gels [86], heavy oil [87], slurries, cement [88], and blood. Understanding how such fluids behave in porous structures is an important problem with many applications such as hydraulic fracturing, soil consolidation, and also medicine in the context of blood flow modeling.

Among non-Newtonian fluids, a relevant class is one of the yield-stress fluids for which a minimal applied stress is needed to make the fluid flow. Recent experiments [89] and numerical studies [90] on yield-stress fluids in porous material also showed that a minimal pressure P_0 below which no flow is observed. Moreover, it is observed that the permeability is not constant anymore and depends on the applied pressure, resulting in a non-linear flow curve (at variance with 4.1). In this chapter, after introducing some other known facts about the Darcy law for Newtonian fluids, we will attack the problem of yield-stress fluids and the corresponding Darcy law using tools from disordered systems and in the context of pore network models, which we describe in the following section.

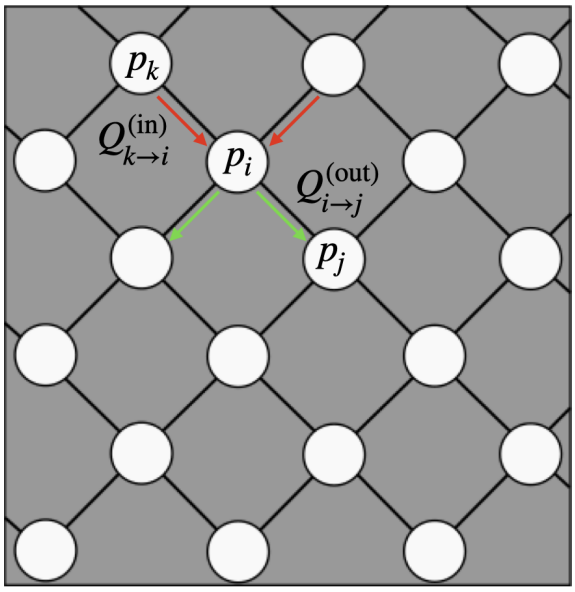

Figure 4.2: Example of a pore network. To each node/pore i we associate a pressure p_i and the in and out flows $Q^{(\text{in})}_{k\to i}$ and $Q^{(\text{out})}_{i\to j}$, with the constraint of flow conservation by the Kirchoff's law 4.6. In a link/throat, the relation between the flow $Q^{(\text{out})}_{i\to j}$ and $p_i - p_j$ is given by Poiseuille's law, which changes according depends to the type of fluid considered (Netwonian, yield-stress...).

The pore network model is one of the most popular and effective model used for describing a porous material. As in the original Darcy derivation, the porous medium presents one or more inlets (where a pressure P is applied) and one or more outlets (set at zero pressure). The inlet(s) and outlet(s) are connected by paths, also called *channels*, divided into nodes and links. The nodes represent the pores, which are void regions within the material and the links are the narrow channels, also called throats, that connect the pores together. Intuitively, the pore network model is equivalent to an electrical circuit where the links, the electrical current in a link is equivalent to the flow rate and the pressure to the electrical voltage.

The model's main assumption is that, when a fluid is present in the medium, the pressures are well-defined only at the level of the nodes. At the level of the link/throat, we impose the Poiseuille's law law relating the flow to the pressure difference between the nodes. The form of the Poiseuille's law however depends on the type of fluid considered i.e. Newtonian, yield-stress... Moreover, at the level of a pore/node, we impose the Kirchhoff's law: the incoming flow in a node i must be

equal to its outgoing flow:

$$\sum_k Q_{i\to k}^{(\text{out})} = \sum_k Q_{k\to i}^{(\text{in})} \tag{4.6}$$

where $Q_{m\to n}$ denotes the flow from node m to n. See figure 4.2 for a schematic example.

We will use another non-restrictive assumption, namely that we will only deal with directed networks i.e. between two nodes, the fluid has a preferential flow direction. This assumption greatly simplifies the calculations as the fluid is not allowed to come back on its path and is non-restrictive as the pressure gradient sets a preferential direction by itself.

4.3 . Newtonian fluids

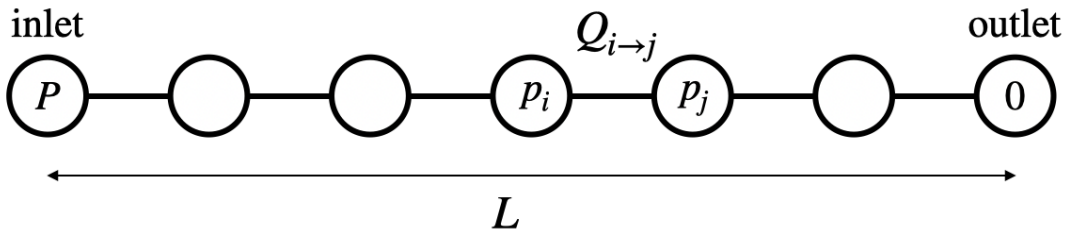

Figure 4.3: Geometry of the single channel. The inlet and the outlet are at pressure $P > 0$ and 0, respectively. The flow goes from left to right and the flow between the pores i and j is given by 4.7.

The first type of fluid we will treat is Newtonian fluid. While the objective of this chapter is to discuss yield-stress fluids, it is useful first to obtain results for the Newtonian case which is a limiting case of the non-Newtonian in the regime of high pressure. For the sake of simplicity, we are going to employ a reduced version of 4.2 for Newtonian fluids, namely that in a single throat/link the flow reads:

$$Q_{i\to j} = p_i - p_j \tag{4.7}$$

In this reduced version, we assume that each link has the same radius and we measure the flow in units of $\pi R^4/8\eta$. By using 4.6, we immediatly obtain that a single a channel with L links has a flow:

$$Q = \frac{P}{L} \tag{4.8}$$

where P is the pressure difference between the inlet and the outlet. See also figure 4.3 for a pictorial representation.

4.3.1 . Independent channels

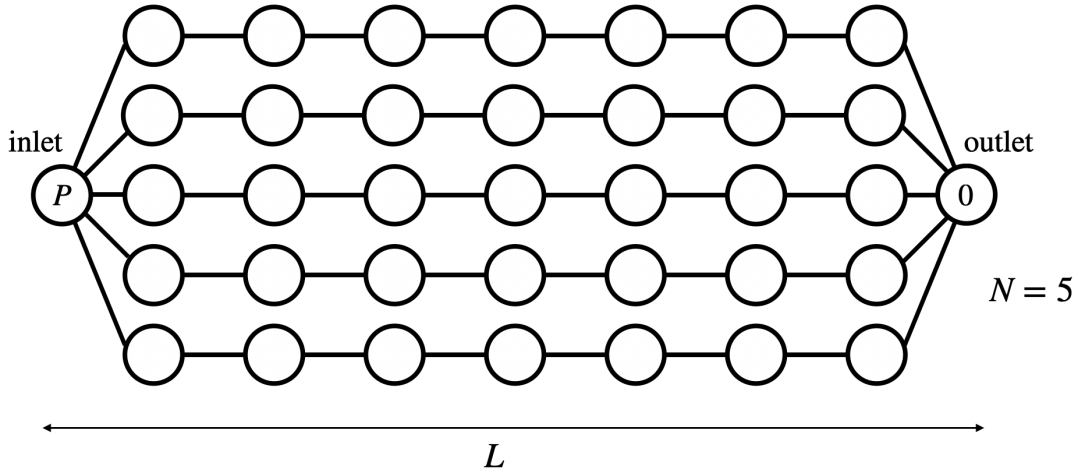

Figure 4.4: Geometry of the independent channels model. This network is obtained by combining N independent channels with L links each. The inlet and the outlet are at pressure $P > 0$ and 0, respectively.

If we combine together N independent channels with L throats (see figure 4.4), each with the same pressure drop, we reproduce Darcy's original derivation of its law. the same. Each channel sustains a flow $Q_c = P/L$ (see 4.8) and, as they are independent, the overall flow is:

$$Q = NQ_c = N\frac{P}{L} \tag{4.9}$$

The permeability here is simply proportional to the number of channels in the system i.e. $\kappa = N$, as in the original Darcy derivation.

4.3.2 . Tree-like network

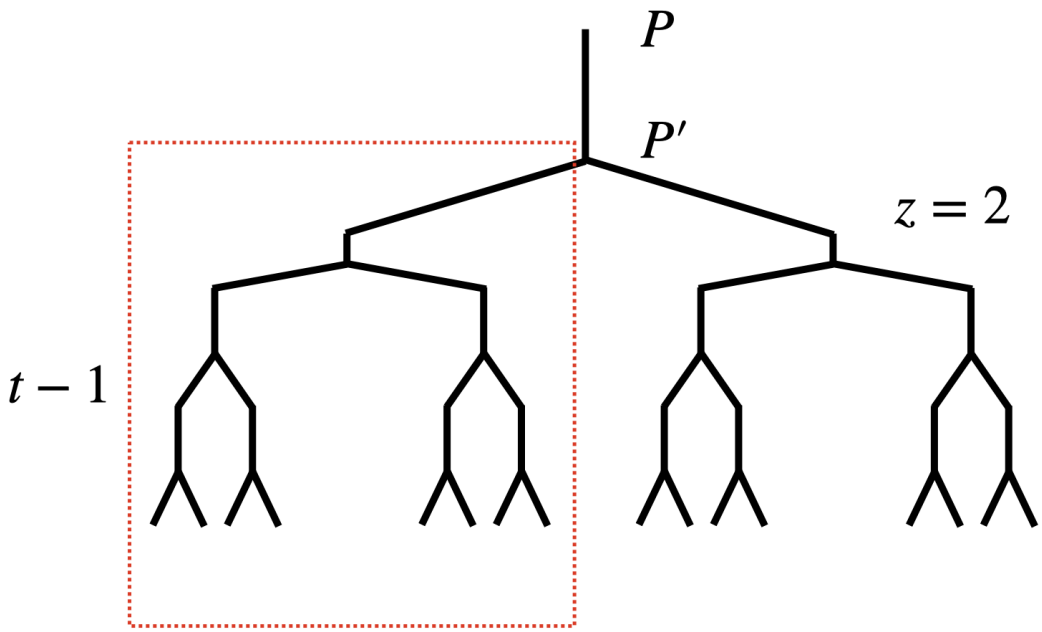

Figure 4.5: Flow of a fluid in a tree-like network of t levels. At the root a pressure P is applied and from the node (at pressure P') connected to the root two other independent tree of $t-1$ levels grow. The recursive structure of the tree allows a simple treatment of the Netwonian flow by recursion on t.

The first non-trivial case is the one of a Network with the geometry of a tree. Consider thus a tree with t levels and a branching ratio z (see **??**. We use the convention that the level $t = 1$ case is composed of two nodes, like in figure 4.5. The tree has a mathematically amenable structure that allows to write a recursive equation for the flow of a system with t levels in terms of one with $t-1$ levels. Indeed consider a tree with t levels where we apply a pressure P at the tree root. It can be thought as a collection of z trees with $t-1$ levels that are joint from the root to a new segment. See figure 4.5. Hence the flow satisfies the following relation:

$$Q_t(P) = zQ_{t-1}(P - P') \tag{4.10}$$

where P' is the pressure applied at the top of the z trees with $t-1$ levels. By Poiseuille 4.7 the flow on the top segment is equal to the pressure drop:

$$P - P' = zQ_{t-1}(P') \tag{4.11}$$

The left-hand side is the incoming flow from the inlet and the right hand side the one going inside the z trees. As the flow is linear in P, we can use the form $Q_t(P) = \kappa_t P$ and rewrite the equations for the permeability κ_t:

$$P - P' = z\kappa_{t-1}P' \tag{4.12}$$

which implies $P' = P/(1 + z\kappa_{t-1})$. Using 4.10 in conjunction with $Q_t(P) = \kappa_t P$ we get:

$$\kappa_t P = z\frac{\kappa_{t-1}}{1 + z\kappa_{t-1}}P \tag{4.13}$$

As $P \neq 0$:

$$\kappa_t = \frac{z\kappa_{t-1}}{1 + z\kappa_{t-1}} \tag{4.14}$$

Since $\kappa_1 = 1$ (a tree with one level is a single throat/link):

$$\kappa_t = \frac{(z-1)z^{t-1}}{z(z^t - 1)} \tag{4.15}$$

It is worth noticing that as $t \to \infty$

$$\kappa_\infty = \frac{z-1}{z} \tag{4.16}$$

which implies:

$$Q_\infty(P) = \frac{z-1}{z}P \tag{4.17}$$

A small remark: we use here the permeability as the constant of proportionality between Q and P. When expressing the flow with respect to the pressure gradient, here P/t, the permeability would read $t\kappa_t \approx t/2$ for large t.

4.4 . Darcy law for yield-stress fluids

So far we dealt with Newtonian fluids, for which the Poiseuille's law with the form 4.2 and 4.7 holds. However for the class of yield-stress fluids the Poiseuille law changes and is no longer linear in the pressure gradient: the fluid responds like a solid for low pressures (namely no flow is observed). In this case the Poiseuille gets modified as:

$$Q = \frac{\pi R^4}{8\eta}\left(\frac{P}{L} - \frac{\sigma_Y}{R}\right)_+^n \tag{4.18}$$

with $(x)_+ = \max(x, 0)$, σ_Y the yield-stress threshold and n describes the non-linearity of the fluid. As mentioned before, recent numerical studies [90–93] on the flow of such fluids in porous material have shown how there exists a minimal applied pressure P_0 below which no flow is observed. On top of this the flow rate displays three regimes for $P > P_0$:

$$Q(P) \propto \begin{cases} (P - P_0) & P \gtrsim P_0 \\ (P - P^*)^\beta & P_0 \ll P \ll P_{\text{sat}} \\ (P - P_{\text{sat}}) & P \gg P_{\text{sat}} \end{cases} \tag{4.19}$$

where P_0 is the minial opening pressure, P^* and P_{sat} are the pressure at which the non-linear and Netwonian regime occur. The first linear regime has a very small permeability, as only one of few channels flow. The non-linear regime is associated instead with a quick growth of the permeability of the system and this regime is the one we want to focus on. Finally the last regime, linear in P, is the Netwonian regime, called as such because when the pressure is sufficiently high, the permeability saturates to the Netwonian value κ_∞ as all the channels start to flow. .

We mainly focus on $n = 1$, the class of Bingham fluids. To simply the calculations we used a reduced form of 4.18 by setting to one its prefactor and we relabel the pressure $\sigma_Y L/R$ as τ. This form of the Poiseuille law thus becomes:

$$Q = \frac{1}{L}(P - \tau)_+ \tag{4.20}$$

where L still represents the length of the throat, that we also set to 1:

$$Q = (P - \tau)_+ \tag{4.21}$$

4.4.1 . Single-channel system

The first and most simple pore network model we study is the one-channel model. Namely we consider a porous medium with a single channel made of a number t throats. To model material heterogeneity the yield stress threshold in each throat is a random variable distributed according to a distribution $\rho(\tau)$. We can thus label the nodes as $i = 1, \ldots, t + 1$, and each node will hold a pressure p_i. The boundary conditions are $p_1 = P$ and $p_{t+1} = 0$. The flow from node i to node $i + 1$ is thus:

$$Q_{i,i+1} = (p_i - p_{i+1} - \tau_i)_+ \tag{4.22}$$

where τ_i is defined for $i = 1, \ldots, t$. As we are dealing with a single channel system in order to have a non-zero flow rate at each throat the pressure drop $p_i - p_{i+1}$ must be larger than the corresponding threshold τ_i. So assuming this hold Kirchoff's law imposes on a node:

$$Q_{i-1,i} = Q_{i,i+1} \tag{4.23}$$

As the throats are all in series, the flow is the same in each throat and equal to a value Q. Using thus

$$Q = p_i - p_{i+1} - \tau_i \tag{4.24}$$

and summing over $i = 1 \ldots t$ we get:

$$tQ = \sum_{i=1}^{t} P_i - \sum_{i=1}^{t} P_{i+1} - \sum_{i=1}^{t} \tau_i = p_1 - p_{t+1} - \sum_{i=1}^{t} \tau_i \tag{4.25}$$

as $p_1 = P$ and $p_{t+1} = 0$ we get:

$$Q = \frac{P - \sum_{i=1}^{t} \tau_i}{t} \equiv \frac{P - P_0}{t} \tag{4.26}$$

Equation 4.26 gives thus the condition for a non-zero flow which simply reads:

$$P > P_0 \equiv \sum_i \tau_i \tag{4.27}$$

which also reads:

$$Q(P) = \begin{cases} 0 & P < P_0 \\ \frac{P - P_c}{t} & P > P_0 \end{cases} \tag{4.28}$$

with P_0 a random variable distributed as the sum of t random variables with p.d.f. $\rho(\tau)$, which we call $\rho_t(P_0)$. For large t we can assume, as long as $\rho(\tau)$ has a first and second moment, that:

$$\rho_t(P_0) \sim \frac{1}{\sqrt{2\pi\sigma^2 t}} \exp\left(-\frac{(P_0 - t\bar{\tau})^2}{2\sigma^2 t}\right) \quad \text{as} \quad t \to \infty \tag{4.29}$$

hence P_0 ha an average $t\bar{\tau}$ with $\bar{\tau} = \int_{\mathbb{R}} \tau\rho(\tau)d\tau$ and variance $\sigma^2 t$ with $\sigma^2 = \int(\tau - \bar{\tau})^2\rho(\tau)d\tau$.

4.4.2 . Independent channels or the fiber-bundle model

As we did for the Newtonian case, a straight generalization of the single channel model is a pore network with independent N channels each of length t all put at the same pressure gradient (see schema 4.4). In literature, this model of a porous network is also known as fiber-bundle model. As each individual channel has a minimal opening pressure $P_{0,i}$ with $i = 1 \ldots N$ distributed according to $\rho_t(P_{0,i})$ in 4.29, there will be a minimal opening pressure among the N

$$P_0 = \min_{i=1\ldots N} P_{0,i} \tag{4.30}$$

The minimal pressure P_0 is such that for $P < P_0$ no flow rate is measured $Q(P) = 0$ and just above it $P > P_0$, $Q(P) > 0$.

As the individual opening pressures $P_{0,i}$ are independent random variables we can use extreme value statistics tools to determine the behavior of P_0.

We are interested in the limits of large channel lengths $t \to \infty$ and large number of channels $N \to \infty$. Thanks to the Gaussian nature of the $P_{0,i}$'s for large t 4.29, we can limit ourselves to the extreme value statistics of gaussian random variables. The probability to have P_0 larger than some value ϵ reads:

$$\text{Prob}[P_0 > \epsilon] = F_t(\epsilon)^N \tag{4.31}$$

with $F_t(\epsilon) = \int_\epsilon^\infty d\tau \rho_t(\tau)$ the inverse cumulative distribution of $\rho_t(P_{0,i})$:

$$F_t(\epsilon) = \frac{1}{2}\text{erfc}\left(\frac{\epsilon - t\bar{\tau}}{\sqrt{2t\sigma^2}}\right) \tag{4.32}$$

with $\text{erfc}(\tau) = \frac{2}{\sqrt{\pi}}\int_\tau^\infty e^{-x^2}dx$. As we are interested in the minimum, the relevant limit at which we need to look is $\epsilon \to -\infty$:

$$F_t(\epsilon) \sim 1 + \frac{\sqrt{t}\sigma e^{-\frac{(\epsilon - t\bar{\tau})^2}{2\sigma^2 t}}}{\sqrt{2\pi}(\epsilon - t\bar{\tau})} \tag{4.33}$$

To find the typical value of P_0 we shift the variable $\epsilon = a_N + b_N u$ and try to look at a finite limit of:

$$F_t(a_N + b_N u)^N \tag{4.34}$$

as $N \to \infty$. Following the derivation in [34] we obtain:

$$\begin{aligned} a_N &= t\bar{\tau} - \sigma\sqrt{t}\left[\sqrt{2\ln N} - \frac{\ln(2\sqrt{\pi \ln N})}{\sqrt{2\ln N}}\right] + \dots \\ b_N &= \frac{\sigma\sqrt{t}}{\sqrt{2\ln N}} + \dots \end{aligned} \tag{4.35}$$

We now consider a precise scaling for N with t, namely $N = k^t$ with $k > 1$. In this case equation 4.35 becomes:

$$\begin{aligned} a_{N=k^t} &= t\bar{\tau} - \sigma t\sqrt{2\ln k} + \sigma\frac{\ln(2\sqrt{\pi t \ln k})}{2\sqrt{2\ln k}} + \dots \\ b_{N=k^t} &= \frac{\sigma}{\sqrt{2\ln k}} + \dots \end{aligned} \tag{4.36}$$

$$\tag{4.37}$$

As b_N at leading order is independent of t we label $1/b_N = \beta_c$, for reasons that will become clear later. This derivation implies that the minimum pressure P_0 has a typical value $\overline{P_0}$ (at leading order in t):

$$\overline{P_0} \sim t(\bar{\tau} - \sigma\sqrt{2\ln k}) \tag{4.38}$$

Its fluctuations are given by u, a random variable with law:

$$\lim_{N\to\infty} F_t^N(a_N + b_N u) = e^{-e^u} \tag{4.39}$$

which corresponds to a Gumbel random variable. Now that we characterized the minimal pressure we are ready to study the full flow curve. Consider thus $Q(P)$ for a given realization of the $P_{0,i}$s:

$$Q(P) = \sum_{i=1}^{N} \frac{(P - P_{0,i})_+}{t} \tag{4.40}$$

As for $P < P_0$ the flow is zero, it is convenient to express P as $P = x + P_0$. Therefore the flow reads:

$$Q(x) \equiv Q(x + P_0) = \sum_{i=1}^{N} \frac{(x + P_0 - P_{0,i})_+}{t} \tag{4.41}$$

We can now introduce the quantity:

$$m(x) = \sum_{i=1}^{N} \theta(x - (P_{0,i} - P_0)) \tag{4.42}$$

which counts the number of channels flowing at the pressure P. Using the derivative of $m(x)$:

$$\frac{dm(x)}{dx} = \sum_{i=1}^{N} \delta(x - (P_{c,i} - P_c)) \tag{4.43}$$

we can express the flow in an integral form:

$$Q(x) = \frac{1}{t} \int_0^x dx'(x - x') \frac{dm}{dx'}(x') \tag{4.44}$$

As $m(x)$ is a random variable, we can study it using order statistics. The probability of it being equal to $n + 1$ reads

$$P(m(x) = n + 1) = N \binom{N-1}{n} \int \rho_t(\epsilon)[F_t(\epsilon) - F_t(x + \epsilon)]^n F_t^{N-n-1}(\epsilon + x) \tag{4.45}$$

Its average value thus reads:

$$\overline{m(x)} = \sum_{n=0}^{N-1} (1+n) P(m(x) = n+1) = 1 + N(N-1) \int d\epsilon \rho_t(\epsilon)[F_t(\epsilon) - F_t(x+\epsilon)] F_t(\epsilon + x)^{N-2} \tag{4.46}$$

By using the scaling $\epsilon = a_N + b_N u$ for $N = k^t \to \infty$ obtained before we get:

$$\overline{m(x)} = 1 + \int du e^{2u - e^u} (e^{\beta_c x} - 1) = e^{\beta_c x} \tag{4.47}$$

Thus the average flow reads:

$$\overline{Q(x)} = \frac{1}{t} \int_0^x dx'(x - x') \overline{\frac{dm}{dx'}(x')} = \frac{e^{\beta_c x} - 1}{\beta_c t} \tag{4.48}$$

The average permeability can be obtained by taking a derivative w.r.t. x:

$$\overline{\kappa(x)} = \frac{d\overline{Q(x)}}{dx} = \frac{1}{t} e^{\beta_c x} \tag{4.49}$$

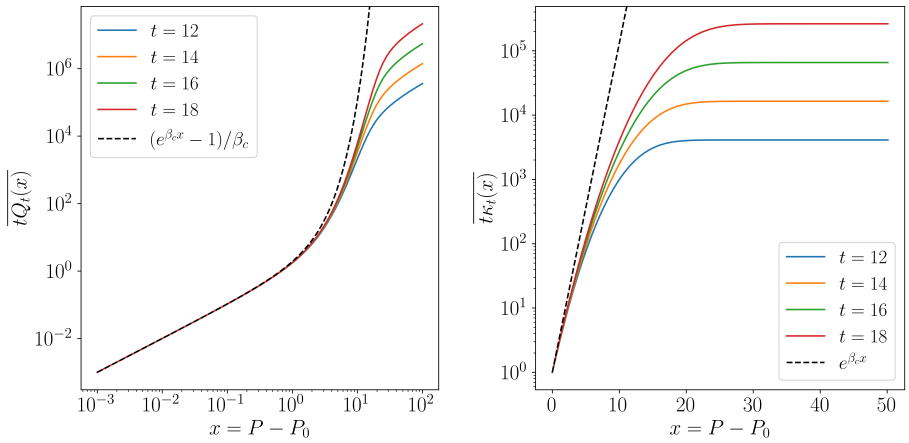

Figure 4.6: Left: Flow, rescaled by t, in the fiber bundle model. The two linear regimes, the low-pressure and high-pressure Netwonian regimes are clearly visible and the non-linear one connects the two. In the non-linear regime, the permeability has an abrupt growth from order $1/t$ to order k^t/t. We compare the flow curves for moderate $t = 12, 14, 16, 18$ and we see a slow but definite convergence towards the exponential behavior. Right: permeability, scaled such that $t\kappa_t(0) = 1$. As for the flow, the convergence towards the limiting behaviour $e^{\beta_c x}$ is extremely slow in t.

One can notice a striking similarity (and, in fact, a one-to-one mapping) between this fiber-bundle model and the Random Energy Model (REM) in statistical physics [94]. And indeed the quantity $m(x)$ coincides with the counting statistics of the states in the REM and the number β_c, which here has the interpretation of an inverse pressure, coincides with the freezing inverse temperature of the REM i.e. the temperature below which the entropy of the REM freezes and remains constant. Going back to the permeability, its maximal value is k^t/t as it is reached as soon as all the k^t channels flow. We can thus identify a typical pressure $x_{\text{sat}} = P_{\text{sat}} - P_0$ for which the permeability stops growing:

$$\kappa(x_{\text{sat}}) = \frac{k^t}{t} \tag{4.50}$$

i.e.

$$P_{\text{sat}} = \frac{1}{\beta_c} \ln t + P_0 \tag{4.51}$$

This result implies that only a small pressure increase above P_0 is needed to reach a maximal value for the permeability and this pressure increase grows sub-linearly with the system size t. In figure 4.6 we compare these anaytical results with numerics. As it is known from extreme value statistics [32], the $t \to \infty$ convergence is extremely slow and thus we expect a slow convergence to the exponential law in 4.48.

4.5 . Two-dimensional models

As the channels are non-intersecting, the fiber bundle model works as a 'mean-field' of the pore network models. This results is no competition in the sequence of opening channels between the quenched randomness of the yield-stress thresholds and the spatial organization of the channels. However, it is extremely challenging to study analytically a model where channels are overlapping. A step forward has been made in [95] where the flow of a yield-stress fluid has been considered in a more realistic two-dimensional medium. The geometry considered is a two-dimensional grid tilted by 45 degrees, like a diamond-shaped lattice (see figure 4.8). The fluid is put at pressure P at the top pore of the grid (inlet) and pressure 0 the bottom pore (outlet). A single channel flowing from the inlet pore to the outlet can contain, a priori, loops. However such configurations are negligible [95] and thus only directed paths are considered. Each inlet-outlet channel has a length L, namely L throats participate to it. As before, between two nodes/pores i and j the following Poiseuille law is considered:

$$Q_{ij} = (p_i - p_j - \tau_{ij}) \tag{4.52}$$

where τ_{ij} is a random number. As before, in order to characterize the flow, it is important to first study the statistics of the minimal opening pressure P_0 and the corresponding first opening channel. The important point of [95] is that there is a direct mapping between the this channel and the ground state of a directed polymer in a random medium. The mapping works as follows. Consider all the possible paths between the inlet and the outlet when no flow occurs. Each single channel has an opening pressure equal to the sum along the channel of all its thresholds τ_{ij}. So to open the first channel we need to find the one with the minimal opening pressure. In formula:

$$P_0 \equiv \min_{(i,j)\in\mathcal{C}} \tau_{ij} \equiv \min_{\mathcal{C}} \tau(\mathcal{C}) \tag{4.53}$$

where $\mathcal{C}$ denotes a path from the inlet to the outlet and $\tau(\mathcal{C})$ indicates the sum of the thresholds along the channel. As we consider only directed paths, we can identify the various $\tau(\mathcal{C})$ with *energies* of a directed polymer in $1+1$ dimensions. As such, first channel $\mathcal{C}_{\min}$ has an opening pressure P_0 that identifies with the ground state of the model of the directed polymer in random media. As such it is known that [49]:

$$P_0 = -\overline{p_0}L + L^{1/3}\chi \tag{4.54}$$

where χ is a random variable with Tracy-Widom distribution [96]. Numerically, a brute-force approach to search this minimum is unfeasible, as one would need to sort 2^L variables. However, as pointed out in [95], the Djistrka algorithm can help

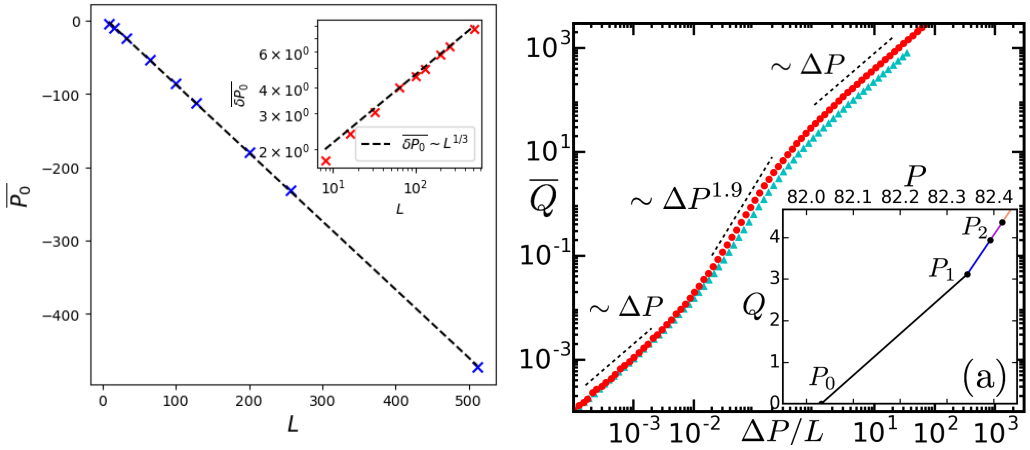

Figure 4.7: Left: typical value of P_0 in the 2d Darcy problem. Inset: fluctuations of P_0 around its typical value. As predicted by the theory of directed polymer in random media [49], fluctuations grow as $L^{1/3}$. Right: average flow curve for a yield-stress fluid in a 2d porous medium, from [95]. The three regime are highlighted, with the non-linear regime connecting the low to the Newtonian permeability ones. Colors stand for different distributions of disorder (gaussian and uniform). Inset: a single realization of the flow. As a function of pressure, the flow is a piecewise linear function. The slope corresponds to the (increasing) permeability and each new linear portion corresponds to a newly flowing channel.

in the task reducing the complexity to $O(L^2)$. In figure 4.7 left, we show the average opening pressure's linear scaling and its fluctuations in the inset.

Having found the ground state channel, we need to find the opening pressures $P_1, P_2, P_3, \ldots$ of subsequent flowing channels. In the [95] this task was attacked numerically in two ways: by extending the Djistrka algorithm and by using a gradient descent technique (this latter useful for the high-pressure limit). Here, we will follow the first method and we remind to the original work for a derivation [95]. The method can be described as following:

- First, at a given channels configuration, one solves Kichoff's equation and finds how the pressure p_n at a node n depends on the inlet pressure P i.e. one obtains $p_n = a_n P + b_n$ for all the flowing nodes.
- Second, one fixes two pores m and n and finds the channel with minimal energy $\tau_{m,n}$ between m and n using the Djistrka algorithm.
- Finally, the new channel is the one that minimizes $(\tau_{m,n} - (b_m - b_n))/(a_m - a_n)$ among any two pores m, n.

By using this modified Djistrka algorithm, the flow curve observed is compatible with the experimental observation for which a non-linear behavior kicks in as soon as the

first few channels have opened i.e. $Q(P) \sim (P-P_0)^\beta$ with $\beta \approx 1.9$ as shown in figure 4.7 right. Close to P_0 the behavior is linear as the ground state typically dominates the flow. The non-linear regime stops for high pressures: in this regime permeability starts to saturate as the opening of new channels does not affect it sensibly, kicking a Newtonian-like regime. In [95], it was understood that the non-linear of both the flow and the permeability is determined by the opening of new channels with low overlap (i..e low number of common links) with the already flowing configuration. However quantifying this mechanism is particularly challenging in the 2d model, for both numerical and analytical difficulties. In the next section, we study a model for which this observation can be properly tested. Indeed we consider the geometry of a porous medium with a tree-like structure. The tree-like structure, while less realistic than the 2d one as no loops can be formed i.e. two channels after separating never cross again, has the important feature of being analytically tractable (besides the determination of P_0).

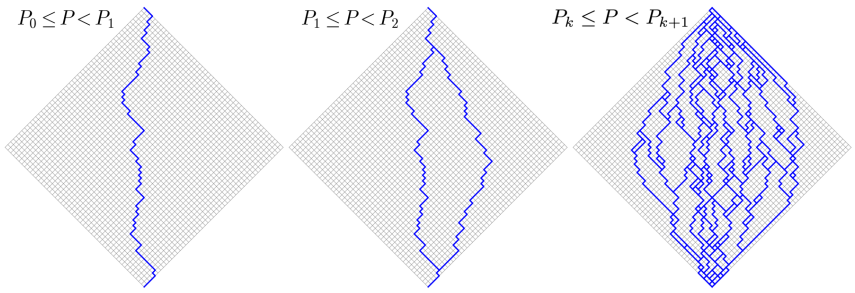

Figure 4.8: A spatial depiction of the three regimes of the flow in the 2d model. On the left the system is at pressure close to P_0 and thus only one channel flows. As more channel start to open the growth of the flow rate grows non-linearly (middle figure) until the system has been fully 'invaded' and thus the flow resembles a Netwonian one (right figure).

4.6 . Darcy flow in a tree-like pore network

In this section we present the problem of the flow of yield-stress fluids in a tree-like pore network. As it often occurs in statistical physics, models on a tree as they exhibit recursive structures, are more amenable to analytical prediction and can give us important insights on systems on a regular lattice. In our case, the model is indeed analytically tractable and gives us important information on the role of the overlap between flowing channels in the growth of the flow and the permeability as pressure increases

Consider thus a binary tree with t levels. To each link in the tree is associated a yield stress threshold τ_{ij} distributed according to some $\rho(\tau)$. In a binary tree there

are $N_P = 2^{t-1}$ paths/channels that connect the inlet (the tree root) to the outlets (see figure 4.5). The inlet has a pressure P and the outlet a pressure 0. As in the case of a two-dimensional pore network, we can associate to each path α an energy ϵ_α by summing all the thresholds in the links along the given path:

$$\epsilon_\alpha = \sum_{(ij)\in\alpha} \tau_{ij} \tag{4.55}$$

Each channel α is thus a directed polymer connecting the inlet to the corresponding outlet carrying an energy ϵ_α. As in the two dimensional case, the first channel that flows in the system corresponds to the channel with minimal energy i.e. to the ground state of a directed polymer in random media. If now we re-label the paths according to their energies $\epsilon_0 < \epsilon_1 < \dots$, the minimal energy identifies with ϵ_0 and thus $P_0 = \epsilon_0$. Denoting with P_i the pressure at which the $(i+1)$-th channel starts to flow, flow rate $Q_t(P)$ reads

$$Q_t(P) = \frac{1}{t}(P - P_0) \quad P \in [P_0, P_1) \tag{4.56}$$

To understand what happens for subsequent channels we can use a simple physical argument, grounded in the flow continuity (Kirchoff). When a single channel flows, if we increase the pressure from P to $P + \delta P$, the pores at the top of the channel will feel an increase in their pressure of order δP while channels at the bottom an increase of $\delta P/t$. As such, it is easier for channels originating from the top to start to flow with respect to the bottom ones. In other words, channels sharing few common links with the flowing one i.e. channels with low-overlap are favored to start flowing at lower pressures. We can precisely quantify how the overlap affects the flow of new channels by looking at the expression for P_1 (the pressure at which the second channel starts to flow, see appendix B for a derivation):

$$P_1 = \epsilon_0 + \min_{\alpha\neq 0} \frac{\epsilon_\alpha - \epsilon_0}{1 - \hat{q}_{0\alpha}/t} \equiv \epsilon_0 + \frac{\epsilon_{\alpha_1} - \epsilon_0}{1 - \hat{q}_{0\alpha_1}/t} \tag{4.57}$$

with α_1 denoting the channel minimizing (4.57). Here α labels any channel different from the ground state and $\hat{q}_{0\alpha}$ their overlap i.e. the number of common links (see figure 4.9). By construction $\hat{q}_{0\alpha}$ can range from 1 to $t-1$. The expression for P_1 explicitly involves two factors. The first is (as might be expected) the difference in energy between any channel α and the ground state: a channel with lower energy is more likely to flow. The second factor, as anticipated, is the overlap, which biases the minimization towards channels with low $\hat{q}_{0\alpha}$. This mechanism holds also for the pressure of subsequent channels $P_2, P_3, \dots$. In appendix B we explicitly show that this is also the case for P_2. For the other channels the analysis becomes too complicated. However in the next section we show how a major simplification occurs for large t, leading to an explicit determination of the flow.

4.6.1 . Large t limit

We already discussed the mapping between the channels and the directed polymer. The directed polymer problem on a tree has been introduced in the seminal paper by Derrida and Spohn in [97] and extensively studied thereafter [98–102] using the tools of the Kolmogorov–Petrovsky–Piskunov (KPP) equation. We review some of the main known results in appendix C. Using the tools from the KPP equation one can show that the typical value taken by $P_0 = \epsilon_0(t)$ is:

$$\overline{\epsilon_0(t)} = \bar{\tau} t - c(\beta_c) t + \frac{3}{2\beta_c} \ln t + O(1) \tag{4.58}$$

where $\bar{\tau}$ is the average value of $\rho(\tau)$ and $c(\beta_c)$ and β_c are defined by

$$\begin{aligned} c(\beta) &= \tfrac{1}{\beta} \log \left(2 \int d\tau \rho(\tau) e^{-\beta \tau} \right) \\ \beta_c &= \arg\min_\beta c(\beta) \end{aligned} \tag{4.59}$$

Both β and β_c, as in the case of the REM, have the interpretation of inverse temperature. Precisely β_c is the inverse freezing transition temperature of the directed polymer on the tree and, more generally, of a family of log-correlated random energy models (Log-REM), all in the same universality class. The freezing transition, namely the fact that the entropy of the polymer remains zero for $\beta > \beta_c$, has important consequences on the distribution of states above the minimum and this fact will be important later on. Moreover, the fluctuations of $\epsilon_0(t)$ around its typical value are also known and they deviate from the Gumbel distribution of the standard fluctuations of minima of uncorrelated random variables [32].

Now that we have enough information above P_0, we need to study the states above the ground state in order to connect them to the subsequent flowing channels. The directed polymer on a tree shows one-step replica symmetry breaking (1-RSB). Systems with 1-RSB, at low temperatures, display an organization of the states above the ground state with either $\hat{q}/t \to 0$ or $\hat{q}/t \to 1$ for $t \to \infty$. Moreover, because of the freezing transition, the number of states close in energy to the ground state is size independent, as the extensive entropy is zero. Consequently, such states have either a small $\hat{q} \sim 0$ or large overlap $\hat{q} \sim t$. From equation 4.57 the channels with high overlap with the ground states would have large opening pressure P_1. Hence among the low-energy states the first channels to open will coincide with those with low-overlap among them. A series of channels with low overlap display energies that are almost uncorrelated and the total flow in the system comes from the individual contribution of each low-overlap path, much like the independent channels/fiber bundle case. Thus finding the flow curve reduces to the problem of

enumerating the low-energy states above $\epsilon_0(t)$ with the constraint of having low overlap among them.
To confirm this intuition we can perform a rigorous calculation: we introduce a quantity $m_{\hat{q},t}(x)$ which counts the number of states above $\epsilon_0(t)$ that have at most $x + \epsilon_0(t)$ energy and maximal overlap $\hat{q}$ among them (see figure 4.9 for a pictorial example of maximal overlap).

The quantity $m_{\hat{q},t}(x)$ is different with respect to the density of states above $\epsilon_0(t)$, which we label $m_t^{(\text{full})}(x)$. It counts, in a tree with t levels, the number of states with energy below $x + \epsilon_0(t)$. These states, in the large t limit, have either $\hat{q} \sim 1$ or $\hat{q} \sim t$ and their number, thanks to the freezing transition, is constant and size independent. Thus for energy gaps $x = O(1)$, in the limit $t \to \infty$, $m_t^{(\text{full})}(x)$ exists finite. The study of $m_t^{(\text{full})}(x)$ has been extensively studied by Derrida and Brunet [101] using the tools from the KPP equation. They have shown that its average value $\overline{m_t^{(\text{full})}(x)}$, for large t, grows as:

$$\lim_{t\to\infty} \overline{m_t^{(\text{full})}(x)} = Axe^{\beta_c x} \tag{4.60}$$

with A a constant [101]. In appendix C we discuss the methods to obtain $m_t^{(\text{full})}(x)$. The existence of a finite limit for $m_t^{(\text{full})}(x)$ implies that the $t \to \infty$ limit of $m_{\hat{q},t}(x)$ exists finite, as by construction $0 < m_{\hat{q},t}(x) < m_t^{(\text{full})}(x)$ for any t.

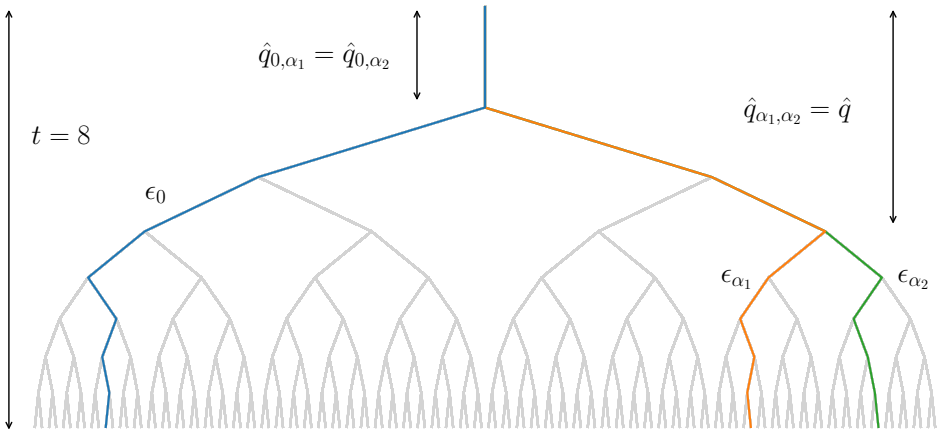

Figure 4.9: Example of three channels $0, \alpha_1, \alpha_2$ flowing with maximal overlap $\hat{q} = 3$ for a tree with $t = 8$ levels. Channel 0 (the ground state) and the other two α_1, α_2 share an overlap $\hat{q}_{0\alpha_1} = \hat{q}_{0\alpha_2} = 1$ and α_1 and α_2 an overlap $\hat{q}_{\alpha_1\alpha_2} = 3$ hence the maximal overlap is precisely $\hat{q} = 3$.

On the other hand, a numerical or analytical study of $m_{\hat{q},t}(x)$ is not feasible for a finite t. However in the limit $t \to \infty$ (keeping $\hat{q}$ fixed) we can use a *pruning*

procedure to obtain $\lim_{t\to\infty} m_{\hat{q},t}(x) = m_{\hat{q}}(x)$. The exact methodology and idea is described in C section 3. In practice, we construct a tree with $\hat{q}+1$ levels, where the first $\hat{q}$ levels have links threshold distributed as $\rho(\tau)$ while the last ones have thresholds distributed as the minimal energy of an infinite tree. Technically such minimal energy it is a divergent quantity we consider thresholds distributed as $\chi = \lim_{t\to\infty} \epsilon_0(t) - \overline{\epsilon_0(t)}$ which exists (see also C section 3). A pictorial representation of this modified tree is shown in figure 4.10.

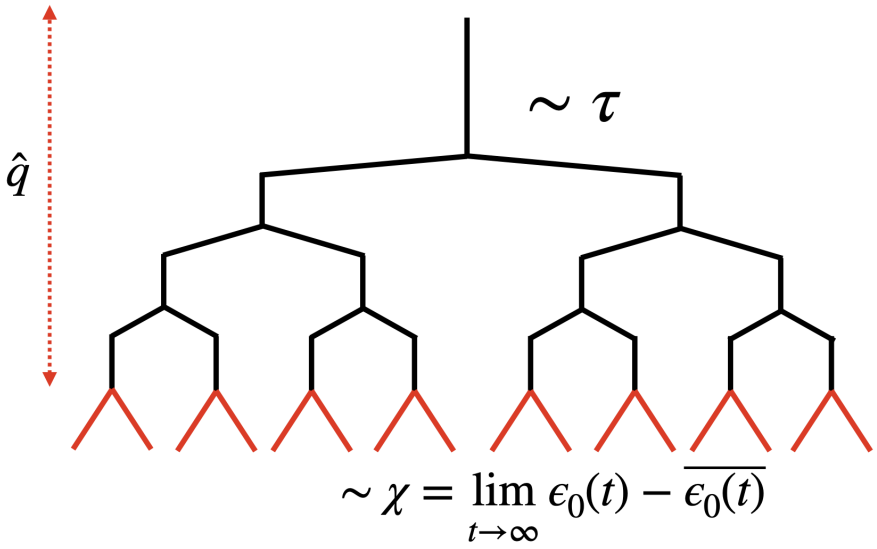

Figure 4.10: Example of the pruning procedure for $\hat{q} = 7$. The bottom links' thresholds are distributed according to the ground state energy of an infinite tree.

The methods introduce by [97] and reviewed in appendix C that are used to obtain 4.60 can be generalized for $m_{\hat{q}}(x)$ (see C section 3).
As the limit $t \to \infty$ is taken at fixed $\hat{q}$, the overlap $\hat{q}/t$ will vanish even if we take $\hat{q} \to \infty$. In this limit, we show numerically (see figure 4.11) that

$$\lim_{\hat{q}\to\infty} \overline{m_{\hat{q}}(x)} = e^{\beta_c x} \tag{4.61}$$

In the last section of appendix C, we give an analytical argument that proves 4.61. Intuitively, if we take paths with vanishing overlap their energies become uncorrelated and as such the sub-system of zero-overlap states behaves as a REM which has precisely the density of states of the form 4.61. So by the arguments given above about the opening pressures, for a large tree $t \to \infty$ the number of channels $n_{\mathrm{ch,t}}(x)$ flowing below a pressure $P = x + P_0$ identifies with the number of channels with vanishing overlap and low energy. Thus, on average:

$$\lim_{t\to\infty} \overline{n_{\mathrm{ch,t}}(x)} = \lim_{\hat{q}\to\infty} \overline{m_{\hat{q}}(x)} = e^{\beta_c x} \tag{4.62}$$

As the channels have vanishing overlap, they contribute to the flow independently. Each of them has an opening pressure $x' + P_0$, thus its contribution to the flow is $(P - (x' + P_0)_+)/t = (x - x')_+/t$ from which the average flow reads:

$$\lim_{t\to\infty} \overline{tQ_t(x)} = \int_0^x dx'(x - x') \lim_{t\to\infty} \frac{d}{dx'} \overline{n_{\mathrm{ch,t}}(x')} = \frac{e^{\beta_c x} - 1}{\beta_c} \tag{4.63}$$

to which the following permeability is associated:

$$\lim_{t\to\infty} \overline{t\kappa_t(x)} = \frac{d}{dx} \lim_{t\to\infty} \overline{tQ_t(x)} = e^{\beta_c x} \tag{4.64}$$

The expression for the flow 4.63 catches both the initial linear regime $Q_t(P) \sim \frac{P-P_0}{t}$ for $x \to 0$ and the non-linear one for larger x. At very high pressure the Newtonian regime takes over, where the permeability reaches its maximal value $\kappa_\infty = 1/2$ (see previous section) and the flow becomes again linear in P:

$$Q(P) = \kappa_\infty (P - P^*) \tag{4.65}$$

where $P^* \sim \bar{\tau} t$ corresponds to the average pressure at which all channels flow. The cross-over between the non-linear regime and the Newtonian linear one occurs when the permeability $\overline{\kappa_t(x)} \sim e^{\beta_c x}/t$ reaches the Netwonian value κ_∞ at $P_{\mathrm{sat}} = P_0 + x_{\mathrm{sat}}$:

$$x_{\mathrm{sat}} \sim \frac{1}{\beta_c} \ln t \tag{4.66}$$

As consequence, at P_{sat}, the number of flowing channels is $\sim t$. Let us comment on this result. When the pressure is slightly above the minimal value P_0, only a single channel is open and κ_t is $\sim 1/t$. Increasing the pressure slightly more ($\sim \ln t$) is enough to have the $\sim t$ channels with very small overlap flowing and consequently to reach the total permeability κ. Note that this number is very small compared to 2^{t-1}, the total number of directed paths. At very high pressure, the fluid flows indeed in more and more channels, but this does not affect much the permeability of the network. the flow cannot increase indefinitely and this can be seen in two equivalent ways. In the next section we test these predictions using extensive numerical simulations.

4.7 . Numerical results

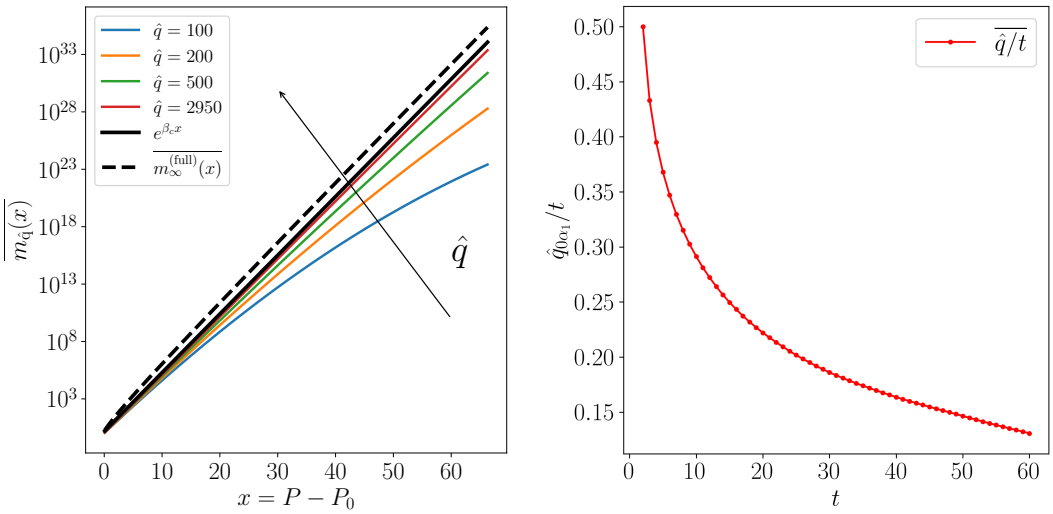

Figure 4.11: Left: Numerical study of $m_{\hat{q}}(x)$ and comparison with the prediction $e^{\beta_c x}$ and full density of states. Right: Monte Carlo simulation of the average (scaled) overlap between the ground state and the second channel i.e. $q = \hat{q}_{\alpha_1,0}$. As discussed, the first channels to flow present low overlap with the ground state and thus resulting in a sub-linear growth of $\hat{q}_{\alpha_1,0}$ with t.

We first test the limit of $\hat{q} \to \infty$ of $m_{\hat{q}}(x)$. By employing the KPP methods reported in appendix C, we numerically compare $m_{\hat{q}}(x)$ for increasing $\hat{q}$ with the standard density of states $m_t^{(\mathrm{full})}(x) \sim x e^{\beta_c x}$ and with the prediction $\lim_{\hat{q}\to\infty} m_{\hat{q}}(x) = e^{\beta_c x}$. The results are reported in figure 4.11 where we find perfect agreement in the large $\hat{q}$ limit.

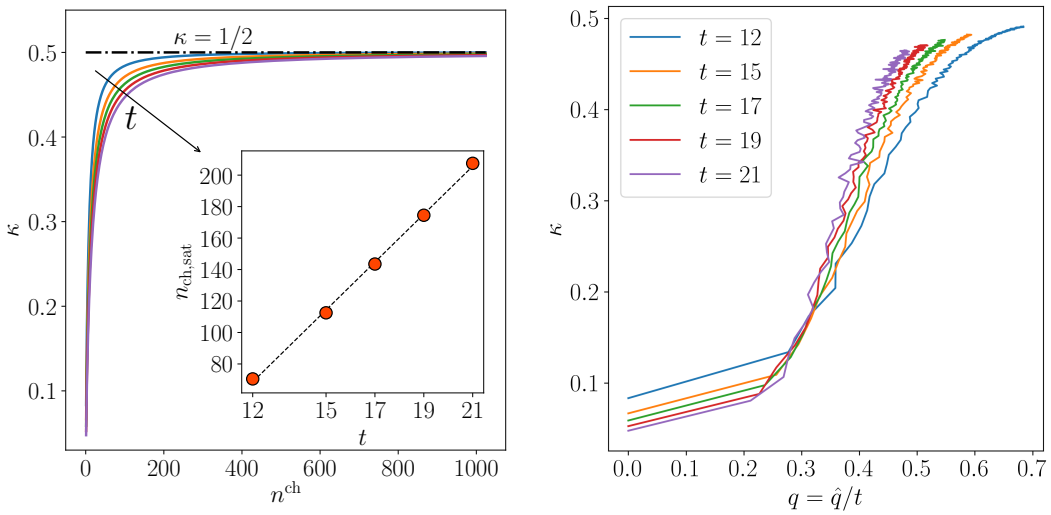

Figure 4.12: Left: permeability κ as a function of the number of flowing channels. Inset: average number of flowing channels needed to reach 95% of κ_∞ as a function of t. Right: permeability vs (scaled) maximal overlap. It is evident how low-overlapping channels dominate in the growth of permeability.

However, it is extremely challenging to probe directly the $t \to \infty$ as the number of channels in the system grow exponentially with the system size. In the figure reported here we limit ourselves to $t = 12, 15, 17, 19, 21$. The simulation of the system at a given t use the same algorithm as the two-dimensional case, where now a major simplification occurs, as the channels after separating do not cross anymore. Indeed the Djistrka part of the algorithm reduces to finding the minimal energy path from a the sub-tree originating a given node, which is particularly efficient in a tree structure. For a given realization of the disorder, between two opening pressures $P_k \leq P < P_{k+1}$ the flow is linear in P:

$$Q(P) = \kappa_k (P - P_k^*) \tag{4.67}$$

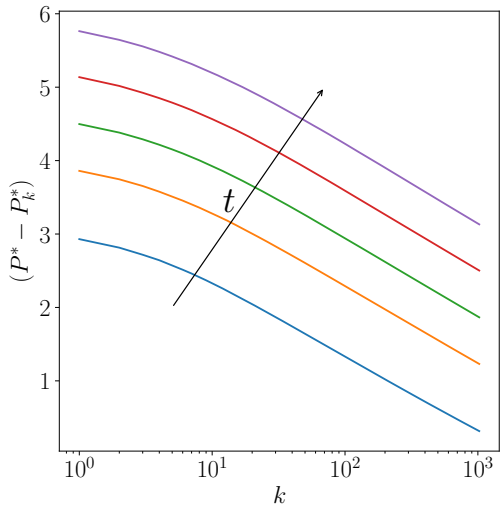

Figure 4.13: Distance of P_k^* to P^* (Netwonian pressure threshold). At variance with the permeability, the pressure P_k^* slowly approaches the Netwonian value. It is worth noticing that the rate, as a function of k, does not depend on t.

where κ_k is the permeability (precisely the one showed in figure 4.12 left) and P_k^* is a pressure threshold that ensures the continuity of the flow when a new channel opens. The various P_k^* can be obtained from the relation $\kappa_{k-1}(P_k - P_{k-1}^*) = \kappa_k(P_k - P_k^*)$. Since in the exact numerical simulation, we have access to both κ_k and P_k we can reconstruct the P_k^*. We then compare in figure 4.13 P_k^* to the pressure threshold $P^* \sim \bar{\tau}t$ relative to the Newtonian regime. What we find is that P_k^* approaches the Netwonian limit logarithmically in the number of flowing channels k: at variance with the permeability, this growth is extremely slow, which confirms an exponential growth of the flow in the system. Finally, to corroborate further the low-overlap bias of the Darcy problem, we performed simulations for larger t at the level of the second flowing channel, confirming the anticipated decay towards zero of $\hat{q}_{0,\alpha_1}$ as t grows. See figure 4.11 right.

4.8 . Conclusion and future work

In this chapter we discussed the disordered systems approach to the study of the Darcy's law of yield-stress fluids. Thanks to the mapping to the directed polymer in random media it is possible to study the the low pressure regime in the two dimensional case and to fully solve the system in the tree case. From the latter the importance of low-overlap states has emerged and thanks to the tools of the KPP equation we were able to fully study such states. It would be interesting to precisely understand the role of low-overlapping exictations in the finite dimensional case. In mean-field models exhibiting a glass transition the low energy low overlap excitations are abundant. However they usually are suppressed in finite dimension. On the otehr hand, the bias on the overlap induced by the flow problem does not depend on the system dimension and that is why we believe that the tree solution can give important insights on the flow of yield-stress fluids also in finite-dimensional porous media. Indeed, a prediction that should also hold there is the fast growth of κ_k and the slow growth of P_k^*.

Conclusion

In this thesis, we focused on three different approaches to the characterization of aftershocks. For the first one, we introduced a simple model of avalanches displaying correlations i.e. aftershocks. The model is based on a simple construction, that essentially, an avalanche releases a constant amount of stress each time the system fails, and the quenched disorder determines the total displacement. We managed to solve the model with a mixture of analytical and numerical techniques, showing the existence of a phase transition when the distribution of disorder is exponential. The presence of correlations is, on the other hand, independent of the disorder distribution. For future work, we look forward to completing the analysis of correlations (characterizing the maximum of the avalanche size in a sequence, for example) and extending the model to other types of disorders, such as a force landscape correlated as a random walk. In the second approach, we analyzed an experiment of an expansion of a domain wall in the creep regime. We showed how the domain expands in a correlated fashion, akin to mainshock-aftershocks group in earthquakes, and we characterized the statistics of such events confirming previous theoretical and numerical predictions for the first time. For further developments, it would be interesting to analyze similar experiments for field closer to the depinning one, where a first deviation from the creep law has been observed. Moreover, thanks to a collaboration with the experimentall group that carried out the experiments, we will use the techniques develop at this stage to compute the strength of the Dzyaloshinskii–Moriya interaction (DMI, responsible for magneto-electric effects in a material called multiferroics) with possible future applications to spintronics. The last chapter dedicated to aftershocks is the closest to the earthquakes phenoemon as it deals directly with their prediction starting from surface displacement data as measured by GPS stations. We showed how it is possible to handle this type of data and how to set up a prediction method, obtaining satisfying results for aftershocks prediction in Japan. While not overcoming the performances of catalog-driven methods, such the famous Epidemic-Type Aftershocks Sequence (ETAS) model, we were able to show that indeed GPS data carries information relevant to aftershocks prediction.

Thus a natural step would be to unify in one single method all the different types of independent seismic data - waveforms, GPS, past catalog - with the hope that their interplay could boost the overall performances and one source would compensate for the flaws of the other. Moreover, from a more descriptive point of view, it would be interesting to characterize the statistical properties of the slip maps measured by GPS data, relating them to the predictions given by the theory of interfaces in random media and its more earthquake-oriented variations. In spirit, while requiring more effort - knowledge of the seismic fault geometry and the associated propagation models - such an approach would transfer the type of analysis carried out for the domain walls to the fault dynamics.

As for the last chapter, dedicated to porous media, we solved a model of interacting channels by characterizing the flow rate and the associated increase in permeability by exploiting the relevance of channel overlap in the process. To this purpose, we adapted the methods of the KPP equation to the study of low overlap states in the directed polymer in random media on a tree and showed that an exact mapping exists between the Darcy and the polymer problem. For future developments, one straightforward extension would be to fully understand to which extent the results on the tree geometry generalize to the 2D and 3D cases, thus reconciling the overlap picture of yield stress fluids in porous media.

Résumé en français

Cette thèse vise à étudier les corrélations spatiales et temporelles des systèmes présentant des avalanches. En physique statistique, une avalanche est une réorganisation des degrés de liberté d'un système en réponse à une instabilité générée, telle que le changement de forces appliquées, les fluctuations thermiques ou le mécanisme de relation interne. L'étude de la dynamique des avalanches est aussi intéressante qu'ubiquitaire : les séismes sont des avalanches se produisant dans des failles sismiques [1–7], les avalanches caractérisent la déformation de structures cristallines soumises à une charge [8,9], elles sont des précurseurs de la rupture dans des matériaux fragiles [10], décrivent l'invasion de milieux poreux par un fluide [11,12] et émergent même dans l'activité neuronale [13]. Souvent, les avalanches présentent des propriétés de regroupement, à la fois dans le temps et dans l'espace : une avalanche principale se produit pouvant déclencher de nombreuses avalanches "filles" exhibant des structures statistiques riches. Un exemple phare et le principal sujet de cette thèse se trouve dans le binôme des chocs principaux et des répliques en sismologie. Caractériser la manière dont surviennent les répliques est d'une importance primordiale, tant pour des applications scientifiques que pratiques pour l'homme. En tant que tel, la partie principale du manuscrit est divisée en trois chapitres, chacun se référant à un traitement différent du sujet des répliques. Dans le premier chapitre, basé sur l'article publié [14], nous développons et résolvons exactement un modèle minimal d'avalanches présentant des répliques, générant des séquences similaires à celles observées dans les tremblements de terre réels. Ce modèle s'inspire des modèles de champ moyen d'avalanches, tels que le célèbre modèle ABBM [15], et est ancré dans la classe des particules dans des paysages désordonnés. En utilisant la statistique des valeurs extrêmes, nous montrons que ce modèle présente des avalanches avec une distribution de loi de puissance, que nous déterminons analytiquement. De plus, nous caractérisons analytiquement et numériquement les corrélations entre les avalanches, montrant que ce modèle est l'un des rares modèles solubles présentant des répliques. Lors de la modélisation des failles sismiques et des tremblements de terre en physique statistique, le paradigme des interfaces dans des milieux aléatoires

est souvent adopté. En termes simples, l'interface modélise la section de la faille sismique, et l'avalanche observée dans le modèle est interprétée comme des tremblements de terre. En pratique, le mouvement de l'interface est décrit par l'équation suivante $u(x,t)$:

$$\gamma \partial_t u(x,t) = c\nabla^2 u(x,t) + f + F(x, u(x,t))$$

où f est une force motrice, et $F(x, u(x,t))$ est un désordre figé provenant d'un potentiel $F(x,u) = -\partial_u V(x,u)$, modélisé comme une variable aléatoire gaussienne de moyenne nulle et de corrélation $\overline{V(x,u)V(x',u')} = \delta(x-x')\Delta(u-u')$. Il peut être démontré qu'à la force critique f_c, l'interface subit une transition de dépiégeage : en dessous de f_c, l'interface a une vitesse nulle dans la limite des grands t, tandis qu'elle acquiert une vitesse finie au-dessus de celle-ci. À $f = f_c$, le mouvement est intermittent, et $u(x,t)$ se réorganise en couvrant une zone S suivant une distribution à queues épaisses $P(S) \sim S^{-\tau}$. En interprétant une telle réorganisation comme un tremblement de terre, on mesurerait sa magnitude par $m = \frac{2}{3}\log_{10} S$, qui, par un simple changement de variable, serait distribuée de manière exponentielle $P(m) \sim 10^{-bm}$. Dans les tremblements de terre réels, une telle distribution de magnitude est effectivement observée et est appelée loi de Gutenberg-Richter [103]. Le modèle ABBM dont nous nous inspirons, comme mentionné précédemment, est une version de champ moyen de telles interfaces dans des milieux aléatoires au dépiégeage. Dans le deuxième chapitre, nous effectuons l'analyse des données de la dynamique d'une paroi de domaine s'étendant dans un film magnétique ultra-mince sous l'influence d'un petit champ magnétique. Le terme "creep" dans les matériaux magnétiques est emprunté à celui de la mécanique des solides, correspondant à l'accumulation lente mais progressive de la déformation de contrainte lors de l'application d'une contrainte externe (faible) sur une longue période. Ici, la déformation correspond à l'expansion de la paroi de domaine qui est entraînée par un petit champ magnétique externe. L'interaction entre la température, les impuretés présentes dans la structure cristalline du film sous-jacent et le champ magnétique d'entraînement donne lieu à une dynamique riche, dont la compréhension est extrêmement importante, par exemple, en spintronique. Nous encadrons le système dans la famille des interfaces entraînées dans des milieux aléatoires et nous testons les prédictions théoriques sur les données expérimentales.

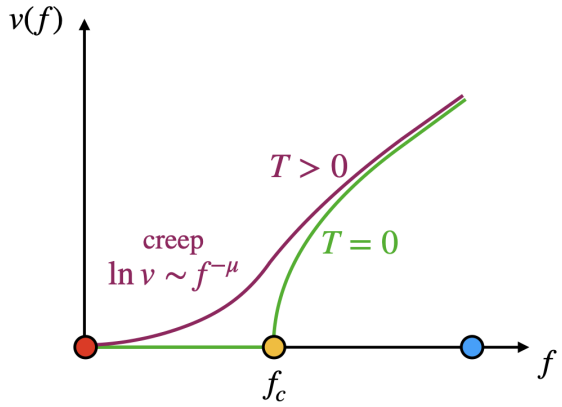

Figure 4.14: Caractéristiques de vitesse du régime de fluage (violet) comparées à la température zéro (vert). Au-dessus de la force critique f_c, l'effet de la température a tendance à diminuer et les statistiques de dépiégeage dominent.

En particulier, nous travaillons maintenant dans un contexte de température finie du modèle d'interface décrit ci-dessus

$$\gamma \partial_t u(x,t) = c\nabla^2 u(x,t) + f + F(x, u(x,t)) + \eta(x,t)$$

où $\langle \eta(x,t)\eta(x',t')\rangle = T\delta(x-x')\delta(t-t')$ est un désordre recuit modélisant une température finie. Le régime de fluage émerge pour des forces $f < f_c$ et les fluctuations thermiques permettent à l'interface d'avoir une vitesse finie v évoluant avec f comme $\ln v \sim f^{-\mu}$ avec $\mu = 1/4$, un exposant universel. Ce dernier est la célèbre loi de fluage et a été observé pour la première fois dans [54]. Nous montrons l'observation expérimentale de la présence de paires chocs principaux-répliques dans la dynamique d'avalanche de la paroi de domaine qui avait été prédite par la théorie [16] et observée récemment dans des simulations numériques [17].

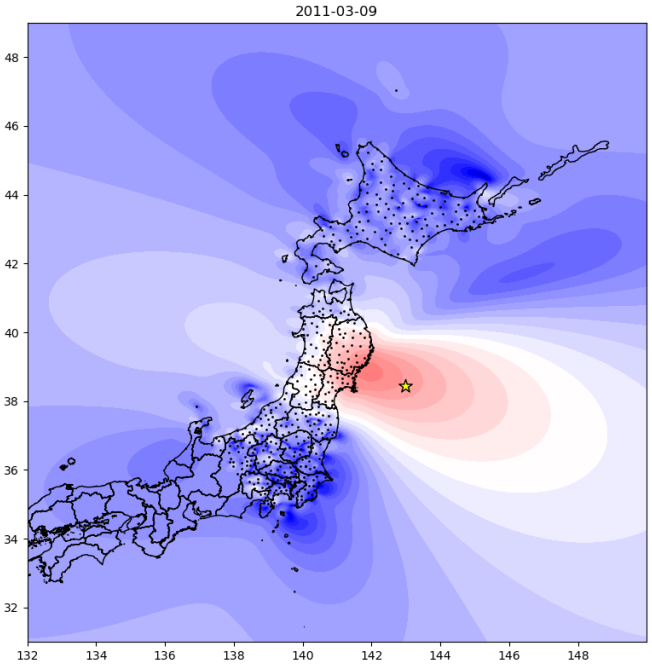

Figure 4.15: Logarithme de l'amplitude du déplacement interpolé tel que mesuré à la date du 9 mars 2011 au Japon, après le séisme précurseur de la séquence de Tohoku. Les points noirs correspondent aux positions réelles des stations.

Finalement, dans le troisième chapitre, nous explorons une nouvelle approche de la prévision des tremblements de terre, plus précisément dans la prédiction des répliques. Le point de départ est un travail récent [18] qui a exploité des cartes de déplacement souterrain reconstruites à la suite de grands tremblements de terre (séismes principaux) pour déduire les motifs spatiaux des répliques ultérieures en utilisant l'apprentissage automatique. Bien que très prometteuses, de telles cartes de déformation souterraine nécessitent une connaissance précise du système de failles et sont difficilement réalisables en temps réel ou presque en temps réel. Ici, nous explorons la possibilité d'utiliser des cartes de déplacement en surface sans connaissance préalable du système de failles pour atteindre le même objectif de prédiction de motifs. En particulier, de telles cartes de déplacement en surface peuvent être reconstruites plus facilement en utilisant des mesures de déplacement provenant de stations GPS au sol. Les stations GPS communiquent avec des satellites pour des mesures continues de leur position sur le sol, et une lecture satisfaisante peut être obtenue avec un délai de quelques heures, les rendant appropriées pour des prévisions quasi temps réel. Dans la pratique, nous abordons d'abord le problème de la construction de telles cartes. En effet, tandis que les mesures sont discrètes dans l'espace (au niveau des stations GPS), les répliques peuvent survenir partout dans l'espace, et nous devons donc extrapoler ces mesures discrètes à l'ensemble de l'espace. Nous

abordons ce problème en nous appuyant sur les méthodes de [79] qui décrivent une interpolation de mesures discrètes à la surface de la Terre, particulièrement adaptée aux données GPS. Après avoir construit les cartes, nous combinons les données GPS avec les données du catalogue contenant les emplacements des répliques en nous concentrant sur les données du jour d'un séisme principal et en associant les répliques survenues 45 jours après celui-ci. Nous visons à prédire les motifs spatiaux de ces répliques en utilisant une méthode statistique classique (régression logistique) et une approche d'apprentissage automatique plus moderne, en discutant à la fois de ses particularités et de ses limites.

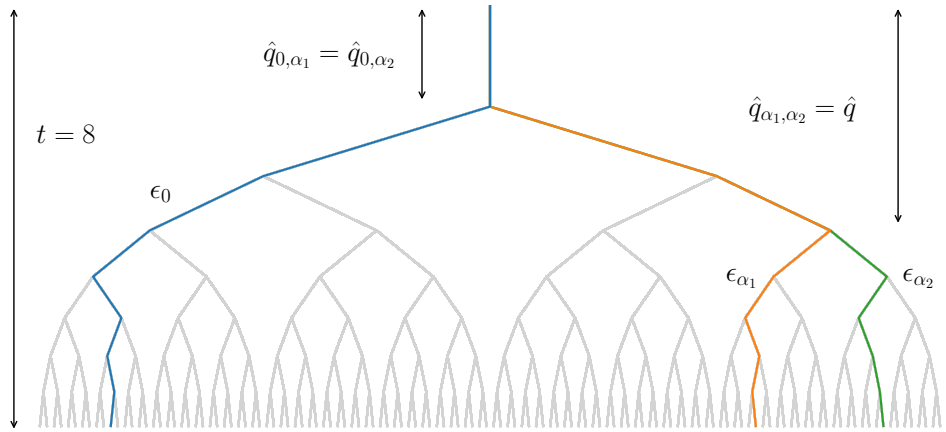

Figure 4.16: Exemple d'un arbre binaire avec $t = 8$ niveaux. Dans le cadre actuel, seuls trois canaux s'écoulent (bleu, orange, vert). Dans le chapitre, nous montrons que les canaux les plus susceptibles de s'écouler sont ceux ayant une faible overlap (nombre d'arêtes en commun) entre eux.

En tant qu'addendum, dans le dernier chapitre de cette thèse, nous étudions le problème de caractérisation de la loi de Darcy des fluides à seuil de contrainte non newtoniens. La loi de Darcy standard [19] est une loi linéaire décrivant les caractéristiques du débit par rapport à la pression d'un fluide newtonien dans un matériau poreux. Cependant, lorsque des fluides non newtoniens sont impliqués, tels que les fluides à seuil de contrainte, la loi de Darcy devient non linéaire en fonction de la pression appliquée. De nombreuses preuves numériques et expérimentales ont montré que dans de tels fluides, il existe un gradient de pression minimal en dessous duquel aucun écoulement macroscopique n'est observé. Un tel problème a été récemment étudié, par exemple, dans [89–92, 95] où une pression minimale de ce type a été caractérisée. Dans ce chapitre, nous utilisons les outils des systèmes désordonnés et de la physique statistique pour décrire l'écoulement en utilisant une

correspondance avec un problème bien connu et étudié, le polymère dirigé dans un milieu aléatoire. Nous résolvons analytiquement l'écoulement dans un modèle où le matériau poreux est modélisé comme un arbre binaire, où les chemins représentent les canaux par lesquels le flux peut se produire. Cette géométrie nous permet non seulement d'étudier la pression minimale, mais aussi de relier la non-linéarité de la loi de Darcy pour les fluides à seuil de contrainte à l'arrangement géométrique de la partie du système où le fluide circule à une pression donnée.

Appendix A

Mainshocks: test set

Table A.1: List of the 23 earthquakes employed for the test.

INDEX	CODE-NAME	DATE (UTC)	MAG	EPI.	NUM-STATS	CNN-ACC	LRB-ACC
1	Ofunato	2015-5-12	6.8	$38.86N$ $142.15E$	22	0.65	0.58
2	Shizunai	2016-1-14	6.7	$41.97N$ $142.80E$	11	0.39	0.50
3	Kumamoto	2016-4-15	7.3	$32.75N$ $130.76E$	58	0.70	0.65
4	Hualien1	2016-5-12	6.5	$24.66N$ $121.92E$	1	0.50	0.50
5	Yonakuni	2016-6-23	6.2	$23.50N$ $123.33E$	1	0.48	0.50
6	Kurayoshi	2016-10-21	6.6	$35.38N$ $133.86E$	41	0.88	0.92
7	Namie	2016-11-21	7.4	$37.35N$ $141.60E$	23	0.79	0.74
8	Daigo	2016-12-28	6.3	$36.72N$ $140.57E$	46	0.47	0.55
9	Hachinohe	2017-9-26	6.1	$40.27N$ $142.46E$	13	0.49	0.50
10	Misawa	2018-1-24	6.3	$41.01N$ $142.45E$	6	0.77	0.50
11	Hualien	2018-2-6	6.7	$24.09N$ $121.68E$	1	0.50	0.50
12	Matsue	2018-4-8	6.1	$35.18N$ $132.59E$	31	0.99	0.50
13	Osaka	2018-6-17	6.1	$34.84N$ $135.62E$	75	0.44	0.50
14	Chiba	2018-7-7	6.0	$35.17N$ $140.59E$	29	0.48	0.50
15	Chitose	2018-9-5	6.7	$42.69N$ $142.01E$	31	0.69	0.86
16	Hokkaido	2018-11-4	6.3	$44.61N$ $145.81E$	4	0.50	0.50
17	Nishinoomote	2019-1-8	6.0	$30.57N$ $131.16E$	15	0.50	0.48
18	Volcano Islands	2019-3-11	6.1	$25.67N$ $141.03E$	1	0.50	0.50
19	Hualien2	2019-4-18	6.5	$24.01N$ $121.51E$	2	0.50	0.50
20	Miyazaki	2019-5-9	6.3	$31.80N$ $131.97E$	20	0.48	0.50
21	Tsuruoka	2019-6-18	6.7	$38.61N$ $139.48E$	28	0.98	0.95
22	Namie	2019-8-4	6.4	$37.71N$ $141.63E$	25	0.50	0.50
23	Yilan	2019-8-7	6.4	$24.37N$ $121.87E$	3	0.88	0.50

Appendix B

Opening pressures for the first few channels

In this section we report the derivation of the expression for P_1 used in the chapter and we also derive P_2.

The fluid starts to flow only above the critical pressure $P_0 = \epsilon_0(t)$ and only along the channel that coincides with the ground state of the directed polymer:

$$Q_{0,t}(P) = \frac{P - P_0}{t} \tag{B.1}$$

The subscript 0 in Q indicates that flow is possible only along the ground state. Such a formula holds for $P > P_0$ and smaller than P_1, the pressure at which a second channel opens.

The two channels problem

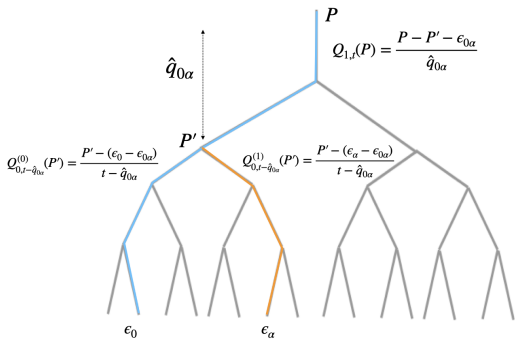

Figure B.1: Schematics for the tree with two open channels.

Here, flow is possible along two channels (see figure B.1): the ground state with energy ϵ_0, depicted in blue and a second channel with energy ϵ_α, depicted in orange.

These two channels have a common part of length $\hat{q}_{0\alpha}$; we denote with $\epsilon_{0\alpha}$ the sum of the thresholds along this common portion and P' the pressure at the bottom of the common part, hence the flow along it reads:

$$Q_{1,t}(P) = \frac{P - P' - \epsilon_{0\alpha}}{\hat{q}_{0\alpha}} \tag{B.2}$$

The pressure P' can be determined using the conservation of the flow:

$$\frac{P - P' - \epsilon_{0\alpha}}{\hat{q}_{0\alpha}} = Q^{(0)}_{0,t-\hat{q}_{0\alpha}}(P') + Q^{(1)}_{0,t-\hat{q}_{0\alpha}}(P') \tag{B.3}$$

where $Q^{(0)}_{0,t-\hat{q}_{0\alpha}}(P')$ is the flow along the subtree containing the ground state, $Q^{(1)}_{0,t-\hat{q}_{0\alpha}}(P')$ containing the other channel (see the two branches of figure B.1). Since each of these is a single channel of length $t - \hat{q}_{0\alpha}$, we can use once again Eq. (B.1). One has

$$Q^{(0)}_{0,t-\hat{q}_{01}}(P') = \frac{P' - (\epsilon_0 - \epsilon_{0\alpha})}{t - \hat{q}_{0\alpha}} \ , \qquad Q^{(1)}_{0,t-\hat{q}_{0\alpha}}(P') = \frac{P' - (\epsilon_\alpha - \epsilon_{0\alpha})}{t - \hat{q}_{0\alpha}} \tag{B.4}$$

From equation (B.3) we derive first the expression for $P'(P)$ and then $Q_{1,t}(P)$:

$$P'(P) = \frac{\hat{q}_{0\alpha}(\epsilon_0 + \epsilon_\alpha) + (t - \hat{q}_{0\alpha})P}{t + \hat{q}_{0\alpha}} - \epsilon_{0\alpha} \ , \qquad Q_{1,t}(P) = \frac{2}{t + \hat{q}_{0\alpha}} \left(P - \frac{\epsilon_0 + \epsilon_\alpha}{2} \right) \tag{B.5}$$

We can now determine the pressure $\tilde{P}_1$ such that $Q_{0,t}(\tilde{P}_1) = Q_{1,t}(\tilde{P}_1)$, namely

$$\tilde{P}_1 = \epsilon_0 + \frac{t}{t - \hat{q}_{0\alpha}}(\epsilon_\alpha - \epsilon_0) \tag{B.6}$$

For pressure $P \in (P_0, \tilde{P}_1)$ we have $Q_{0,t}(\tilde{P}_1) > Q_{1,t}(\tilde{P}_1)$, this means that the fluid cannot flow in the second channel and the flow rate is given by $Q_{0,t}(P)$. Above $\tilde{P}_1$ the second channel is open and the flow rate is given by $Q_{1,t}(\tilde{P}_1)$. The criterion to select the first excited channel that opens above P_0, is that the pressure P_1 is the smallest among all the $\tilde{P}_1$ computed for all possible two-channel geometries. This translates into

$$P_1 = \min_{\tilde{P}_1} \tilde{P}_1 = \epsilon_0 + \min_{\alpha \neq 0} \frac{t}{t - \hat{q}_{0\alpha}}(\epsilon_\alpha - \epsilon_0) \tag{B.7}$$

The channel satisfying the minimum condition is denoted by α_1. Notice that the equation for P_1 B.7 remains the same for the tree and the 2d geometries.

The three channels problem

There are three possible configurations for the position of the second excited channel with respect to the ground state and the first one. They each lead to a slightly different expression for the pressure P_2, but all simplify to $P_2 = \epsilon_{\alpha_2}$ in the limit $t \to \infty$.

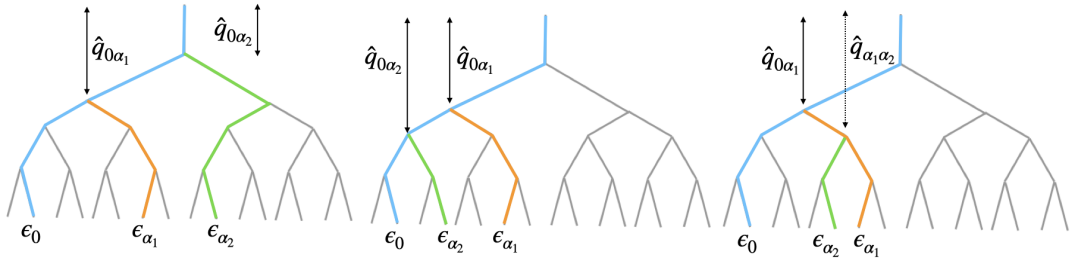

Figure B.2: Schematics for the Cayley tree with three open channels in the three possible geometrical arrangements.

The first case is the simplest: the second channel opens with a common overlap $\hat{q}_{0\alpha_2} = \hat{q}_{\alpha_1\alpha_2}$ with the ground state and the first channel. See figure B.2 left. By construction, $\hat{q}_{0\alpha_2} < \hat{q}_{0\alpha_1}$.
The pressure P_2 reads:

$$P_2 = \min_{\alpha_2 \neq \{\alpha_1, 0\}} \left[\epsilon_{\alpha_2} - \frac{\hat{q}_{0\alpha_2}}{t + \hat{q}_{0\alpha_1} - 2\hat{q}_{0\alpha_2}} (\epsilon_{\alpha_1} + \epsilon_0 - 2\epsilon_{\alpha_2}) \right] \tag{B.8}$$

In the limit $t \to \infty$, we saw that $\hat{q}_{0\alpha_1} = O(1)$; from this and $\hat{q}_{0\alpha_2} < \hat{q}_{0\alpha_1}$, it follows that $\hat{q}_{0\alpha_2} = O(1)$ and $P_2 = \epsilon_{\alpha_2}$.

The second case corresponds to the opening of the second excited channel from the ground state with an overlap $\hat{q}_{0\alpha_2} > \hat{q}_{\alpha_1\alpha_2} = \hat{q}_{0\alpha_1}$. See figure B.2 middle. The pressure P_2 reads:

$$P_2 = \epsilon_0 - \frac{\hat{q}_{0\alpha_1}}{t - \hat{q}_{0\alpha_1}} (\epsilon_{\alpha_1} - \epsilon_0) + \min_{\alpha_2 \neq \{\alpha_1, 0\}} \frac{t + \hat{q}_{0\alpha_1}}{t - \hat{q}_{0\alpha_2}} (\epsilon_{\alpha_2} - \epsilon_0) \tag{B.9}$$

When $t \to \infty$, the previous argument for the first excited channel sets $\hat{q}_{0\alpha_1}/t \approx 0$. In this limit, the resulting expression for P_2 is:

$$P_2 = \epsilon_0 + \min_{\alpha_2 \neq \{\alpha_1, 0\}} \frac{t}{t - \hat{q}_{0\alpha_2}} (\epsilon_{\alpha_2} - \epsilon_0) \qquad \text{when } t \to \infty \tag{B.10}$$

This expression is identical to equation (B.7) with the substitution $\alpha \to \alpha_2$, and applying the same arguments of the first channel we arrive at setting $\hat{q}_{0\alpha_2}/t \approx 0$, leading $P_2 = \epsilon_{\alpha_2}$.

The last case is the mirror of the previous one, with the second channels that opens from the first one with overlap $\hat{q}_{\alpha_1\alpha_2} > \hat{q}_{0\alpha_1} = \hat{q}_{0\alpha_2}$. See figure B.2 right. The pressure P_2 reads:

$$P_2 = \epsilon_0 + \frac{t}{t - \hat{q}_{0\alpha_1}} (\epsilon_{\alpha_1} - \epsilon_0) + \min_{\alpha_2 \neq \{\alpha_1, 0\}} \frac{t + \hat{q}_{0\alpha_1}}{t - \hat{q}_{\alpha_1\alpha_2}} (\epsilon_{\alpha_2} - \epsilon_{\alpha_1}) \tag{B.11}$$

When $t \to \infty$, the previous argument for the first excited channel sets $\hat{q}_{0\alpha_1}/t \approx 0$. In this limit, the resulting expression for P_2 is:

$$P_2 = \epsilon_1 + \min_{\alpha_2 \neq \{\alpha_1, 0\}} \frac{t}{t - \hat{q}_{\alpha_1\alpha_2}} (\epsilon_{\alpha_2} - \epsilon_{\alpha_1}) \qquad \text{when } t \to \infty \tag{B.12}$$

This expression is again similar to equation (B.7) and applying the same arguments of the first channel we arrive at setting $\hat{q}_{\alpha_1\alpha_2}/t \approx 0$, leading $P_2 = \epsilon_{\alpha_2}$.

Appendix C

Discrete KPP equation

In this appendix we give a complete summary for the techniques used for the study of the Darcy flow in a tree that employ the discrete KPP equation

C.1 . The equation

The discrete KPP equation has the general form:

$$G_{t+1}(x) = \int d\tau \rho(\tau) G_t(x-\tau)^2 \tag{C.1}$$

where $\rho(\tau)$ is a probability distribution and the initial condition on $G_t(x)$ is given by a function $g(x)$ i.e. $G_0(x) = g(x)$. By labelling the (ordered) energies of the directed polymer as $\epsilon_\alpha(t)$ with $\alpha = 0 \dots 2^{t-1} - 1$, we can show if $G_t(x)$ has the following multiplicative form

$$G_t(x) = \overline{\prod_\alpha g(x - \epsilon_\alpha(t))} \tag{C.2}$$

it satisfies (C.1). Indeed a tree of $t+1$ levels can be constructed from two trees of t levels that we combined together by adding an edge like as in figure C.1.

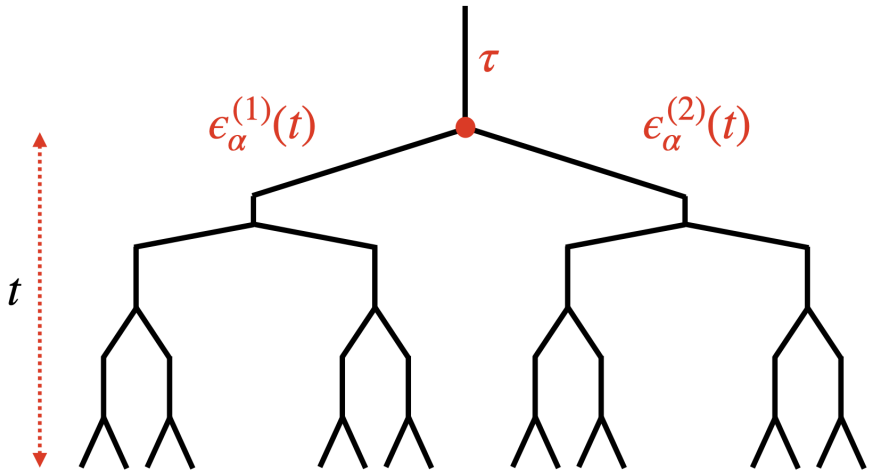

Figure C.1: Caption

The energies $\epsilon_\alpha(t+1)$ are constructed by summing the new edge energy τ to any other energy coming from either of the two subtrees. Hence:

$$G_{t+1}(x) = \overline{\prod_{\alpha=0}^{2^t-1} g(x-\epsilon_\alpha(t+1))} = \tag{C.3}$$

$$= \int d\tau\rho(\tau) \overline{\prod_{\alpha=0}^{2^{t-1}-1} g(x-\tau-\epsilon_\alpha^{(1)}(t))} \quad \overline{\prod_{\alpha=0}^{2^{t-1}-1} g(x-\tau-\epsilon_\alpha^{(2)}(t))} = \tag{C.4}$$

$$= \int d\tau\rho(\tau) G_t^2(x-\tau) \tag{C.5}$$

The overline, which stands for the average over the energies, can be split by explicitiing first the edge energy τ and using the fact the the two subtrees of t levels have independent energies. Different choiches for the initial condition $G_0(x) = g(x)$ correspond to different type of statistics over the energies. One general result holds, as proven by [104]. If $g(x) \to 0$ for $x \to \infty$ and $g(x) \to 1$ for $x \to -\infty$, $G_t(x)$ becomes for large t a travelling wave form with negative velocity i.e. $G_t(x) = w(x+ct)$. where c depends on $g(x)$.

C.2 . Ground state energy

To study the minimal energy $\epsilon_0(t)$ (the ground state) that correspond to the critical pressure P_0 in the case of a yield stress fluid on the tree, we can make use of the following initial condition dependent on a parameter β:

$$g_\beta(x) = \exp(-e^{\beta x}) \tag{C.6}$$

In this section we will use instead of $G_t(x)$ the label $\Omega_t(x;\beta)$. Hence $\Omega_0(x;\beta) = g_\beta(x)$. This choice corresponds to to the study of the cumulant generating function of the partition function associated to the directed polymer, when interpreted as a random energy model:

$$Z_{\mathrm{DP,t}}(\beta) = \sum_\alpha e^{-\beta\epsilon_\alpha(t)} \tag{C.7}$$

Indeed:

$$\overline{\sum_{n=0}^{\infty}(-1)^n\frac{(e^{\beta x}Z_{\mathrm{DP,t}}(\beta))^n}{n!}} = \overline{\exp(-e^{\beta x}Z_{\mathrm{DP,t}}(\beta))} = \overline{\prod_\alpha \exp(-e^{\beta(x-\epsilon_\alpha(t))})} = \overline{\prod_\alpha g_\beta(x-\epsilon_\alpha(t))} \tag{C.8}$$

When interested in the ground state energy taking the limit $\beta \to \infty$ corresponds to:

$$\lim_{\beta\to\infty} g_\beta(x) = \theta(-x) \tag{C.9}$$

which for $\Omega_t(x;\beta)$ means:

$$\overline{\prod_\alpha \theta(\epsilon_\alpha(t)-x)} = \overline{\theta(\epsilon_0(t)-x)} \tag{C.10}$$

which corresponds to the inverse cumulative distribution of $\epsilon_0(t)$, namely the probability $\mathbb{P}[\epsilon_0(t) \geq x]$. We can now start by analyzing the discrete KPP equation with the initial condition $g_\beta(x)$. We start by studying the left tail, namely the limit $x \to -\infty$ and we do so by linearizing (C.1) using a travelling wave ansatz with velocity $-c$:

$$\omega_t(x;\beta) \approx 1 - e^{\beta(x+ct)} \quad x \to -\infty \tag{C.11}$$

By plugging this form into (C.1) we get a consistency condition on c

$$1 - \epsilon^{\beta(\epsilon+c(t+1))} = \int \rho(\tau)(1-2\epsilon^{\beta(\epsilon-\tau+ct)}) \tag{C.12}$$

that translates to

$$c(\beta) = \frac{1}{\beta}\log\left(2\int d\tau\rho(\tau)e^{-\beta\tau}\right) \tag{C.13}$$

It can be shown [97, 104] that the travelling wave velocity *freezes* at a value β_c that corresponds to the minimum of $c(\beta)$:

$$\beta_c = \arg\min_\beta c(\beta) \tag{C.14}$$

Namely that:

$$c(\beta) = \begin{cases} c(\beta) & \beta < \beta_c \\ c(\beta_c) & \beta \geq \beta_c \end{cases} \tag{C.15}$$

In other words, the travelling wave solution exists only above a minimal velocity $c(\beta_c)$. This freezing phenomenon has been extensively observed in other systems, for example in the Derrida's random energy model and generally in spin glasses. Thus the typical value for the minimal energy is given by, at leading order

$$\overline{\epsilon_0(t)} = -c(\beta_c)t + O(t) \tag{C.16}$$

However important logarithmic corrections are present. They have been obtained by the discrete KPP equation in [99] (see [97, 104] for the continuum version) and they read:

$$\overline{\epsilon_0(t)} = -c(\beta_c)t + \frac{3}{2\beta_c}\ln t + O(1) \tag{C.17}$$

The fluctuations of the minimum around the typical value $\overline{\epsilon_0(t)}$ are given by the travelling front solution $w_{\min}(x)$ that satifsies the fixed point of (C.1) :

$$w_{\min}(x + c(\beta_c)) = \int d\tau \rho(\tau) w_{\min}^2(x - \tau) \tag{C.18}$$

More precisely, the fluctuations χ have a distribution $-w'(\chi)$ in the large t limit. In the following section we will denote with $\Omega_t(x)$ the solution of the KPP equation $\Omega_t(x;\beta)$ when $\beta \geq \beta_c$.

C.3 . Density of states above the minimum

Using the KPP formalism we can also study the average density of states:

$$\overline{n_t(x)} = \overline{\sum_\alpha \theta(x - \epsilon_\alpha(t))} \tag{C.19}$$

and and the average density of states above the minimum:

$$\overline{m_t^{(\text{full})}(x)} = \overline{\sum_\alpha \theta(x + \epsilon_0(t) - \epsilon_\alpha(t))} \tag{C.20}$$

For this we are gonna follow the techniques presented in [101] and summarized in [...]. The quantity $n_t(x)$ does not have a well define limit as $\epsilon_0(t)$ diverges with t. On the other hand $\overline{m_t^{(\text{full})}(x)}$ for $x \sim O(1)$ has a well defined form as shown in [101]:

$$\lim_{t\to\infty} \overline{m_t^{(\text{full})}(x)} = Axe^{\beta_c x} \quad x \sim O(1) \tag{C.21}$$

with A an unknown constant of order one. Let's start by considering the following multiplicative function of the energies:

$$\chi_t(x;\lambda) = \overline{\lambda^{m_t^{(\text{full})}(x)}} \tag{C.22}$$

It can be rewritten using the following identity:

$$\chi_t(x;\lambda) = \int dx' \overline{\lambda^{n_t(x+x')}\delta(x'-\epsilon_0(t))} = 1 + \partial_x \int dx' \overline{\lambda^{n_t(x+x')}\theta(\epsilon_0(t)-x')} \quad \text{(C.23)}$$

By using the definition of $n_t(x)$:

$$\chi_t(x;\lambda) = 1 + \partial_x \int dx' \prod_\alpha \lambda^{\theta(x+x'-\epsilon_\alpha(t))}\theta(\epsilon_\alpha(t)-x') \quad \text{(C.24)}$$

The inner part of the integral corresponds to a multiplicative function (in the variable x') of the energies with initial condition $g(x';x,\lambda) = \lambda^{\theta(x+x')}\theta(-x')$. Now we can use $\chi(x;\lambda)$ to study $\overline{m_t^{(\text{full})}(x)}$ as we can take a derivative w.r.t λ:

$$\overline{m_t^{(\text{full})}(x)} = \partial_\lambda \chi(x;\lambda)|_{\lambda=1} \quad \text{(C.25)}$$

Expanding thus $\lambda = 1-\varepsilon$ for small ϵ we get:

$$\overline{\lambda^{n_t(x+x')}\theta(\epsilon_0(t)-x')} = \Omega_t(x') - \varepsilon R_t(x';x) + O(\varepsilon^2) \quad \text{(C.26)}$$

with:

$$R_{t+1}(x';x) = 2\int d\tau\ \rho(\tau)\Omega_t(x'-\tau)R_t(x'-\tau;x) \quad \text{(C.27)}$$

and initial condition $R_0(x';x) = \theta(x'+x)\theta(-x')$. By using $R_t(x';x)$ we can thus obtain $\overline{m_t^{(\text{full})}(x)}$:

$$\overline{m_t^{(\text{full})}(x)} = \int dx'\ \partial_z R_t(x';x) \equiv \int dx'\ r_t(x';x) \quad \text{(C.28)}$$

Moreover because of the linearity of (C.27), $r_t(x';x)$ satisfies

$$r_{t+1}(x';x) = 2\int d\tau\ \rho(\tau)\Omega_t(x'-\tau)r_t(x'-\tau;x) = 2\int dy\ \rho(x'-y)\Omega_t(y)r_t(y;x) \quad \text{(C.29)}$$

with $r_0(x';x) = \delta(x'+x)$. As in [101], we can numerically solve equation (C.29) together with the solution of $\Omega_t(x)$ and numerically integrate $r_t(x';x)$.

C.4 . Density of states above the minimum with maximal overlap

Another important quantity that can be studied using the KPP formalism is the average density of states above minimum with the constraint that the overlap among these states is at most $\hat{q}$. We denote this quantity by $m_{\hat{q},t}(x)$. The physical picture is the one in figure [...].$m_{\hat{q},t}(x)$ is hard to study when t is finite. However in

the $t \to \infty$ limit, to study $\lim_{t\to\infty} m_{\hat{q},t}(x) = m_{\hat{q}}(x)$, we can use a *pruning* procedure (illustrated first in [...]). At the level $\hat{q}$ of the full tree, there are $2^{\hat{q}}$ subtrees labelled by $a = 0, \dots, 2^{\hat{q}} - 1$. We replace each of these subtrees with a single edge with a minimum energy $\epsilon_0^{(a)}$. This way we obtain a tree of $\hat{q}$ levels containing the $2^{\hat{q}}$ low energies paths with maximal overlap $\hat{q}$. This procedure is equivalent to growing a tree with $\hat{q}$ levels where the leaves thresholds are drawn from the distribution of the minimum of an infinite tree. Technically in the limit $t \to \infty$ the subtrees thresholds all diverge, we can subtract the deterministic part $\overline{\epsilon_0(t)}$ from each of the pruned trees, leaving a distribution for such new edges precisely $-w'_{\min}(x)$. The structure for the computation of $m_{\hat{q},t}(x)$ is the same as the $m_t^{(\text{full})}(x)$ and we do not carry out again. In summary:

$$\overline{m_{\hat{q}}(x)} = \int dx' \tilde{r}_{\hat{q}}(x'; x) \tag{C.30}$$

$$\tilde{\Omega}_{\hat{q}+1}(x) = \int d\tau \rho(\tau) \tilde{\Omega}^2_{\hat{q}}(x - \tau) \qquad \tilde{\Omega}_{\hat{q}=0}(x) = w_{\min}(x) \tag{C.31}$$

$$\implies \tilde{\Omega}_{\hat{q}}(x) = w_{\min}(x + c(\beta_c)\hat{q}) \tag{C.32}$$

$$\tilde{r}_{\hat{q}+1}(x'; x) = 2 \int d\tau \ \rho(\tau) \tilde{\Omega}_{\hat{q}}(x' - \tau) \tilde{r}_{\hat{q}}(x' - \tau; x) \qquad \tilde{r}_{\hat{q}=0}(x'; x) = -w'_{\min}(x + x') \tag{C.33}$$

C.5 . Large $\hat{q}$ limit of maximal overlap energy levels

In this section we present an analytical argument for the convergence at large-$\hat{q}$ of $m_{\hat{q}}(x)$ to $e^{\beta_c x}$. We start by introducing the shifted quantity $r_{\hat{q}}^{(s)}(x'; x) = r_{\hat{q}}(x' - c(\beta_c)\hat{q}; x)$ in the last equation of C.33. It becomes:

$$r_{\hat{q}+1}^{(s)}(x'; x) = 2 \int d\tau \ \rho(\tau) w_{\min}(x' - \tau - c(\beta_c)) r_{\hat{q}}^{(s)}(x' - \tau - c(\beta_c); x) = \int dx'' \mathcal{L}(x', x'') r_{\hat{q}}^{(s)}(x''; x) \tag{C.34}$$

where in the last equality we changed the integration variable setting $x'' = x' - \tau - c(\beta_c)$ and implicitly defined the linear operator $\mathcal{L}$. Thus, one can pass from $\hat{q} \to \hat{q} + 1$ by applying a fixed matrix $\mathcal{L}(x', x'')$[1]. Since the matrix $\mathcal{L}$ is independent of $\hat{q}$, iterating this equation $\hat{q}$ times, we can express $r_{\hat{q}}^{(s)}$ in terms of the initial condition at $\hat{q} = 0$

$$r_{\hat{q}}^{(s)}(x'; x) = \int dx'' \mathcal{L}^{\hat{q}}(x', x'') r_0^{(s)}(x''; x) = -\int dx'' \mathcal{L}^{\hat{q}}(x', x'') w'_{\min}(x'' + x) \tag{C.35}$$

where we denoted as $\mathcal{L}^{\hat{q}}$ the $\hat{q}$-th matrix power of $\mathcal{L}$ and in the last equality we used C.33 . In the limit $\hat{q} \to \infty$, $\mathcal{L}$ acts as a projector on the eigenspace with largest

[1]We use the expression *matrix*, although compact linear operator would be more appropriate in the mathematical jargon.

eigenvalues. Taking the derivative of Eq. (C.18) with respect to x', we obtain

$$w'_{\min}(x') = \int dx'' \mathcal{L}(x', x'') w'_{\min}(x'') \ . \tag{C.36}$$

which shows that $w'_{\min}(x')$ is an eigenvector with eigenvalue 1. We also have $-w'_{\min}(x') > 0$, as it corresponds to the probability density of the minimum. Since $\mathcal{L}(x', x'') > 0$, Perron-Frobenius theorem ensures that it corresponds to the largest eigenvalues which equals 1. Therefore, without further knowledge of the full spectrum of $\mathcal{L}$, we know that the remaining eigenvectors lie inside the unit circle. We can thus expand the initial condition on the eigenvectors as

$$r_0^{(s)}(x'; x) \equiv -w'_{\min}(x' + x) = -A(x) w'_{\min}(x') + R(x'; x) \tag{C.37}$$

where the first term contains the components on the leading eigenvector and $R(x'; x)$ stays for the remainder. The repeated application of $\mathcal{L}$ projects on $w'_{\min}(x')$ and thus

$$\lim_{\hat{q}\to\infty} r_{\hat{q}}^{(s)}(x'; x) = -A(x) w'_{\min}(x') \quad \Rightarrow \quad \lim_{\hat{q}\to\infty} m_{\hat{q}}(x) = -A(x) \int dx' w'_{\min}(x') = A(x) \tag{C.38}$$

where we used C.33 and in the last equality we performed the integration over x' using that $-w'_{\min}(x')$ is a normalised probability density. Thus, the large$-\hat{q}$ asymptotic behavior $m_{\hat{q}}(x)$ is given by the coefficient $A(x)$ in (C.37). However, since the operator $\mathcal{L}$ is not self-adjoint, in order to compute the projector on the eigenvector in (C.36), we need to determine the left eigenvector $\ell_{\min}(x')$ corresponding to $w'_{\min}(x')$, which satisfies

$$\int dx' \ell_{\min}(x') R(x'; x) = 0 \ , \qquad \int dx' \ell_{\min}(x') w'_{\min}(x') \neq 0 \ . \tag{C.39}$$

so that we can express the coefficient $A(x)$ as

$$A(x) = \frac{\int dx' \ell_{\min}(x') w'_{\min}(x' + x)}{\int dx' \ell_{\min}(x') w'_{\min}(x')} \tag{C.40}$$

Computing the adjoint of $\mathcal{L}$, we see that $\ell_{\min}(x')$ must satisfy

$$\ell_{\min}(x') = 2 w_{\min}(x') \int dx'' \ \ell_{\min}(x'') p(x'' - x' - c(\beta_c)) \tag{C.41}$$

The explicit form of $\ell_{\min}(x)$ cannot be determined in general as it depends on the specific form of the threshold distribution $p(\tau)$. So, it might look surprising that eventually the large $\hat{q}$ drastically simplify to a universal form, but a subtle mechanism is at play. Indeed, in the limit $x' \to -\infty$, we assume $\ell_{\min}(x') \sim e^{-\tilde{\beta} x'}$. Plugging

it in Eq. (C.41) and using that $w_{\min}(x \to -\infty) = 1$, we can determine the value of $\tilde{\beta}$. We obtain

$$2 \int dx' \, e^{-\tilde{\beta} x'} p(x' - x - c(\beta_c)) = e^{-\tilde{\beta} x} \tag{C.42}$$

and after the change of variables $\tau = x' - x - c(\beta_c)$, it coincides with equation (C.13) with $\tilde{\beta} = \beta_c$. Since $w'_{\min}(x') \overset{x' \to -\infty}{\longrightarrow} x' e^{\beta_c x'}$, we see that both the numerator and denominator in Eq. (C.40) are formally infinite as the integrand diverges for $x' \to -\infty$. So the ratio in Eq. (C.40) needs to be evaluated by a limiting procedure. In order to regularize we introduce a cutoff Λ on the left tail, replacing $\ell_{\min}(x) \to \vartheta(x + \Lambda)\ell_{\min}(x)$, so that the result should be recovered in the limit $\Lambda \to \infty$. Then, we have

$$\lim_{\hat{q} \to \infty} m_{\hat{q}}(x) \equiv A(x) = \lim_{\Lambda \to \infty} \frac{\int_{-\Lambda}^{\infty} dx' \, \ell_{\min}(x') w'_{\min}(x + x')}{\int_{-\Lambda}^{\infty} dx' \, \ell_{\min}(x') w'_{\min}(x')} = \lim_{\Lambda \to \infty} \frac{e^{\beta_c x} \int_{-\Lambda}^{0} dx \, (x' + x) + O(1)}{\int_{-\Lambda}^{0} dx' \, x' + O(1)} = e^{\beta_c x} \tag{C.43}$$

which gives the expected exponential behavior.

Bibliography

[1] S. Lise and M. Paczuski, "Self-organized criticality and universality in a nonconservative earthquake model," *Phys. Rev. E*, vol. 63, p. 036111, Feb 2001.

[2] S. Lise and M. Paczuski, "Scaling in a nonconservative earthquake model of self-organized criticality," *Phys. Rev. E*, vol. 64, p. 046111, Sep 2001.

[3] Z. Olami, H. J. S. Feder, and K. Christensen, "Self-organized criticality in a continuous, nonconservative cellular automaton modeling earthquakes," *Phys. Rev. Lett.*, vol. 68, pp. 1244–1247, Feb 1992.

[4] F. P. Landes and E. Lippiello, "Scaling laws in earthquake occurrence: Disorder, viscosity, and finite size effects in olami-feder-christensen models," *Physical Review E*, vol. 93, May 2016.

[5] C. H. Scholz, *The mechanics of earthquakes and faulting*. Cambridge university press, 2019.

[6] E. Lippiello, G. Petrillo, F. Landes, and A. Rosso, "Fault heterogeneity and the connection between aftershocks and afterslip," *Bulletin of the Seismological Society of America*, vol. 109, pp. 1156–1163, Apr. 2019.

[7] G. Petrillo, E. Lippiello, F. P. Landes, and A. Rosso, "The influence of the brittle-ductile transition zone on aftershock and foreshock occurrence," *Nature Communications*, vol. 11, June 2020.

[8] T. Richeton, J. Weiss, and F. Louchet, "Breakdown of avalanche critical behaviour in polycrystalline plasticity," *Nature Materials*, vol. 4, pp. 465–469, May 2005.

[9] T. RICHETON, J. WEISS, and F. LOUCHET, "Dislocation avalanches: Role of temperature, grain size and strain hardening," *Acta Materialia*, vol. 53, pp. 4463–4471, Sept. 2005.

[10] A. Shekhawat, S. Zapperi, and J. P. Sethna, "From damage percolation to crack nucleation through finite size criticality," *Phys. Rev. Lett.*, vol. 110, p. 185505, Apr 2013.

[11] M. Cieplak and M. O. Robbins, "Dynamical transition in quasistatic fluid invasion in porous media," *Phys. Rev. Lett.*, vol. 60, pp. 2042–2045, May 1988.

[12] R. Planet, S. Santucci, and J. Ortín, "Avalanches and non-gaussian fluctuations of the global velocity of imbibition fronts," *Phys. Rev. Lett.*, vol. 102, p. 094502, Mar 2009.

[13] N. Friedman, S. Ito, B. A. W. Brinkman, M. Shimono, R. E. L. DeVille, K. A. Dahmen, J. M. Beggs, and T. C. Butler, "Universal critical dynamics in high resolution neuronal avalanche data," *Phys. Rev. Lett.*, vol. 108, p. 208102, May 2012.

[14] V. M. Schimmenti, S. N. Majumdar, and A. Rosso, "Statistical properties of avalanches via the mml:math xmlns:mml="http://www.w3.org/1998/math/MathML"mml:mic/mml:mi/mml:math -record process," *Physical Review E*, vol. 104, Dec. 2021.

[15] B. Alessandro, C. Beatrice, G. Bertotti, and A. Montorsi, "Domain-wall dynamics and barkhausen effect in metallic ferromagnetic materials. i. theory," *Journal of applied physics*, vol. 68, no. 6, pp. 2901–2907, 1990.

[16] P. Chauve, P. L. Doussal, and K. J. Wiese, "Renormalization of pinned elastic systems: How does it work beyond one loop?," *Physical Review Letters*, vol. 86, pp. 1785–1788, Feb. 2001.

[17] E. E. Ferrero, L. Foini, T. Giamarchi, A. B. Kolton, and A. Rosso, "Spatiotemporal patterns in ultraslow domain wall creep dynamics," *Phys. Rev. Lett.*, vol. 118, p. 147208, Apr 2017.

[18] P. M. R. DeVries, F. Viégas, M. Wattenberg, and B. J. Meade, "Deep learning of aftershock patterns following large earthquakes," *Nature*, vol. 560, pp. 632–634, Aug. 2018.

[19] H. Darcy, *Les fontaines publiques de la ville de Dijon: exposition et application.* 1856.

[20] G. Durin, V. M. Schimmenti, M. Baiesi, A. Casiraghi, A. Magni, L. Herrera-Diez, D. Ravelosona, L. Foini, and A. Rosso, "Earthquake-like dynamics in ultrathin magnetic film," 2023.

[21] V. M. Schimmenti, G. Petrillo, A. Rosso, and F. P. Landes, "Assessing the predicting power of gps data for aftershocks forecasting," 2023.

[22] V. M. Schimmenti, F. Lanza, A. Hansen, S. Franz, A. Rosso, L. Talon, and A. De Luca, "Darcy's law of yield stress fluids on a treelike network," *Phys. Rev. E*, vol. 108, p. L023102, Aug 2023.

[23] T. Utsu, Y. Ogata, *et al.*, "The centenary of the omori formula for a decay law of aftershock activity," *Journal of Physics of the Earth*, vol. 43, no. 1, pp. 1–33, 1995.

[24] B. Persson, F. Bucher, and B. Chiaia, "Elastic contact between randomly rough surfaces: comparison of theory with numerical results," *Physical review B*, vol. 65, no. 18, p. 184106, 2002.

[25] T. Baumberger and C. Caroli, "Solid friction from stick–slip down to pinning and aging," *Advances in Physics*, vol. 55, no. 3-4, pp. 279–348, 2006.

[26] P. Le Doussal and K. J. Wiese, "Driven particle in a random landscape: Disorder correlator, avalanche distribution, and extreme value statistics of records," *Phys. Rev. E*, vol. 79, p. 051105, May 2009.

[27] C. ter Burg, P. Rissone, M. Rico-Pasto, F. Ritort, and K. J. Wiese, "Experimental test of sinai's model in DNA unzipping," *Physical Review Letters*, vol. 130, May 2023.

[28] J. Franke, G. Wergen, and J. Krug, "Records and sequences of records from random variables with a linear trend," *Journal of Statistical Mechanics: Theory and Experiment*, vol. 2010, p. P10013, Oct. 2010.

[29] G. Wergen, J. Franke, and J. Krug, "Correlations between record events in sequences of random variables with a linear trend," *Journal of Statistical Physics*, vol. 144, pp. 1206–1222, Sept. 2011.

[30] J. Franke, G. Wergen, and J. Krug, "Correlations of record events as a test for heavy-tailed distributions," *Physical Review Letters*, vol. 108, Feb. 2012.

[31] S.-C. Park, I. G. Szendro, J. Neidhart, and J. Krug, "Phase transition in random adaptive walks on correlated fitness landscapes," *Physical Review E*, vol. 91, Apr. 2015.

[32] S. N. Majumdar and A. Pal, "Extreme value statistics of correlated random variables," 2014.

[33] C. Godrèche, S. N. Majumdar, and G. Schehr, "Record statistics of a strongly correlated time series: random walks and lévy flights," *Journal of Physics A: Mathematical and Theoretical*, vol. 50, p. 333001, July 2017.

[34] S. N. Majumdar, A. Pal, and G. Schehr, "Extreme value statistics of correlated random variables: A pedagogical review," *Physics Reports*, vol. 840, pp. 1–32, Jan. 2020.

[35] S. Redner, *A Guide to First-Passage Processes*. Cambridge University Press, Aug. 2001.

[36] B. D. Bruyne, J. Randon-Furling, and S. Redner, "Optimization in first-passage resetting," *Physical Review Letters*, vol. 125, July 2020.

[37] B. D. Bruyne, J. Randon-Furling, and S. Redner, "Optimization and growth in first-passage resetting," *Journal of Statistical Mechanics: Theory and Experiment*, vol. 2021, p. 013203, Jan. 2021.

[38] S.-C. Park, J. Neidhart, and J. Krug, "Greedy adaptive walks on a correlated fitness landscape," *Journal of Theoretical Biology*, vol. 397, pp. 89–102, May 2016.

[39] S.-C. Park and J. Krug, "i/i-exceedance records and random adaptive walks," *Journal of Physics A: Mathematical and Theoretical*, vol. 49, p. 315601, July 2016.

[40] K. Christensen and Z. Olami, "Variation of the gutenberg-richter ib/i values and nontrivial temporal correlations in a spring-block model for earthquakes," *Journal of Geophysical Research: Solid Earth*, vol. 97, pp. 8729–8735, June 1992.

[41] E. Jagla, F. P. Landes, and A. Rosso, "Viscoelastic effects in avalanche dynamics: A key to earthquake statistics," *Physical Review Letters*, vol. 112, Apr. 2014.

[42] F. P. Landes, *Viscoelastic Interfaces Driven in Disordered Media*. Springer International Publishing, 2016.

[43] L.-H. Tang, M. Kardar, and D. Dhar, "Driven depinning in anisotropic media," *Phys. Rev. Lett.*, vol. 74, pp. 920–923, Feb 1995.

[44] G. Mukerjee, J. A. Bonachela, M. A. Muñoz, and K. J. Wiese, "Depinning in the quenched kardar-parisi-zhang class. i. mappings, simulations, and algorithm," *Physical Review E*, vol. 107, May 2023.

[45] G. Mukerjee and K. J. Wiese, "Depinning in the quenched kardar-parisi-zhang class. II. field theory," *Physical Review E*, vol. 107, May 2023.

[46] K. J. Wiese, "Theory and experiments for disordered elastic manifolds, depinning, avalanches, and sandpiles," *Reports on Progress in Physics*, vol. 85, p. 086502, Apr. 2022.

[47] A. I. Larkin, "Effect of inhomogeneities on the structure of the mixed state of superconductors.," *Zh. Eksp. Theor. Fiz. 58: 1466-70(Apr 1970).*

[48] K. J. Wiese and P. Le Doussal, "Functional renormalization for disordered systems basic recipes and gourmet dishes," *Markov Processes Relat. Fields 13 (2007) 777-818*, 2006.

[49] M. Kardar, "Replica bethe ansatz studies of two-dimensional interfaces with quenched random impurities," *Nuclear Physics B*, vol. 290, pp. 582–602, Jan. 1987.

[50] E. E. Ferrero, L. Foini, T. Giamarchi, A. B. Kolton, and A. Rosso, "Creep motion of elastic interfaces driven in a disordered landscape," *Annual Review of Condensed Matter Physics*, vol. 12, pp. 111–134, Mar. 2021.

[51] A. A. Middleton, P. L. Doussal, and K. J. Wiese, "Measuring functional renormalization group fixed-point functions for pinned manifolds," *Physical Review Letters*, vol. 98, Apr. 2007.

[52] P. L. Doussal, A. A. Middleton, and K. J. Wiese, "Statistics of static avalanches in a random pinning landscape," *Physical Review E*, vol. 79, May 2009.

[53] L. B. Ioffe and V. M. Vinokur, "Dynamics of interfaces and dislocations in disordered media," *Journal of Physics C: Solid State Physics*, vol. 20, no. 36, p. 6149, 1987.

[54] S. Lemerle, J. Ferré, C. Chappert, V. Mathet, T. Giamarchi, and P. Le Doussal, "Domain wall creep in an Ising ultrathin magnetic film," *Phys. Rev. Lett.*, vol. 80, pp. 849–852, Jan 1998.

[55] K.-J. Kim, J.-C. Lee, S.-M. Ahn, K.-S. Lee, C.-W. Lee, Y. J. Cho, S. Seo, K.-H. Shin, S.-B. Choe, and H.-W. Lee, "Interdimensional universality of dynamic interfaces," *Nature*, vol. 458, pp. 740–742, Apr. 2009.

[56] T. Nattermann, "Interface roughening in systems with quenched random impurities," *Europhysics Letters*, vol. 4, no. 11, p. 1241, 1987.

[57] B. Drossel and M. Kardar, "Scaling of energy barriers for flux lines and other random systems," *Phys. Rev. E*, vol. 52, pp. 4841–4852, Nov 1995.

[58] P. W. ANDERSON and Y. B. KIM, "Hard superconductivity: Theory of the motion of abrikosov flux lines," *Rev. Mod. Phys.*, vol. 36, pp. 39–43, Jan 1964.

[59] L. Herrera Diez, F. García-Sánchez, J.-P. Adam, T. Devolder, S. Eimer, M. S. El Hadri, A. Lamperti, R. Mantovan, B. Ocker, and D. Ravelosona, "Controlling magnetic domain wall motion in the creep regime in He^+-irradiated CoFeB/MgO films with perpendicular anisotropy," *Appl. Phys. Lett.*, vol. 107, p. 032401, Jul 2015.

[60] P. Duval, M. Montagnat, F. Grennerat, J. Weiss, J. Meyssonnier, and A. Philip, "Creep and plasticity of glacier ice: a material science perspective," *Journal of Glaciology*, vol. 56, no. 200, pp. 1059–1068, 2010.

[61] M. P. Grassi, A. B. Kolton, V. Jeudy, A. Mougin, S. Bustingorry, and J. Curiale, "Intermittent collective dynamics of domain walls in the creep regime," *Phys. Rev. B*, vol. 98, p. 224201, Dec 2018.

[62] T. Tybell, P. Paruch, T. Giamarchi, and J.-M. Triscone, "Domain wall creep in epitaxial ferroelectric $Pb(Zr_{0.2}Ti_{0.8})O_3$ thin films," *Phys. Rev. Lett.*, vol. 89, p. 097601, Aug 2002.

[63] B. Casals, G. F. Nataf, and E. K. Salje, "Avalanche criticality during ferroelectric/ferroelastic switching," *Nature Communications*, vol. 12, no. 1, p. 345, 2021.

[64] P. Tückmantel, I. Gaponenko, N. Caballero, J. C. Agar, L. W. Martin, T. Giamarchi, and P. Paruch, "Local probe comparison of ferroelectric switching event statistics in the creep and depinning regimes in $Pb(Zr_{0.2}Ti_{0.8})O_3$ thin films," *Physical Review Letters*, vol. 126, no. 11, p. 117601, 2021.

[65] L. Ponson, D. Bonamy, and E. Bouchaud, "Two-dimensional scaling properties of experimental fracture surfaces," *Phys. Rev. Lett.*, vol. 96, p. 035506, Jan 2006.

[66] M. Ozawa and G. Biroli, "Elasticity, facilitation, and dynamic heterogeneity in glass-forming liquids," *Phys. Rev. Lett.*, vol. 130, p. 138201, Mar 2023.

[67] A. Tahaei, G. Biroli, M. Ozawa, M. Popović, and M. Wyart, "Scaling description of dynamical heterogeneity and avalanches of relaxation in glass-forming liquids," 2023.

[68] M. Kuepferling, A. Casiraghi, G. Soares, G. Durin, F. Garcia-Sanchez, L. Chen, C. Back, C. Marrows, S. Tacchi, and G. Carlotti, "Measuring interfacial Dzyaloshinskii-Moriya interaction in ultrathin magnetic films," *Rev. Mod. Phys.*, vol. 95, p. 015003, mar 2023.

[69] G. C. King, R. S. Stein, and J. Lin, "Static stress changes and the triggering of earthquakes," *Bulletin of the Seismological Society of America*, vol. 84, no. 3, pp. 935–953, 1994.

[70] S. Toda, R. S. Stein, P. A. Reasenberg, J. H. Dieterich, and A. Yoshida, "Stress transferred by the 1995 mw= 6.9 kobe, japan, shock: Effect on aftershocks and future earthquake probabilities," *Journal of Geophysical Research: Solid Earth*, vol. 103, no. B10, pp. 24543–24565, 1998.

[71] T. Parsons, R. S. Stein, R. W. Simpson, and P. A. Reasenberg, "Stress sensitivity of fault seismicity: A comparison between limited-offset oblique and major strike-slip faults," *Journal of Geophysical Research: Solid Earth*, vol. 104, no. B9, pp. 20183–20202, 1999.

[72] P. A. Reasenberg and R. W. Simpson, "Response of regional seismicity to the static stress change produced by the loma prieta earthquake," *Science*, vol. 255, no. 5052, pp. 1687–1690, 1992.

[73] E. Jacques, G. King, P. Tapponnier, J. Ruegg, and I. Manighetti, "Seismic activity triggered by stress changes after the 1978 events in the asal rift, djibouti," *Geophysical research letters*, vol. 23, no. 18, pp. 2481–2484, 1996.

[74] C. Nostro, M. Cocco, and M. E. Belardinelli, "Static stress changes in extensional regimes: an application to southern apennines (italy)," *Bulletin of the Seismological Society of America*, vol. 87, no. 1, pp. 234–248, 1997.

[75] T. Wang, J. Zhuang, T. Kato, and M. Bebbington, "Assessing the potential improvement in short-term earthquake forecasts from incorporation of GPS data," *Geophysical Research Letters*, vol. 40, pp. 2631–2635, June 2013.

[76] V. Gitis, A. Derendyaev, and K. Petrov, "Analyzing the performance of GPS data for earthquake prediction," *Remote Sensing*, vol. 13, p. 1842, May 2021.

[77] J. Kouba *Studia Geophysica et Geodaetica*, vol. 47, no. 4, pp. 741–755, 2003.

[78] J. Hu, Z. W. Li, X. L. Ding, J. J. Zhu, and Q. Sun, "Derivation of 3-d coseismic surface displacement fields for the 2011 mw 9.0 tohoku-oki earthquake from

InSAR and GPS measurements," *Geophysical Journal International*, vol. 192, pp. 573–585, Nov. 2012.

[79] D. T. Sandwell and P. Wessel, "Interpolation of 2-d vector data using constraints from elasticity," *Geophysical Research Letters*, vol. 43, no. 20, pp. 10–703, 2016.

[80] G. Costantino, S. Giffard-Roisin, D. Marsan, L. Marill, M. Radiguet, M. D. Mura, G. Janex, and A. Socquet, "Seismic source characterization from GNSS data using deep learning," *Journal of Geophysical Research: Solid Earth*, vol. 128, Apr. 2023.

[81] *Theory of Elasticity.* Elsevier, 1986.

[82] H. Gercek, "Poisson's ratio values for rocks," *International Journal of Rock Mechanics and Mining Sciences*, vol. 44, pp. 1–13, Jan. 2007.

[83] J. Zhuang, Y. Ogata, and D. Vere-Jones, "Stochastic declustering of space-time earthquake occurrences," *Journal of the American Statistical Association*, vol. 97, pp. 369–380, June 2002.

[84] Y. Okada, "Internal deformation due to shear and tensile faults in a half-space," *Bulletin of the Seismological Society of America*, vol. 82, pp. 1018–1040, Apr. 1992.

[85] A. Fall, F. m. c. Bertrand, G. Ovarlez, and D. Bonn, "Yield stress and shear banding in granular suspensions," *Phys. Rev. Lett.*, vol. 103, p. 178301, Oct 2009.

[86] J. Piau, "Carbopol gels: Elastoviscoplastic and slippery glasses made of individual swollen sponges: Meso- and macroscopic properties, constitutive equations and scaling laws," *Journal of Non-Newtonian Fluid Mechanics*, vol. 144, no. 1, pp. 1 – 29, 2007.

[87] H. Pascal, "Nonsteady flow through porous media in the presence of a threshold gradient," *Acta Mechanica*, vol. 39, pp. 207–224, Sep 1981.

[88] P. Coussot, *Rheometry of pastes, suspensions, and granular materials: applications in industry and environment.* John Wiley and Sons, 2005.

[89] T. Chevalier, C. Chevalier, X. Clain, J. Dupla, J. Canou, S. Rodts, and P. Coussot, "Darcy's law for yield stress fluid flowing through a porous medium," *Journal of Non-Newtonian Fluid Mechanics*, vol. 195, pp. 57–66, May 2013.

[90] T. Chevalier and L. Talon, "Generalization of darcy's law for bingham fluids in porous media: From flow-field statistics to the flow-rate regimes," *Phys. Rev. E*, vol. 91, p. 023011, Feb 2015.

[91] L. Talon and D. Bauer, "On the determination of a generalized darcy equation for yield-stress fluid in porous media using a lattice-boltzmann TRT scheme," *The European Physical Journal E*, vol. 36, Dec. 2013.

[92] T. Chevalier and L. Talon, "Moving line model and avalanche statistics of bingham fluid flow in porous media," *The European Physical Journal E*, vol. 38, July 2015.

[93] P. Aussillous, Z. Zou, É. Guazzelli, L. Yan, and M. Wyart, "Scale-free channeling patterns near the onset of erosion of sheared granular beds," *Proceedings of the National Academy of Sciences*, vol. 113, pp. 11788–11793, Oct. 2016.

[94] B. Derrida, "Random-energy model: An exactly solvable model of disordered systems," *Phys. Rev. B*, vol. 24, pp. 2613–2626, Sep 1981.

[95] C. Liu, A. D. Luca, A. Rosso, and L. Talon, "Darcy's law for yield stress fluids," *Physical Review Letters*, vol. 122, June 2019.

[96] K. Johansson, "Shape fluctuations and random matrices," *Communications in Mathematical Physics*, vol. 209, pp. 437–476, Feb. 2000.

[97] B. Derrida and H. Spohn, "Polymers on disordered trees, spin glasses, and traveling waves," *Journal of Statistical Physics*, vol. 51, pp. 817–840, June 1988.

[98] S. N. Majumdar and P. L. Krapivsky, "Extremal paths on a random cayley tree," *Phys. Rev. E*, vol. 62, pp. 7735–7742, Dec 2000.

[99] S. N. Majumdar and P. L. Krapivsky, "Extreme value statistics and traveling fronts: Application to computer science," *Phys. Rev. E*, vol. 65, p. 036127, Feb 2002.

[100] S. N. Majumdar and P. Krapivsky, "Extreme value statistics and traveling fronts: various applications," *Physica A: Statistical Mechanics and its Applications*, vol. 318, pp. 161–170, Feb. 2003.

[101] É. Brunet and B. Derrida, "A branching random walk seen from the tip," *Journal of Statistical Physics*, vol. 143, pp. 420–446, Apr. 2011.

[102] B. Derrida and P. Mottishaw, "On the genealogy of branching random walks and of directed polymers," *EPL (Europhysics Letters)*, vol. 115, p. 40005, Aug. 2016.

[103] M. Båth, "B. gutenberg and c. f. richter, seismicity of the earth and associated phenomena," *Tellus*, vol. 2, p. 68–68, Feb. 1950.

[104] M. Bramson, *Convergence of Solutions of the Kolmogorov Equation to Traveling Waves*. 1983.